Check for updates

Article

TRANSPARENT PROCESS OPEN ACCESS

THE EMBO JOURNAL

Stress-dependent macromolecular crowding in the mitochondrial matrix

Elianne P Bulthuis[1,†,‡], Cindy E J Dieteren[1,2,†,¶], Jesper Bergmans[3], Job Berkhout[1], Jori A Wagenaars[1], Els M A van de Westerlo[1], Emina Podhumljak[1,§], Mark A Hink[4], Laura F B Hesp[1], Hannah S Rosa[5], Afshan N Malik[5], Mariska Kea-te Lindert[2], Peter H G M Willems[1], Han J G E Gardeniers[6,7], Wouter K den Otter[7,8,‡], Merel J W Adjobo-Hermans[1,‡] & Werner J H Koopman[3,9,*,‡]

Abstract

Macromolecules of various sizes induce crowding of the cellular environment. This crowding impacts on biochemical reactions by increasing solvent viscosity, decreasing the water-accessible volume and altering protein shape, function, and interactions. Although mitochondria represent highly protein-rich organelles, most of these proteins are somehow immobilized. Therefore, whether the mitochondrial matrix solvent exhibits macromolecular crowding is still unclear. Here, we demonstrate that fluorescent protein fusion peptides (AcGFP1 concatemers) in the mitochondrial matrix of HeLa cells display an elongated molecular structure and that their diffusion constant decreases with increasing molecular weight in a manner typical of macromolecular crowding. Chloramphenicol (CAP) treatment impaired mitochondrial function and reduced the number of cristae without triggering mitochondrial orthodox-to-condensed transition or a mitochondrial unfolded protein response. CAP-treated cells displayed progressive concatemer immobilization with increasing molecular weight and an eightfold matrix viscosity increase, compatible with increased macromolecular crowding. These results establish that the matrix solvent exhibits macromolecular crowding in functional and dysfunctional mitochondria. Therefore, changes in matrix crowding likely affect matrix biochemical reactions in a manner depending on the molecular weight of the involved crowders and reactants.

Keywords chloramphenicol; diffusion; FRAP; macromolecular crowding; mitochondria

Subject Category Organelles

DOI 10.15252/embj.2021108533 | Received 21 April 2021 | Revised 10 January 2023 | Accepted 19 January 2023 | Published online 24 February 2023

The EMBO Journal (2023) 42: e108533

Introduction

Mitochondria host a large variety of biochemical reactions, including the ATP-generating oxidative phosphorylation (OXPHOS) system (Smeitink *et al*, 2001; Rath *et al*, 2021). Structurally, mitochondria consist of an inner (MIM) and outer membrane (MOM), which surround the mitochondrial matrix compartment. The MIM contains many folds (cristae) that protrude into the matrix thereby providing a large surface area for biochemical reactions. Alterations in metabolic state are generally paralleled by dynamic changes in mitochondrial internal and external structure, matrix volume, and physicochemical properties of the matrix solvent (Hackenbrock, 1966; Perkins & Ellisman, 2011; Willems *et al*, 2015; Bulthuis *et al*, 2019). It is to be expected that these changes are functionally relevant through affecting matrix solute diffusion and biochemical reaction dynamics (Scalettar *et al*, 1991; Lizana *et al*, 2008; Perkins & Ellisman, 2011; Dieteren *et al*, 2011a; Cogliati *et al*, 2016; Sprenger & Langer, 2019).

1 Department of Biochemistry, Radboud Institute for Molecular Life Sciences (RIMLS), Radboud Center for Mitochondrial Medicine (RCMM), Radboud University Medical Centre (Radboudumc), Nijmegen, The Netherlands
2 Department of Cell Biology and Electron Microscopy Center, Radboudumc, Nijmegen, The Netherlands
3 Department of Pediatrics, Amalia Children's Hospital, Radboud Institute for Molecular Life Sciences (RIMLS), Radboud Center for Mitochondrial Medicine (RCMM), Radboud University Medical Center (Radboudumc), Nijmegen, The Netherlands
4 Swammerdam Institute for Life Sciences, University of Amsterdam, Amsterdam, The Netherlands
5 Department of Diabetes, King's College London, London, UK
6 Mesoscale Chemical Systems, University of Twente, Enschede, The Netherlands
7 MESA+ Institute for Nanotechnology, University of Twente, Enschede, The Netherlands
8 Thermal and Fluid Engineering, Faculty of Engineering Technology, University of Twente, Enschede, The Netherlands
9 Human and Animal Physiology, Wageningen University, Wageningen, The Netherlands
*Corresponding author. Tel: +31 24 3614589; E-mail: werner.koopman@radboudumc.nl
†These authors contributed equally to this work as first authors
‡These authors contributed equally to this work as senior authors
§Present address: Department of Human Genetics, Amsterdam UMC, Amsterdam, The Netherlands
¶Present address: Protinhi Therapeutics, Nijmegen, The Netherlands
#Present address: Khondrion B.V., Nijmegen, The Netherlands

© 2023 The Authors. Published under the terms of the CC BY NC ND 4.0 license.

Diffusion-limited bioreactions often involve "target finding" by (partially) mobile enzymes and/or substrates that need to diffuse towards a binding partner (Haggie & Verkman, 2002; Wilkens *et al*, 2013; Dey & Bhattacherjee, 2019). An example of such a system is the biogenesis of OXPHOS Complex I (CI), which involves matrix diffusion of an 100–200 kDa assembly intermediate in search of a MIM-attached scaffold (Dieteren *et al*, 2008, 2011b; Koopman *et al*, 2010; Guerrero-Castillo *et al*, 2017). However, our quantitative understanding of solute diffusion in the mitochondrial matrix is still limited. A key parameter in this respect is the solvent-dependent diffusion constant of the solute ($D_{solvent}$; Weiss, 2014). For any given solute, the value of $D_{solvent}$ is linked to the physicochemical properties of the solvent like viscosity ($\eta_{solvent}$), absolute temperature (T), and solute properties like molecular structure and molecular weight (MW). The former is quantitatively described by the radius of gyration (R_G) and hydrodynamic radius (R_H) of the solute (Einstein, 1905; Sutherland, 1905; von Smoluchowski, 1906; Young *et al*, 1980; Tyn & Gusek, 1990; He & Niemeyer, 2003; Saxton, 2014). With respect to solute diffusion in the mitochondrial matrix, it has been previously demonstrated that mitochondrial cristae can act as diffusion barriers that impede the free diffusion of fluorescent proteins (FPs; Ölveczky & Verkman, 1998; Partikian *et al*, 1998; Dieteren *et al*, 2011a).

In addition to cristae, macromolecular crowding is also a potential key factor influencing solute diffusion by increasing effective solvent viscosity and reducing the water-accessible volume via volume exclusion, the extent of which increases with crowder size (Boersma *et al*, 2015; Rivas & Minton, 2016). In this way, macromolecular crowding can alter the hydrodynamic volume (compaction, shape, folding, structure, and conformational stability) and/or association state (protein–protein interactions, aggregation, oligomerization, and phase separation) of proteins (Kuznetzova *et al*, 2014). This will affect their chemical reaction rates and/or molecular target finding (Dey & Bhattacherjee, 2019; Weilandt & Hatzimanikatis, 2019). Macromolecular crowding can also induce "molecular sieving" effects, which alter the translational mobility of biomolecules in an MW/size-dependent manner (Papadopoulos *et al*, 2000; Mika *et al*, 2010; Junker *et al*, 2019; Van Tartwijk & Kaminski, 2022). In this sense, macromolecular crowding will reduce the diffusion coefficient of larger tracer molecules to a greater extent than predicted by the Stokes–Einstein equation (Mika *et al*, 2010; Delarue *et al*, 2018; Junker *et al*, 2019). Experimental and theoretical studies suggest that modulation of macromolecular crowding can act as a (patho)physiological control mechanism in prokaryotes and eukaryotes (Scalettar *et al*, 1991; Akabayov *et al*, 2013; Poggi & Slade, 2015; Cravens *et al*, 2015; Joyner *et al*, 2015; Hansen *et al*, 2016; Delarue *et al*, 2018; Schavemaker *et al*, 2018; Fuentes-Lemus *et al*, 2021; Hochmair *et al*, 2022; Vorontsova *et al*, 2022). The mitochondrial matrix compartment is classically recognized as highly protein-rich. For instance, 46% of all mitochondrial proteins were predicted to be matrix-localized in humans (Rath *et al*, 2021) and 20% of the mitochondrial proteins were classified as matrix-soluble in *Saccharomyces cerevisiae* (Vögtle *et al*, 2017). Therefore, it appears likely that the mitochondrial matrix fluid displays macromolecular crowding-related phenomena. However, given the biological functions of these matrix proteins (e.g., metabolism, mtDNA maintenance, OXPHOS assembly; Rath *et al*, 2021), they might not always be expressed at the same levels and/or could be (transiently) MIM-attached or otherwise immobilized. For example, four of the most abundant mitochondrial proteins (ATP5A1, ATP5B, ANT1, and ANT2) are membrane-bound (Calvo & Mootha, 2010). In addition, TCA cycle enzymes and subunits of the fatty acid β-oxidation multienzyme complex appear to be organized in (MIM-attached) multiprotein complexes with restricted mobility (Robinson & Srere, 1985; Partikian *et al*, 1998; Haggie & Verkman, 2002; Fernie *et al*, 2018). This suggests that the protein concentration of the mitochondrial matrix solvent might be (substantially) lower than generally assumed. Moreover, quantitative live-cell evidence demonstrating the existence of macromolecular crowding-related phenomena in the mitochondrial matrix fluid is lacking. Here, we aimed at providing such evidence by quantifying the mobility of matrix-targeted fluorescent protein (FP) concatemers of increasing MW (AcGFP1, $AcGFP1^2$, $AcGFP1^3$, and $AcGFP1^4$). To this end, fluorescence recovery after photobleaching (FRAP) experiments and Brownian dynamics (BD) simulations were integrated to obtain quantitative estimates of $D_{solvent}$ and $\eta_{solvent}$ in functionally active and dysfunctional mitochondria. The obtained results support the conclusion that the mitochondrial matrix fluid displays macromolecular crowding and that this crowding is increased during chloramphenicol (CAP)-induced mitochondrial dysfunction.

Results

A key phenomenon associated with macromolecular crowding is that it reduces the translational mobility of solutes with a similar or larger size than the crowder to a greater extent than the mobility of smaller solutes (e.g., Mika *et al*, 2010; Delarue *et al*, 2018; Junker *et al*, 2019; Van Tartwijk & Kaminski, 2022). The solvent-dependent translational mobility of a solute in the mitochondrial matrix is quantitatively described by its solvent-dependent diffusion constant ($D_{solvent}$). Therefore, we here quantified $D_{solvent}$ values of mitochondria-targeted AcGFP1 concatemers of increasing MW (AcGFP1, $AcGFP1^2$, $AcGFP1^3$, and $AcGFP1^4$) in HeLa cells. To this end, fluorescence recovery after photobleaching (FRAP) analysis of these fluorescent proteins (FPs) was combined with predictive, experimentally constrained, Brownian dynamics (BD) computer simulations. This strategy aimed at delivering quantitative estimates for $D_{solvent}$ and matrix solvent viscosity ($\eta_{solvent}$) in functional mitochondria, as well as in dysfunctional mitochondria treated with the mitochondrial RNA (mtRNA) translation inhibitor chloramphenicol (CAP). Interpretation of these estimates was used to gain insight into macromolecular crowding, concatemer structural conformation, and $\eta_{solvent}$ in the mitochondrial matrix (Fig 1).

Expression, localization, and integrity of mitochondrial matrix-targeted FPs

Four HeLa cell lines were created that stably expressed matrix-targeted AcGFP1 concatemers. These proteins were targeted to the mitochondrial matrix using N-terminal fusions with a mitochondrial targeting sequence (MTS), consisting of a 25-residue Cox8 sequence. In case of $AcGFP1^4$, a double MTS was used to improve mitochondrial matrix delivery (Filippin *et al*, 2005). AcGFP1 and MTS domains were connected by flexible peptide linkers (Appendix Table S1), and FP expression was controlled by a doxycycline

© 2023 The Authors

14602075, 2023, 7, Downloaded from https://www.embopress.org/doi/10.15252/embj.2021108533 by Wageningen University and Research Bibliotheek, Wiley Online Library on [11/08/2023]. See the Terms and Conditions (https://onlinelibrary.wiley.com/terms-and-conditions) on Wiley Online Library for rules of use; OA articles are governed by the applicable Creative Commons License

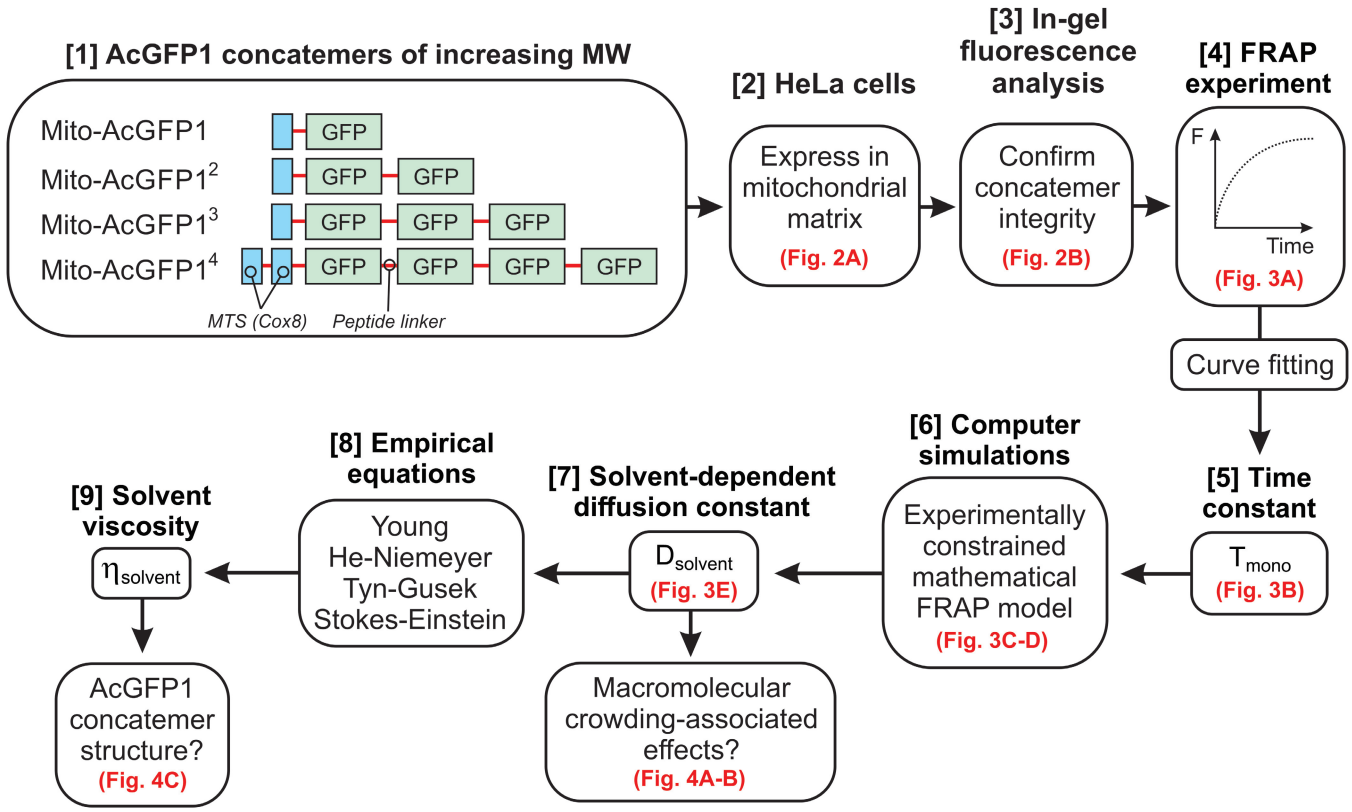

Figure 1. Integrated strategy for quantifying the solvent-dependent diffusion constants of mitochondrial matrix-targeted fluorescent proteins and mitochondrial matrix solvent viscosity.

Corresponding figures are highlighted in red. Four mitochondrial matrix-targeted concatemers of the monomeric fluorescent protein AcGFP1 [1] were stably expressed in HeLa cells [2]. The integrity and mobility of these fluorescent proteins (FPs) was investigated by in-gel fluorescence analysis [3] and fluorescence recovery after photobleaching (FRAP) recordings [4], respectively. Curve fitting was applied to obtain a mono-exponential FRAP time constant for each concatemer (T_{mono}) [5]. The latter were fed into an experimentally constrained mathematical FRAP model [6] to compute solvent-dependent diffusion constants ($D_{solvent}$; [7]). By inserting these constants into four empirical equations [8], the viscosity of the mitochondrial matrix solvent ($\eta_{solvent}$) was determined [9]. Finally, the obtained $\eta_{solvent}$ and $D_{solvent}$ values were interpreted to draw conclusions on the structural conformation of the concatemers and the presence of macromolecular crowding phenomena in the mitochondrial matrix.

(DOX)-inducible promoter. Following induction, all FPs displayed a mitochondrial localization as demonstrated by confocal microscopy and MitoTracker Red co-staining (Fig 2A). Western blot analysis of mitochondrial fractions demonstrated that DOX treatment increased the in-gel fluorescence and expression of the FPs (Fig 2B; marked by *). AcGFP1 and AcGFP1^2 displayed a single major fluorescent product, compatible with our previous findings with DOX-inducible HEK293 cells (Dieteren *et al*, 2008, 2011a, 2011b). Similarly, AcGFP1^3-expressing cells displayed a single fluorescence band albeit of much lower intensity. By contrast, mitochondria in AcGFP1^4-expressing cells contained two fluorescence products, one of the expected size (Fig 2B; marked by *) and another of lower MW (marked by #). Fluorescence analysis by flow cytometry (Fig 2C) correlated well with in-gel fluorescence signals (Fig 2D). This demonstrates that all inducible FP cell lines exhibit a low fluorescence signal in their noninduced state and strongly suggests that the cellular fluorescence intensities reflect mitochondria-specific signals. The former observation is compatible with low-level induction ("leakage") of FP expression in the mitochondrial matrix occurring in the absence of added DOX, as observed previously in our DOX-inducible HEK293 cell models (Dieteren *et al*, 2011b).

Experimental FRAP analysis of mitochondrial matrix-targeted FP mobility

FP mobility in the mitochondrial matrix was determined by confocal FRAP analysis of individual mitochondria. In this approach, mitochondrial fluorescence is rapidly bleached in a square region of interest (ROI) placed at one end of a single mitochondrial filament (Fig 3A; inset), followed by quantification of fluorescence recovery (Appendix Fig S2). As a quality control measure, this analysis included only individual mitochondria: (i) that were fully located within the focal plane (confirmed by an axial scan), and (ii) in which FRAP was paralleled by fluorescence loss in photobleaching (FLIP) in a part distal to the FRAP region (Appendix Fig S2), indicating that these mitochondria possessed a continuous matrix. Combining multiple experiments yielded an average FRAP curve for each FP (Fig 3A), which was adequately fitted by a mono-exponential

© 2023 The Authors

14602075, 2023, 7, Downloaded from https://www.embopress.org/doi/10.15252/embj.2021108533 by Wageningen University and Research Bibliotheek, Wiley Online Library on [11/08/2023]. See the Terms and Conditions (https://onlinelibrary.wiley.com/terms-and-conditions) on Wiley Online Library for rules of use; OA articles are governed by the applicable Creative Commons License

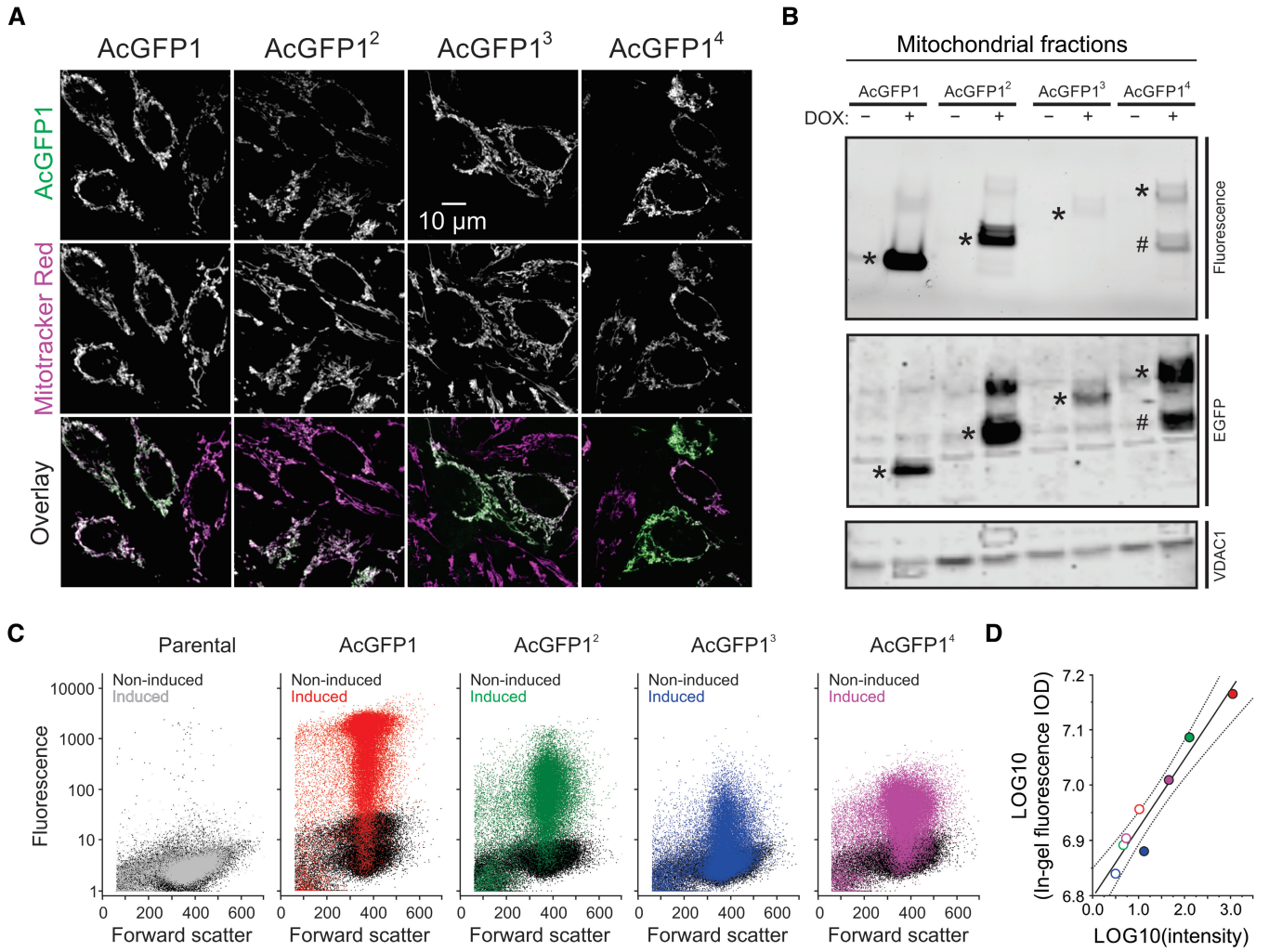

Figure 2. Expression and localization of the mitochondrial matrix-targeted fluorescent proteins.

A Cellular localization of the four AcGFP1 concatemers (AcGFP1, AcGFP1^2, AcGFP1^3, AcGFP1^4) in HeLa cell lines cultured in the presence of the expression inducer doxycycline (DOX). Images were acquired by confocal microscopy and depict typical fluorescence signals of AcGFP1 (upper row), the mitochondrial marker Mitotracker Red CM-H_2XROS (middle row), and an overlay of these signals (lower row; AcGFP1 in green; Mitotracker Red CM-H_2XROS in magenta; colocalization in white).

B Analysis of FP expression and concatemer integrity in mitochondrial fractions isolated from HeLa cells cultured in the absence (–) and presence (+) of DOX. The panels display AcGFP1 fluorescence (SDS–PAGE fluorogram; upper panel), AcGFP1 protein signals (SDS–PAGE; anti-EGFP immunodetection; middle panel) and VDAC1 protein signals (SDS–PAGE; loading control; lower panel). Bands for AcGFP1, AcGFP1^2, AcGFP^3 and AcGFP1^4 are marked by asterisks (*). For AcGFP1^4, also a substantial band of lower MW was detected (marked #). Individual panels were contrast-optimized for visualization purposes. Original blots are presented in Appendix Fig S1A.

C Flow cytometry analysis of the parental and FP-expressing HeLa cell lines. Fluorescence intensity is plotted against forward scatter. The noninduced condition (i.e., in absence of DOX) is depicted by black symbols. The effects of DOX are marked in gray (parental cells) and various colors (FP-expressing cells). For AcGFP1, AcGFP1^2 (noninduced), AcGFP1^3 and AcGFP1^4 a total of $n = 40{,}000$ cells from four technical replicates were analyzed on a single day ($N = 1$). For the AcGFP1^2-induced condition $n = 30{,}000$ cells from three technical replicates are depicted ($N = 1$).

D Correlation between the average AcGFP1 fluorescence intensity in panel (C) (*x*-axis) and the integrated optical density (IOD; *y*-axis) for each condition (full lane) in panel (B) (in-gel fluorescence signal; the original gel was used for quantification). Noninduced cells are marked by open symbols; induced cells are marked with colored symbols (similar to panel C). The continuous line represents a linear fit to the data ($R = 0.966$; $P < 0.0001$). Dotted lines indicate the 95% confidence limits of the fit.

equation (Table 1). The recovery time constant of this fit (T_{mono}), representing the FRAP rate, increased with increasing MW (Table 1 and Fig 3B). This agrees with our previous results with mitochondrial matrix-targeted AcGFP1^1 and AcGFP1^2 in HEK293 cells (Dieteren *et al*, 2011a) and demonstrates that FRAP is slower for FPs with a larger MW. The FP mobile fraction (F_m) somewhat decreased with increasing MW (Table 1 and Fig 3A), suggesting that the FPs became progressively immobilized. A proper comparison of T_{mono} between the different FPs requires that their MW is taken into account (Sprague & McNally, 2005). In case of AcGFP1^4, the fluorescent product of lower MW (Fig 2B) accelerated the average FRAP rate for this FP leading to an underestimation of T_{mono}. To correct for this effect, a straight line was fitted through the origin and the T_{mono} data points for AcGFP1, AcGFP1^2, and AcGFP1^3 (Fig 3B).

© 2023 The Authors

14602075, 2023, 7, Downloaded from https://www.embopress.org/doi/10.15252/embj.2021108533 by Wageningen University and Research Bibliotheek, Wiley Online Library on [11/08/2023]. See the Terms and Conditions (https://onlinelibrary.wiley.com/terms-and-conditions) on Wiley Online Library for rules of use; OA articles are governed by the applicable Creative Commons License

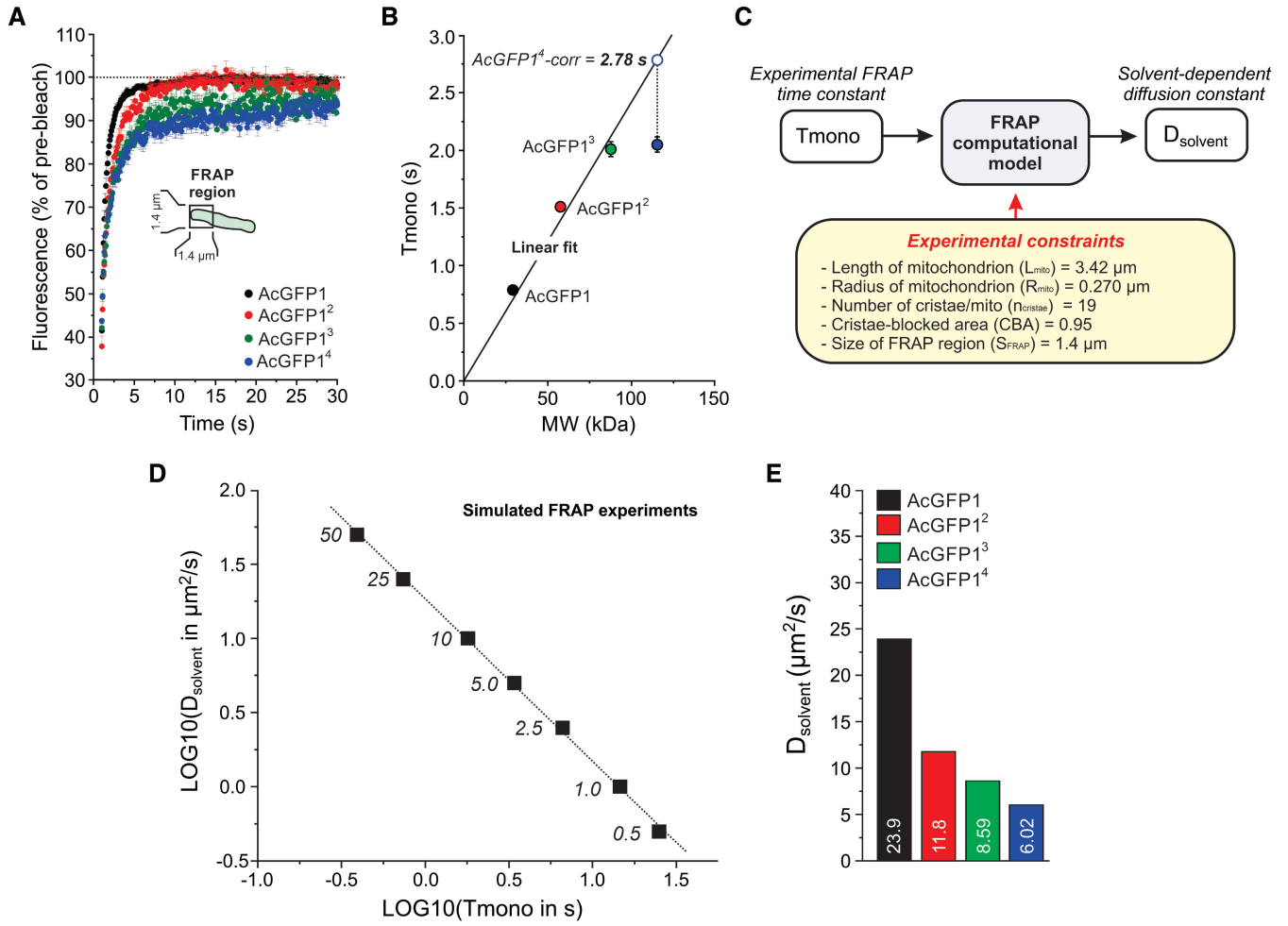

Figure 3. Solvent-dependent mobility of the mitochondrial matrix-targeted fluorescent proteins.

A Average mitochondrial fluorescence recovery after photobleaching (FRAP) curves for the four FPs. These curves were fitted using a mono-exponential function to determine the FRAP recovery time constant T_{mono}. Symbols and error bars indicate mean ± SEM. Data was obtained in at least $N = 3$ independent experiments for $n = 76$ mitochondria (AcGFP1), $n = 30$ (AcGFP1^2), $n = 37$ (AcGFP1^3) and $n = 68$ (AcGFP1^4).

B Relationship between the molecular weight (MW) of the FPs and their FRAP time constant (T_{mono}; numerical data are provided in Table 1). A linear fit was calculated through the origin and the data points for AcGFP1, AcGFP1^2 and AcGFP1^3 ($R = 0.993$, $P = 0.022$; $T_{mono} = B \cdot MW$; B (slope) = 0.0241 ± 0.00118 (SE)). The experimental T_{mono} value for AcGFP^4 (filled blue symbol) was corrected using this linear fit (dotted line; see Results for details) yielding a new T_{mono} value ("AcGFP1^4-corr"). Symbols and error bars reflect mean ± SE (standard error) values from the mono-exponential fit.

C Strategy to compute $D_{solvent}$ from the experimental T_{mono} value for each FP using an experimentally constrained BD simulation model (see Results and Appendix Supplementary Methods for details).

D Linear relationship between LOG10 (T_{mono}) and LOG10 ($D_{solvent}$) predicted by the model for a mitochondrion containing 19 cristae and with a cristae-blocked area (CBA) of 0.95. Parameters of the linear fit (LOG10 ($D_{solvent}$) = A + B·LOG10 (T_{mono})) are: $R = -0.999$, $P < 0.0001$; A (intercept) = 1.27 ± 0.0123 (SE); B (slope) = −1.10 ± 0.0154 (SE)). Numerals indicate the $D_{solvent}$ values (µm^2/s) used in the model (the corresponding FRAP data are presented in Appendix Fig S3B).

E $D_{solvent}$ values of the four FPs (numerals) obtained using the relationship in panel (D) by inserting the experimental T_{mono} values in the fitting equation for panel (D) (see Results for details). Numerical data are provided in Table 1.

Next, the measured T_{mono} value for AcGFP1^4 was projected on the fitted line yielding a corrected ("AcGFP1^4-corr") value (Fig 3B; dotted line and open symbol). This corrected T_{mono} value was used in the remainder of the study.

Brownian dynamics simulations of FRAP experiments

To convert the experimental T_{mono} data into $D_{solvent}$ values, we developed a Brownian dynamics (BD) simulation model (Fig 3C). This quantitative model generated synthetic FRAP curves, used a cristae-containing cylindrical structure to represent mitochondria, and was constrained by experimental data. The latter included mitochondrial length (L_{mito}), mitochondrial radius (R_{mito}), size of the FRAP region (S_{FRAP}), the number of cristae per mitochondrion ($n_{cristae}$), and the "cristae-blocked area" (CBA; expressed as a fraction of the total transecting area). Validated by EM analysis and data on HeLa cristae structure from the literature (Appelhans *et al*, 2011; Wilkens *et al*, 2013; Wolf *et al*, 2019; Hu *et al*, 2020; Segawa

© 2023 The Authors

14602075, 2023, 7, Downloaded from https://www.embopress.org/doi/10.15252/embj.2021108533 by Wageningen University and Research Bibliotheek, Wiley Online Library on [11/08/2023]. See the Terms and Conditions (https://onlinelibrary.wiley.com/terms-and-conditions) on Wiley Online Library for rules of use; OA articles are governed by the applicable Creative Commons License

Table 1. Experimental data and BD modeling results.

	−CAP				+CAP			
Cell line	**AcGFP1**	**AcGFP1^2**	**AcGFP1^3**	**AcGFP1^4**	**AcGFP1**	**AcGFP1^2**	**AcGFP1^3**	**AcGFP1^4**
MW (kDa)[a]	29.155	57.586	87.705	115.337	29.155	57.586	87.705	115.337
LOG10 (MW)	1.4641	1.7603	1.9430	2.06197	1.4641	1.7603	1.9430	2.06197
Mitochondrial length, diameter and radius determined using confocal laser scanning microscopy (CLSM)[b]								
L_{mito} (μm)	3.42 (N = 55)	3.42 (N = 30)	3.42 (N = 37)	3.42 (N = 68)	3.40 (N = 31)	ND	ND	3.42 (N = 26)
D_{mito} (μm)	0.562 ± 0.025 (N = 26)	0.524 ± 0.012 (N = 41)	0.549 ± 0.020 (N = 33)	0.525 ± 0.017 (N = 29)	0.552 ± 0.015 (N = 24)	ND	ND	0.546 ± 0.017 (N = 20)
R_{mito} (μm)	0.281	0.262	0.275	0.263	0.276	ND	ND	0.273
V_{mito} (μm^3)	0.848	0.738	0.813	0.743	0.819	ND	ND	0.801
V_{mito} (l)	$0.848{\cdot}10^{-15}$	$0.738{\cdot}10^{-15}$	$0.813{\cdot}10^{-15}$	$0.743{\cdot}10^{-15}$	$0.819{\cdot}10^{-15}$	ND	ND	$0.801{\cdot}10^{-15}$
Mitochondrial diameter, radius and cristae per mitochondrion determined using electron microscopy (EM)[c]								
D_{mito} (μm)	0.510 ± 0.019 (N = 52)	ND	ND	0.504 ± 0.015 (N = 59)	0.490 ± 0.017 (N = 51)	ND	ND	0.494 ± 0.018 (N = 53)
R_{mito} (μm)	0.255	ND	ND	0.252	0.245	ND	ND	0.247
$n_{cristae}$ (1/μm)	5.620 ± 0.155 (N = 244)	ND	ND	5.462 ± 0.174 (N = 314)	2.705 ± 0.130 (N = 295)	ND	ND	3.50 ± 0.145 (N = 260)
$n_{cristae}$/mito	19	ND	ND	19	9	ND	ND	12
Mono-exponential fitting parameters of the fluorescence recovery after photobleaching (FRAP) curve[d]								
N	76	30	37	68	40	24	26	33
R^2	0.922	0.971	0.932	0.921	0.962	0.947	0.780	0.951
y_0	−80.0 ± 5.85	−0.677 ± 2.42	24.7 ± 2.29	30.7 ± 2.17	39.1 ± 1.20	30.9 ± 0.800	44.2 ± 0.920	47.5 ± 0.767
A_{mono}	178 ± 5.84	98.9 ± 2.40	68.6 ± 2.26	60.5 ± 2.14	55.4 ± 1.17	45.1 ± 0.667	23.6 ± 0.763	39.0 ± 0.706
T_{mono} (s)	0.789 ± 0.015	1.51 ± 0.031	2.01 ± 0.065	2.05 ± 0.066	2.75 ± 0.099	8.76 ± 0.357	9.31 ± 0.883	5.43 ± 0.168
$T_{mono\text{-}corr}$ (s)				2.78				
F_0	41.4 ± 1.61%	37.7 ± 2.40%	42.0 ± 1.80%	43.6 ± 1.22%	42.0 ± 2.60%	22.7 ± 3.38%	40.2 ± 4.51%	42.6 ± 2.50%
F_∞	98.8 ± 11.7%	98.2 ± 4.82%	93.3 ± 4.55%	91.2 ± 4.31%	94.5 ± 2.37%	76.0 ± 1.47%	67.8 ± 1.68%	86.5 ± 1.47%
F_m	0.979	0.972	0.885	0.844	0.904	0.689	0.462	0.765
Parameters and results regarding the BD model[e]								
1. Simulation parameters for $D_{solvent}$ prediction								
Identical for all simulations	L_{mito} = 3.42 μm; R_{mito} = 0.270 μm; S_{FRAP} = 1.4 μm; CBA = 0.95							
$n_{cristae}$	19	19	19	19	9	ND	ND	12
2. Predicted $D_{solvent}$								
$D_{solvent}$ (μm^2/s)	23.9	11.8	8.59	6.02	2.91	NA	NA	NA
LOG10 ($D_{solvent}$)	1.378	1.072	0.9340	0.7796	0.464	NA	NA	NA
3. Computation of radius of gyration (R_G), hydrodynamic radius (R_H) and $\eta_{solvent}$ (cP) at 293 K								
MW (kDa)	29.155	57.586	87.705	115.337	29.155	57.586	87.705	115.337
Assuming that the FP has a compact conformation								
Radius of molecule R (Å)	15	20	20	20	15	NA	NA	NA
Length of molecule L (Å)	40	60	60	60	40	NA	NA	NA
R_G (Å)	15.5	20	20	20	15.5	NA	NA	NA
R_H (Å)	20	23	23	23	20	NA	NA	NA
$\eta_{solvent}$ (Young)	3.32	5.36	6.40	8.34	27.3	NA	NA	NA
$\eta_{solvent}$ (He–Niemeyer)	3.69	5.88	7.53	10.3	30.3	NA	NA	NA

© 2023 The Authors

14602075, 2023, 7, Downloaded from https://www.embopress.org/doi/10.15252/embj.2021108533 by Wageningen University and Research Bibliotheek, Wiley Online Library on [11/08/2023]. See the Terms and Conditions (https://onlinelibrary.wiley.com/terms-and-conditions) on Wiley Online Library for rules of use; OA articles are governed by the applicable Creative Commons License

Table 1 (continued)

	−CAP				+CAP			
Cell line	**AcGFP1**	**AcGFP1^2**	**AcGFP1^3**	**AcGFP1^4**	**AcGFP1**	**AcGFP1^2**	**AcGFP1^3**	**AcGFP1^4**
$\eta_{solvent}$ (Tyn–Gusek)	4.57	7.18	9.86	14.1	37.5	NA	NA	NA
$\eta_{solvent}$ (Stokes–Einstein)	4.49	7.91	10.9	15.5	36.9	NA	NA	NA
Assuming that the FP has an extended conformation								
Radius of molecule R (Å)	15	15	35	35	15	NA	NA	NA
Length of molecule L (Å)	40	130	247	349	40	NA	NA	NA
R_G (Å)	15.5	38	73	102	15.5	NA	NA	NA
R_H (Å)	20	30	61	75	20	NA	NA	NA
$\eta_{solvent}$ (Young)	3.32	5.36	6.40	8.34	27.3	NA	NA	NA
$\eta_{solvent}$ (He–Niemeyer)	3.69	4.27	3.94	4.55	30.3	NA	NA	NA
$\eta_{solvent}$ (Tyn–Gusek)	4.57	3.78	2.70	2.76	37.5	NA	NA	NA
$\eta_{solvent}$ (Stokes–Einstein)	4.49	6.06	4.10	4.75	36.9	NA	NA	NA

BD, Brownian dynamics; CAP, chloramphenicol; $D_{solvent}$, solvent-dependent diffusion constant; $\eta_{solvent}$, solvent-dependent viscosity; NA, not appropriate; ND, not determined; R_G, radius of gyration; R_H, hydrodynamic radius; S_{FRAP}, size of the experimental FRAP region in the BD model; T, temperature; T_{mono}, experimental FRAP mono-exponential time constant.

[a]Molecular weight (MW) was calculated directly from the protein sequences given in Appendix Table S1 (excluding the N-terminal mitochondrial targeting sequence) using the pI/Mw tool (web.expasy.org/compute_pi). One (1) Dalton (Da) equals 1 g/mol.

[b]Confocal laser scanning microscopy (CLSM) analysis: The data are presented as mean ± SEM. *N* indicates the number of mitochondria analyzed in at least two independent experiments. Mitochondrial length (L_{mito}) and mitochondrial diameter (D_{mito}) were determined from the FRAP images by quantifying the frame width at half-maximal height (FWHM; equaling $2{\cdot}R_{mito}$) of a Gaussian curve fitted to a 1 pixel wide intensity profile perpendicular to the short and long axis of the mitochondrial filament (see Appendix Fig S2F). Mitochondrial volume (V_{mito}) was calculated using a cylindrical approximation: $V_{mito} = \pi \cdot (R_{mito})^2 \cdot L_{mito}$. One (1) μm^3 equals 10^{-15} liter, 0.001 picoliter (1 picoliter = 10^{-12} liter) and 1,000 attoliter (1 attoliter = 10^{-18} liter). Average V_{mito} values equaled 0.786 ± 0.0540(SD) μm^3 = 786 attoliter (−CAP) and 0.810 μm^3 = 810 attoliter (+CAP).

[c]Electron microscopy (EM) analysis: The data are presented as mean ± SEM. *N* indicates the number of mitochondria analyzed in two independent experiments. D_{mito} and R_{mito} indicate the mitochondrial diameter and radius, respectively.

[d]Fitting of the fluorescence recovery after photobleaching (FRAP) curve: $y = y_0 + A_{mono}[1-EXP(-t/T_{mono})]$. *N* indicates the number of mitochondria analyzed in at least three independent experiments. The coefficient of determination (R^2) is used as a measure of the goodness of fit (the closer R^2 is to a value of one, the closer the fit is to the data points). The parameter errors reflect the standard error (SE) value from the fit, as reported by the fitting software. F_0 indicates the fluorescence signal at the start of the fluorescence recovery (expressed as % of the prebleach value). F_∞ indicates the fluorescence signal to which the fluorescence signal recovers given by: $y_0 + A_{mono}$ (expressed as % of the prebleach value). The error in F_∞ was calculated by summation of the errors in y_0 and A_{mono}. F_m indicates the mobile fraction given by: $[(F_\infty - F_0+)/(F_i - F_0)]$, with F_i being the prebleach fluorescence equaling 100%.

[e]Mathematical modeling: One (1) Angstrom (Å) equals $1{\cdot}10^{-10}$ m. CBA, cristae-blocked area (fraction of total transecting area). See Results for further details.

et al, 2020; Weissert *et al*, 2021) we assumed in the model that (Appendix Fig S3A): (i) mitochondria contained regularly arranged cristae perpendicular to the longitudinal axis of the mitochondrion, (ii) the positions of the cristae alternated, with consecutive cristae being opposite of each other, (iii) cristae were equidistant, partially overlapping and of negligible thickness (Partikian *et al*, 1998), and (iv) CBA equaled 0.95. The presence of cristae increased the effective length of the "channel" that connected the two ends of the mitochondrion thereby increasing FP diffusion length. In addition, the presence of cristae reduced the diffusive flow between consecutive mitochondrial subcompartments. Therefore, as indicated previously (Ölveczky & Verkman, 1998; Partikian *et al*, 1998), FRAP was slower when more cristae were present (Appendix Fig S3B and C). Further details of the BD model are presented in the Appendix Supplementary Methods.

Determining the $D_{solvent}$ value of mitochondria-targeted FPs

Confocal microscopy analysis of living FP-expressing cells yielded values for L_{mito} and R_{mito} of 3.42 and 0.262–0.281 μm, respectively (Table 1). Similar R_{mito} values (0.252–0.255 μm) were obtained by electron microscopy (EM) analysis of fixed AcGFP1 and AcGFP1^4 cells (Table 1). EM quantification of the number of cristae yielded values of 5.620 cristae/μm (AcGFP1-expressing cells) and 5.462 cristae/μm (AcGFP1^4-expressing cells). This reflects an average $n_{cristae}$ value of 19 (Table 1) and an intercrista distance between 177 and 183 nm. The latter lies within a range of experimental values previously reported for HeLa cells (51–250 nm; Wilkens *et al*, 2013; Stephan *et al*, 2019; Wang *et al*, 2019). Applying these experimental constraints, BD simulations were carried out using the following parameters (Table 1): L_{mito} = 3.42 μm, R_{mito} = 0.270 μm,

© 2023 The Authors

14602075, 2023, 7, Downloaded from https://www.embopress.org/doi/10.15252/embj.2021108533 by Wageningen University and Research Bibliotheek, Wiley Online Library on [11/08/2023]. See the Terms and Conditions (https://onlinelibrary.wiley.com/terms-and-conditions) on Wiley Online Library for rules of use; OA articles are governed by the applicable Creative Commons License

$n_{cristae}$ = 19 and S_{FRAP} = 1.4 μm. Model output was determined for several values of $D_{solvent}$ (0.5–50 $\mu m^2/s$) to establish the relationship between T_{mono} and $D_{solvent}$. On a logarithmic scale, these parameters displayed a linear correlation (Fig 3D), allowing calculation of $D_{solvent}$ for the experimental T_{mono} values (Fig 3E). This yielded values of 23.9 $\mu m^2/s$ (AcGFP1), 11.8 $\mu m^2/s$ (AcGFP1^2), 8.59 $\mu m^2/s$ (AcGFP1^3), and 6.02 $\mu m^2/s$ (AcGFP1^4).

The mitochondrial matrix solvent reduces FP mobility in a manner compatible with macromolecular crowding

The obtained $D_{solvent}$ values (Fig 3E) reflect solvent-dependent FP diffusion in the mitochondrial matrix. To address our primary research question on macromolecular crowding, we first compared these values with empirical data sets of free 3D diffusion of globular biomolecules in aqueous media (Fig 4A; details are provided in Appendix Tables S2 and S3). The LOG10 ($D_{solvent}$) value of these molecules decreased linearly as a function of their LOG10 (MW) value, with a slope of −0.36 (Fig 4B). The latter is compatible with the theoretical proportionality of $D_{solvent}$ with the molecular radius, and hence $MW^{-0.33}$, for globular molecules (Dross *et al*, 2009). Analysis of EGFP concatemer diffusion in aqueous solution suggested that these molecules display a globular conformation, that is, the open blue circles (Fig 4A) appear to be on the line fitted for the globular proteins (black symbols). However, the underlying experimental studies provided evidence that EGFP concatemers display an elongated molecular structure in aqueous solution (Pack *et al*, 2006; Vámosi *et al*, 2014). Therefore, we added the EGFP concatemers to the data set of the elongated molecules in aqueous solution (Fig 4A; open and filled blue symbols). For elongated molecules (Saxton, 2014), $D_{solvent}$ decreased faster as a function of MW than for globular molecules (Fig 4A; black vs. blue line) and a slope of −0.72 was found (Fig 4B). The latter is compatible with experimental data for elongated (i.e., supercoiled) plasmid DNA molecules in dilute aqueous solution where $D_{solvent}$ is proportional to $MW^{-0.66}$ (Prazeres, 2008). Quantification of EGFP concatemer diffusion in HeLa cell nuclei and cytosol yielded steeper slopes relative to aqueous solution (Fig 4A; open red squares, filled red circles, and Fig 4B; open red bars). These slopes were relatively close to the theoretical value for elongated molecules (−0.66), suggesting that these EGFP concatemers displayed an elongated molecular structure. The latter was experimentally confirmed in the underlying studies (Pack *et al*, 2006; Dross *et al*, 2009). In case of mitochondrial matrix-targeted FPs, a slope of −0.98 was obtained (Fig 4A; filled red squares, and Fig 4B; filled red bar). This decline was faster than for globular molecules in aqueous solution (2.7-fold), elongated molecules in aqueous solution (1.4-fold), elongated EGFP concatemers in the HeLa cell nucleus (1.3-fold), and elongated EGFP concatemers in HeLa cytosol (1.5-fold). Of note, the LOG10 ($D_{solvent}$) value for AcGFP1^4 fell exactly on the fitted line (Fig 4A; filled red square for highest MW), supporting the validity of the applied T_{mono} correction (Fig 3B). Because the data points for the mitochondrial matrix-targeted FPs are not parallel to the "aqueous" lines for the globular and elongated molecules (Fig 4A and B), the steeper decline in $D_{solvent}$ for the matrix-targeted concatemers cannot be explained by differences in solvent viscosity. The steeper decline is also not due to cristae-induced diffusion hindrance, since $n_{cristae}$ was similar for AcGFP1- and AcGFP1^4-expressing cells (Table 1) and our modeling approach delivers cristae-independent $D_{solvent}$ values. Integrating the above results, we conclude that the MW-dependent mobility reduction of AcGFP1 concatemers in the mitochondrial matrix is not only due to their elongated structure but also involves macromolecular crowding.

Quantifying the viscosity of the mitochondrial matrix solvent and predicting FP structural conformation

To gain further insight into the structural conformation of the mitochondrial matrix-targeted FPs, we next determined mitochondrial matrix solvent viscosity ($\eta_{solvent}$). To this end, we applied four empirical equations allowing prediction of $\eta_{solvent}$ from $D_{solvent}$ (Appendix Supplementary Methods): "Young" (Young *et al*, 1980), "He–Niemeyer" (He & Niemeyer, 2003), "Tyn–Gusek" (Tyn & Gusek, 1990), and "Stokes–Einstein" (Einstein, 1905; Sutherland, 1905; von Smoluchowski, 1906; Perrin, 1936). These equations also accounted for the effects of MW (Young, He–Niemeyer), radius of gyration (R_G; He–Niemeyer, Tyn–Gusek), and hydrodynamic radius (R_H; Stokes–Einstein) of the FPs. The MW of each concatemer was computed from its protein sequence (Appendix Table S1), whereas R_G and R_H were derived from structural information (see Table 1 and Fig EV1, and Appendix Supplementary Methods). In case of AcGFP1^2, AcGFP1^3, and AcGFP1^4, two extreme conformations of minimal size ("compact") and maximal size ("extended," i.e., elongated) were considered (Fig EV1B–G). The Young equation, which is independent of FP conformation, predicted that $\eta_{solvent}$ increased as a function of concatemer MW (Fig 4C; left panel). Similarly, when assuming that the FPs displayed a "compact" structural conformation also the He–Niemeyer, Tyn–Gusek and Stokes–Einstein equations predicted that $\eta_{solvent}$ increased as a function of MW (Fig 4C; middle panel). By contrast, the predicted $\eta_{solvent}$ values for AcGFP1^2, AcGFP1^3, and AcGFP1^4 were highly similar when assuming that these FPs displayed an "extended" structural conformation (Fig 4C; right panel). This strengthens our above conclusion that the FPs have an extended structure in the mitochondrial matrix solvent. The $D_{solvent}$ value of AcGFP1 is the most reliable and easy-to-interpret predictor of $\eta_{solvent}$ because AcGFP1-expressing cells display a single protein band (Fig 2B), and no assumptions regarding AcGFP1 structure are required (Fig EV1A). For AcGFP1 (Fig 4C; right panel) the He–Niemeyer, Tyn–Gusek, and Stokes–Einstein equations predicted $\eta_{solvent}$ values between 3.69 and 4.57 cP (dotted lines). Taken together, these results support the conclusion that AcGFP1^2, AcGFP1^3, and AcGFP1^4 have an elongated structural conformation in the mitochondrial matrix and that the mitochondrial matrix fluid displays a three to five-fold higher viscosity than water.

Chloramphenicol decreases the number of cristae, increases matrix electron density, and partially immobilizes matrix-targeted FPs

Although the above data provide evidence that FP diffusion in the mitochondrial matrix is reduced by macromolecular crowding, this effect appears to be relatively small. Therefore, we aimed to increase matrix macromolecular crowding levels by treating the cells with chloramphenicol (CAP), which inhibits the biosynthesis of mitochondrial DNA (mtDNA)-encoded OXPHOS subunits. The latter normally function as MIM-embedded binding platforms for

© 2023 The Authors

14602075, 2023, 7, Downloaded from https://www.embopress.org/doi/10.15252/embj.2021108533 by Wageningen University and Research Bibliotheek, Wiley Online Library on [11/08/2023]. See the Terms and Conditions (https://onlinelibrary.wiley.com/terms-and-conditions) on Wiley Online Library for rules of use; OA articles are governed by the applicable Creative Commons License

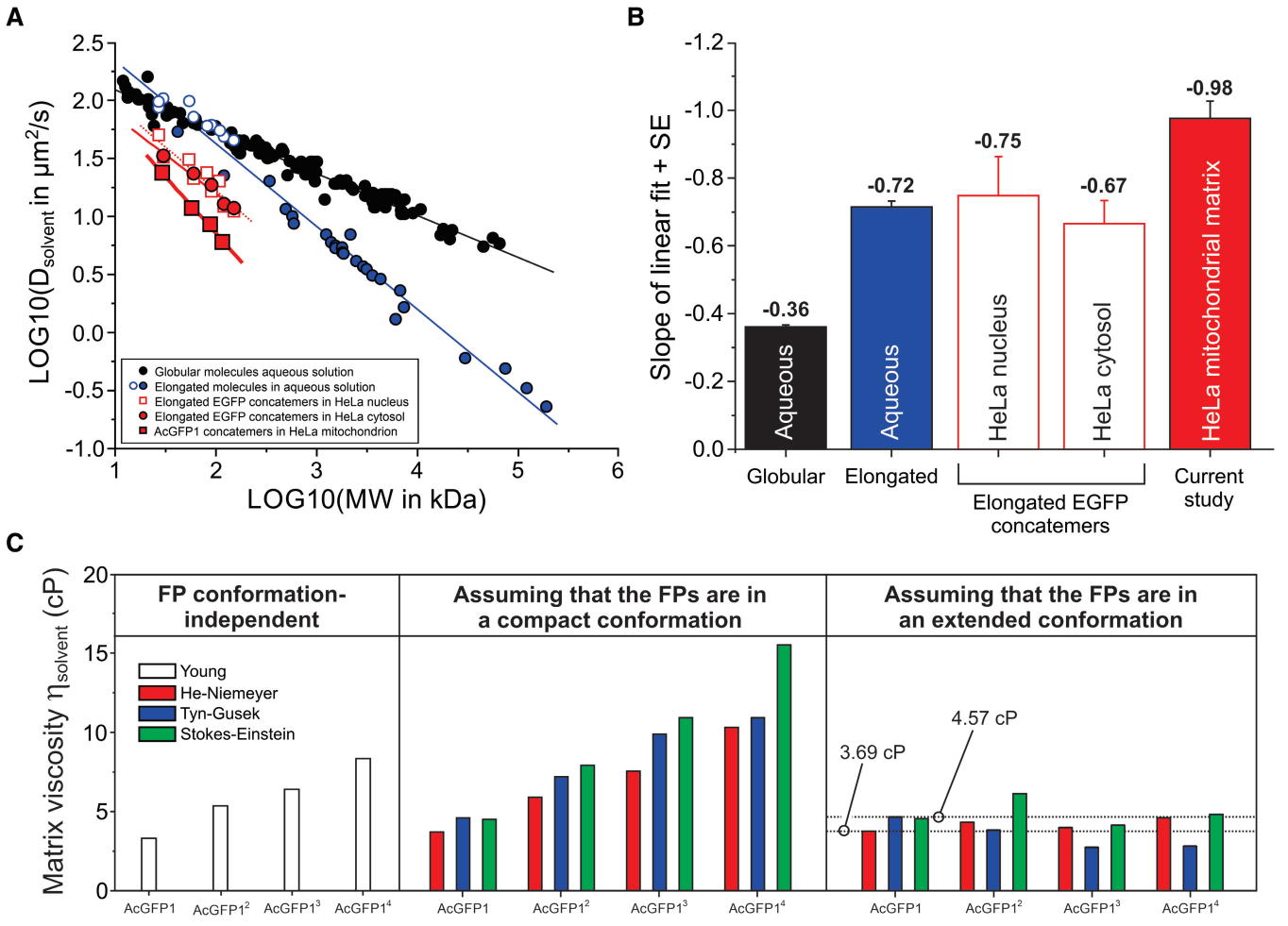

Figure 4. Relationship between $D_{solvent}$ and MW for the mitochondrial matrix-targeted fluorescent proteins, viscosity analysis and protein structure prediction.

A Linear relationship between experimental $D_{solvent}$ and MW values for various biomolecules in a double logarithmic plot. Data obtained in aqueous solution is separated into globular biomolecules (filled black symbols; continuous black line), elongated EGFP concatemers (open blue symbols; continuous blue line) and elongated biomolecules (filled blue symbols; continuous blue line). Red symbols reflect intracellular diffusion measurements with EGFP concatemers in HeLa cell nuclei (open red squares; dotted red line), EGFP concatemers in HeLa cytosol (filled red circles; continuous thin red line) and AcGFP1 concatemers in the mitochondrial matrix (filled red squares; continuous thick red line; current study). Full numerical data, fitting parameters using (LOG10 ($D_{solvent}$) = A + B·LOG10 (MW) and background information are provided in Appendix Tables S2 and S3.

B Slopes of the linear fits depicted in panel (A) for the different classes of biomolecules measured in aqueous solution and intracellular compartments. Individual bars reflect mean ± SE (standard error) values from the linear fit.

C The viscosity of the mitochondrial matrix solvent ($\eta_{solvent}$) was calculated from the $D_{solvent}$ values of the FPs using four empirical equations (Young, He–Niemeyer, Tyn–Gusek and Stokes–Einstein). This allowed the prediction of $\eta_{solvent}$ as well as FP structural conformation ("compact" or "extended"; Fig EV1). The estimated $\eta_{solvent}$ ranged between 3.69 and 4.57 cP. See Results for details.

nDNA-encoded OXPHOS subunits and/or assembly intermediates during OXPHOS biogenesis (Guerrero-Castillo *et al*, 2017; Hock *et al*, 2020). As such, CAP treatment induces the formation of stable subassemblies of mitochondrial CI with MWs of 170-, 67-, and 72-kDa (Guerrero-Castillo *et al*, 2017). Compositional analysis of these subassemblies demonstrated that the 72-kDa subassembly consisted of the NDUFV1 and NDUFV2 subunit. Previous analysis of mitochondrial matrix protein diffusion in HEK293 cells demonstrated that CAP treatment: (i) particularly increased the F_m of AcGFP1-tagged NDUFV1 subunits and/or NDUFV1-containing assembly intermediates, (ii) slowed the FRAP rate of AcGFP1 and AcGFP1^2, and (iii) did not slow the FRAP rate of the integral MIM protein adenine nucleotide translocase 1 (ANT1; Dieteren *et al*, 2011b). This demonstrates that NDUFV1 subunits and/or NDUFV1-containing subassemblies are not MIM-attached but diffusing in the mitochondrial matrix solvent. Considering the currently known mechanisms of OXPHOS biogenesis (Hock *et al*, 2020; Fernández-Vizarra & Ugalde, 2022), it is to be expected that CAP treatment also increases the amount of nDNA-encoded subunits and/or assembly intermediates from other OXPHOS complexes (i.e., III, IV, and V) in the matrix solvent. CAP treatment did not alter mitochondrial dimensions and FP expression patterns (Table 1 and Appendix Fig S1B).

© 2023 The Authors

14602075, 2023, 7, Downloaded from https://www.embopress.org/doi/10.15252/embj.2021108533 by Wageningen University and Research Bibliotheek, Wiley Online Library on [11/08/2023]. See the Terms and Conditions (https://onlinelibrary.wiley.com/terms-and-conditions) on Wiley Online Library for rules of use; OA articles are governed by the applicable Creative Commons License

EM analysis demonstrated that the number of cristae/µm was ~two-fold reduced (Fig 5A and B, and Table 1), compatible with previous studies in HeLa and HEK293 cells (Lenk & Penman, 1971; Kislev *et al*, 1973; Dieteren *et al*, 2011b). Moreover, the mitochondrial matrix was more electron-dense in CAP-treated cells (Fig 5C). The FRAP signal recovered slower, that is, T_{mono} was larger for all FPs in CAP-treated relative to untreated cells (Fig 5D and E, and Table 1). CAP treatment further induced a substantial decrease in F_m (Fig 5D and Table 1) and F_∞ (i.e., the predicted FP fluorescence intensity at $t = t_\infty$; Fig 5F), in particular for AcGFP1^2 and AcGFP1^3. By contrast, CAP treatment was much less effective in reducing T_{mono}, F_m, and F_∞ for AcGFP1^4, compatible with the detected fluorescent degradation product of smaller MW (Appendix Fig S1B). CAP-treated AcGFP1^2- and AcGFP1^3-expressing cells displayed a substantial decrease in F_m and F_∞, which could not be quantitatively reproduced by the BD simulation model (Appendix Fig S3). In light of the above, prediction of $D_{solvent}$ values for AcGFP1^2, AcGFP1^3, and AcGFP1^4 using BD simulations was not possible. However, AcGFP1 displayed T_{mono} and F_m values that were still reasonably compatible with BD simulations, predicting a $D_{solvent}$ of 2.91 µm^2/s for an experimental $n_{cristae}$ value of 9 (Table 1; Appendix Fig S3C and D). This predicted an $\eta_{solvent}$ value between 27.3 and 37.5 cP (Fig 5G

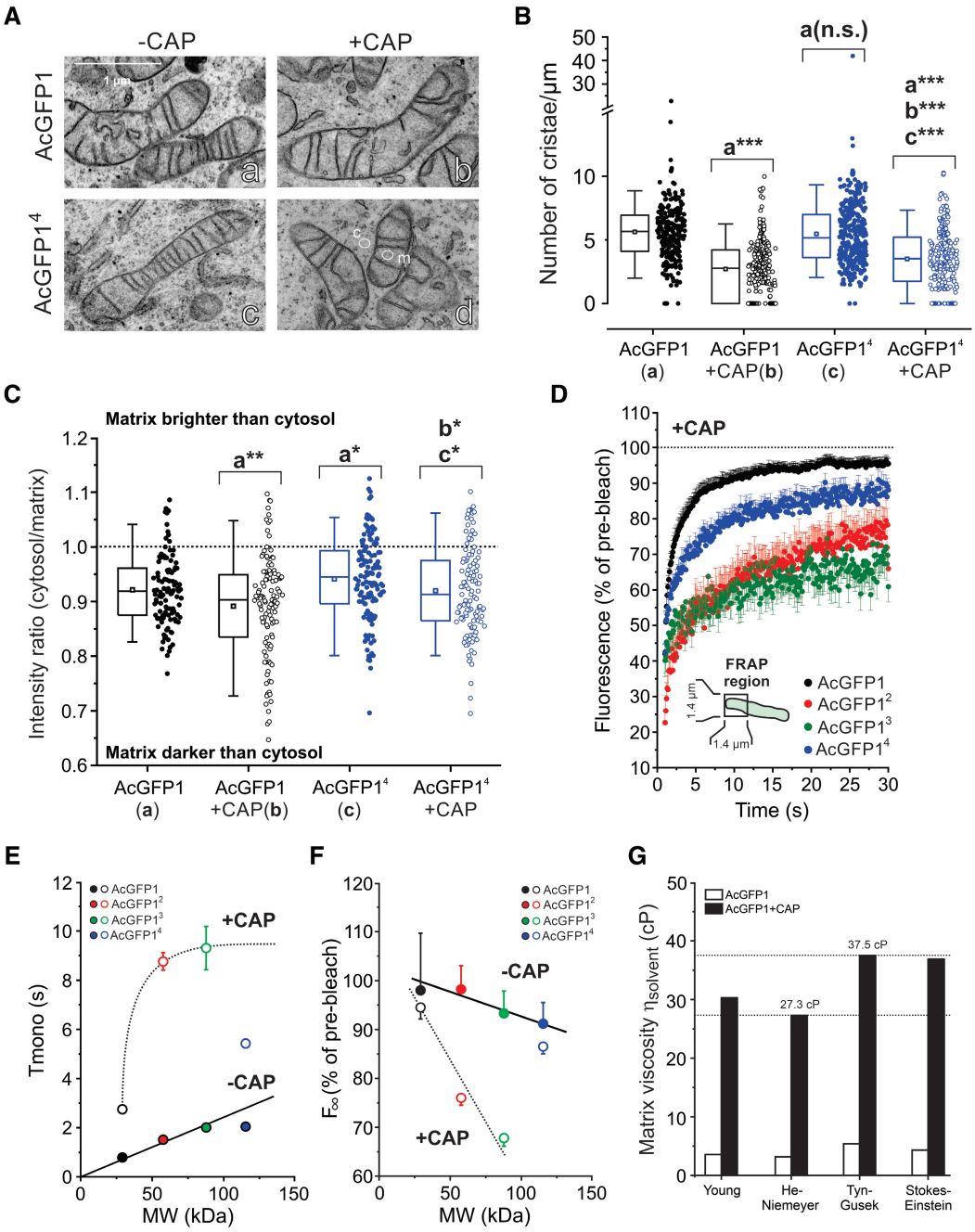

Figure 5.

© 2023 The Authors

14602075, 2023, 7, Downloaded from https://www.embopress.org/doi/10.15252/embj.2021108533 by Wageningen University and Research Bibliotheek, Wiley Online Library on [11/08/2023]. See the Terms and Conditions (https://onlinelibrary.wiley.com/terms-and-conditions) on Wiley Online Library for rules of use; OA articles are governed by the applicable Creative Commons License

Figure 5. Chloramphenicol decreases the number of cristae, increases matrix electron density, reduces the mobility of mitochondrial matrix-targeted fluorescent proteins and increases matrix viscosity.

A Transmission electron microscopy (EM) images of AcGFP1 and AcGFP1^4-expressing HeLa cells cultured in the absence and the presence of chloramphenicol (CAP). Images were contrast-optimized to better visualize cristae. Cytosolic and mitochondrial regions of interest typically used for electron density analysis (panel C) are marked by "c" and "m," respectively.

B Effect of CAP on the average number of cristae/μm calculated by dividing the number of cristae by the mitochondrial length for individual mitochondria. Data was obtained in $N = 2$ independent EM experiments for $n = 244$ mitochondria (AcGFP1), $n = 295$ (AcGFP1 + CAP), $n = 314$ (AcGFP1^4) and $n = 259$ (AcGFP1^4 + CAP).

C Effect of CAP on the electron density of the mitochondrial matrix quantified from EM images (original images were used). The y-axis depicts the intensity ratio between a cytosolic region of interest (ROI; e.g., panel A-d, marked "c") and a close by ROI in the mitochondrial matrix (e.g., panel A-d, marked "m"). Equal intensities of these ROIs are marked by the dotted line. Only mitochondria with clearly visible cristae (i.e., that were fully within the EM section) were included ($N = 2$ independent experiments) from $n = 112$ mitochondria (AcGFP1), $n = 119$ (AcGFP1 + CAP), $n = 134$ (AcGFP1^4) and $n = 116$ (AcGFP1^4 + CAP).

D Average FRAP curves (mean ± SEM) for mitochondrial matrix-targeted FPs in the presence of CAP (Table 1). Data was obtained in at least $N = 3$ independent experiments for $n = 40$ mitochondria (AcGFP1 + CAP), $n = 24$ (AcGFP1^2 + CAP), $n = 26$ (AcGFP1^3 + CAP) and $n = 33$ (AcGFP1^4 + CAP).

E Relationship between MW and T_{mono} in the absence of CAP (−CAP; data taken from Fig 3B) and in the presence of CAP (+CAP; curve manually drawn). Symbols and error bars reflect mean ± SE (standard error) values from the mono-exponential fit. For data points without error bar, the latter fell within the size of the symbol.

F Same as panel (E) but now for the relationship between MW and the fluorescence intensity (F_∞) of the FPs by extrapolating the fitted exponential recovery to $t = t_\infty$ (lines manually drawn). Symbols and error bars for F_∞ reflect mean ± SEM and were computed from the mono-exponential fit parameters as described in Table 1.

G Impact of CAP on the solvent-dependent viscosity ($\eta_{solvent}$) of the mitochondrial matrix fluid determined using the $D_{solvent}$ values of AcGFP1 (see Results for details). The estimated $\eta_{solvent}$ ranged between 27.3 and 37.5 cP.

Data information: In panels (B and C) each symbol represents an individual mitochondrion, error bars mark the 95% (upper) and 5% (lower) percentile, the boundary boxes mark the 75% (upper) and 25% (lower) percentile, the square marks the mean value of the data, and the horizontal line within the box indicates the median value of the data. Data in panel (B and C) was compared using an independent Student's *t*-test and significant differences are indicated by $*P < 0.05$, $**P < 0.01$, $***P < 0.001$ between the marked conditions (a–c). Not significant is marked by n.s. The exact *P*-values for panel (B) were: AcGFP1 (a) vs. AcGFP1 + CAP (b): $P = 1.894 \cdot 10^{-40}$; AcGFP1 (a) vs. AcGFP1^4 + CAP: $P = 1.458 \cdot 10^{-21}$; AcGFP1 + CAP (b) vs. AcGFP1^4 + CAP: $P = 4.846 \cdot 10^{-5}$; AcGFP1^4 (c) vs. AcGFP1^4 + CAP: $P = 2.725 \cdot 10^{-16}$. The exact *P*-values for panel (C) were: AcGFP1 (a) vs. AcGFP1 + CAP (b): $P = 0.00545$; AcGFP1 (a) vs. AcGFP1^4 (c): $P = 0.0348$; AcGFP1 + CAP (b) vs. AcGFP1^4 + CAP: $P = 0.0142$; AcGFP1^4 (c) vs. AcGFP1^4 + CAP: $P = 0.0366$.

and Table 1). Collectively, our FRAP analysis of CAP-treated cells demonstrates that mitochondrial matrix-targeted FPs become progressively immobilized as a function of MW, associated with an eightfold increase in $\eta_{solvent}$. These phenomena are compatible with increased macromolecular crowding.

Chloramphenicol impairs mitochondrial function, but neither induces the mitochondrial unfolded protein response, not alters mtDNA copy number and mitochondrial fission/fusion protein levels

Evidence in the literature suggests that both DOX and CAP inhibit mitochondrial function, thereby potentially inducing the mitochondrial unfolded protein response (UPR^{mt}; Houtkooper *et al*, 2013; Moullan *et al*, 2015; Shpilka & Haynes, 2018). The latter is classically linked to the accumulation of misfolded proteins in the mitochondrial matrix, which could hinder FP diffusion in our experiments by increasing macromolecular crowding. In case of DOX, cellular oxygen consumption rate (OCR) was not reduced (Appendix Supplementary Results and Fig EV2A–C) and the levels of proteinaceous UPR^{mt}-linked markers (LONP1, mtHSP70, mtHSP60, CLPP, and CHOP) were not affected (Figs EV2E, and EV3A and B). This makes it unlikely that DOX treatment induces mitochondrial dysfunction and UPR^{mt} in our experiments. CAP treatment greatly reduced OCR values and increased extracellular acidification rate (ECAR), potentially suggesting induction of a glycolytic switch (Schmidt *et al*, 2021; Bulthuis *et al*, 2022; Divakaruni & Jastroch, 2022). Further analysis demonstrated that CAP-treated cells do not display UPR^{mt} activation (Appendix Supplementary Results and Fig EV2A–C) and exhibit lower and higher TMRM fluorescence signals in the nucleus and mitochondrion, respectively (Appendix Supplementary Results and Fig EV2D). The latter suggests that CAP induces mitochondrial membrane potential ($\Delta\psi$) hyperpolarization. FP diffusion might potentially be altered by changes in mtDNA organization and the function of the mitochondrial MIM fusion protein Optic Atrophy 1 (OPA1). However, no CAP-induced changes in mtDNA copy number and expression of mitochondrial fission/fusion proteins were detected (Appendix Supplementary Results, and Fig EV2F and G). The latter is compatible with CAP not altering mitochondrial length and diameter. Taken together, these results suggest that the progressive FP immobilization observed in CAP-treated cells is neither caused by UPR^{mt} induction nor by alterations in the level of mtDNA and mitochondrial fission/fusion proteins. This supports our conclusion that CAP treatment affects FP mobility by increasing macromolecular crowding.

Discussion

The primary aim of this study was to determine whether the mitochondrial matrix solvent displays macromolecular crowding. To this end, we studied the diffusional behavior of four inert monomeric FPs of increasing MW in the mitochondrial matrix of HeLa cells in the absence and presence of CAP. Mitochondrial FP fluorescence intensity per cell decreased as a function of concatemer MW (Fig 2C) and correlated well with in-gel fluorescence signals (Fig 2D). This strongly suggests that the latter signals faithfully reflect the cellular situation and that AcGFP1 concatemers are not denatured during mitochondrial isolation. Similar to the current findings, the fluorescence signal and expression of nucleus-targeted EGFP concatemers (containing up to 12 monomers) decreased as a function of MW in H1299 cells (Böhm *et al*, 2017). The latter study also demonstrated the presence of minor amounts of fluorescent degradation products of smaller MW. Similarly, expression of EGFP concatemers in *Escherichia coli* cytoplasm (containing up to eight monomers) was paralleled with the formation of degradation

© 2023 The Authors

14602075, 2023, 7, Downloaded from https://www.embopress.org/doi/10.15252/embj.2021108533 by Wageningen University and Research Bibliotheek, Wiley Online Library on [11/08/2023]. See the Terms and Conditions (https://onlinelibrary.wiley.com/terms-and-conditions) on Wiley Online Library for rules of use; OA articles are governed by the applicable Creative Commons License

products of smaller MW (Nenninger *et al*, 2010). By contrast, FP concatemers of up to four EGFP molecules remained intact when expressed in the nucleus of HeLa cells (Dross *et al*, 2009), whereas concatemers of up to five EGFP molecules remained intact in the cytosol of HEK293 cells (Pack *et al*, 2006). Inspection of MW marker positions (Appendix Fig S1A and B) revealed that AcGFP1-expressing cells contained a single fluorescent product with an estimated MW between 25 and 37 kDa (predicted: 29-kDa; Table 1). The fluorescent product in AcGFP1^2-expressing cells displayed an MW between 37 and 50 kDa (predicted: 58-kDa). For AcGFP1^3 a product of 50–75 kDa was observed (predicted: 88-kDa). In case of AcGFP1^4 (predicted: 115-kDa), two fluorescent products with MWs between 37 and 50 kDa (smaller product) and 75–100 kDa (larger product) were detected. With the exception of AcGFP1, these data highlight a discrepancy between the marker-reported MW of the FPs and their predicted MW. This is probably due to the fact that the structural dimensions of the FPs, which co-determine gel migration distance, scale differently with their MW than for the MW markers. Moreover, SDS binding to the various FPs might be different, since samples were not heated (to prevent FP fluorescence loss), thereby affecting their migration behavior. In this context, our SDS–PAGE analysis suggests that the smaller fluorescent product in AcGFP1^4-expressing cells is similar to AcGFP1^2. This might indicate that AcGFP1^4, once imported in the mitochondrial matrix, is cleaved by a mitochondrial protease at the position of its 2nd linker (DIPPHPA-FLYKVVDDPPV; Appendix Table S1). However, an identical linker connected the 1st and 2nd AcGFP1 monomer within AcGFP1^3 but no fluorescent breakdown product was detected. This suggests that the size and/or MW of AcGFP1^4 is responsible for its partial breakdown within mitochondria, in both the presence and absence of CAP.

Viscosity of the mitochondrial matrix solvent in the absence of CAP

Analysis of AcGFP1 experiments predicted a $D_{solvent}$ of 23.9 $\mu m^2/s$ (Fig 3E). This is within the range of previous FP-employing FRAP and fluorescence correlation spectroscopy (FCS) studies (Partikian *et al*, 1998; Verkman, 2002; Koopman *et al*, 2007, 2008b; Dieteren *et al*, 2011a). Free EGFP in aqueous solution displayed a $D_{solvent}$ value between 87 and 104 $\mu m^2/s$ (Appendix Table S2). This means that the $D_{solvent}$ of AcGFP1 is between 3.6- and 4.4-fold lower in the mitochondrial matrix than in aqueous solution. As a consequence, computed matrix $\eta_{solvent}$ values were between 3.69 and 4.57 cP (Fig 4C), being three to five-fold higher than pure water and similar to those observed previously in HEK293 cells (Dieteren *et al*, 2011a) and *E. coli* cytoplasm (Chen *et al*, 2018). In the literature, mitochondrial matrix viscosity was also analyzed using viscosity-sensitive fluorescent rotor molecules (Xiao *et al*, 2021; Yin *et al*, 2021). In the case of HeLa cells, these studies reported heterogeneous and relatively high viscosity values between 20.7 and 275 cP (Yang *et al*, 2013; Jímenez-Sánchez *et al*, 2018; Ren *et al*, 2018, 2020; Steinmark *et al*, 2019). Similarly, variable high mitochondrial viscosity values between < 100 and > 900 cP were reported in rat hepatic tissue slices (Liu *et al*, 2018), whereas COS7 cells displayed a viscosity value of 325 cP, measured with a BODIPY-HaloTag rotor molecule targeted to mitochondria using the mitochondrial Cox8a targeting sequence (Chambers *et al*, 2018). It is currently unknown why the rotor-based viscosity values exceed those reported in the current study and earlier FP-based research (Partikian *et al*, 1998; Verkman, 2002; Koopman *et al*, 2007, 2008b; Dieteren *et al*, 2011a). Potentially, the observed discrepancy in cP values could be due to the BODIPY and/or TPP^+-containing part of the rotors displaying a (transient) physical or electrochemical interaction with the inside-negative MIM. In this context, and to the best of our knowledge, there is currently no information regarding the translational mobility of these rotors in the mitochondrial matrix. Therefore, the rotor properties in the mitochondrial matrix might differ from those in solution, meaning that the viscosity reporting behavior of the sensor is altered (Puchkov, 2013; Chen *et al*, 2018). This hypothesis is supported by the observation that some of the rotor-reported matrix viscosities are close to that of the MIM (i.e., 900–950 cP; Chazotte & Hackenbrock, 1988) and that a plasma membrane-directed BODIPY-based rotor-reported viscosity values between 270 and 380 cP (Kubankova *et al*, 2019). This means that the rotor-reported mitochondrial matrix viscosity values are similar to those of the plasma membrane, which is unrealistic. It was further argued that accurate viscosity analysis with BODIPY-C_{10}-based probes requires calibration in the same polarity environment as the sample of interest and that the size of the surrounding molecules should not exceed that of BODIPY-C_{10} (Polita *et al*, 2020). We here demonstrate that CAP-induced impairment of mitochondrial function is associated with an eightfold increase in $\eta_{solvent}$ (Fig 5G). Therefore, differences in rotor- and FP-reported matrix viscosities might also be due to inter-study differences in mitochondrial functional state.

Evidence for matrix macromolecular crowding in the absence of CAP

Applying empirical relationships, we provided evidence that AcGFP1^2, AcGFP1^3 and AcGFP1^4 display an elongated (structurally extended) conformation in the mitochondrial matrix solvent (Fig 4C). Similarly, EGFP concatemers displayed an elongated structure in the nucleus and cytosol of HeLa cells (Pack *et al*, 2006; Dross *et al*, 2009). This is compatible with the behavior of single DNA molecules in nanochannels, which displayed an elongated structure at low crowding levels but, when exceeding a certain volume fraction of the crowding agent, condensed into a compact form (Zhang *et al*, 2009). Interestingly, analyzing the dependency of $D_{solvent}$ on MW revealed a steeper linear decline for matrix-targeted FPs, than for globular/elongated molecules in aqueous solution and elongated EGFP concatemers in the nucleus/cytoplasm of HeLa cells (Fig 4B). This means that the elongated structure of the matrix-targeted FPs cannot fully explain the steeper decline. In addition, our BD modeling approach renders $D_{solvent}$ cristae-independent and both F_m and F_∞ increased as a function of MW (Table 1 and Fig 5F). Therefore, we conclude that matrix FP mobility is reduced by the combined impact of their elongated structure and macromolecular crowding. This latter probably is low level, since substantial crowding is associated with molecule compaction (Zhang *et al*, 2009; Kuznetzova *et al*, 2014).

CAP treatment slows solute diffusion and increases mitochondrial matrix viscosity

Triggered by our previous findings (see Results), cells were treated with CAP to increase the protein concentration of the matrix

© 2023 The Authors

14602075, 2023, 7, Downloaded from https://www.embopress.org/doi/10.15252/embj.2021108533 by Wageningen University and Research Bibliotheek, Wiley Online Library on [11/08/2023]. See the Terms and Conditions (https://onlinelibrary.wiley.com/terms-and-conditions) on Wiley Online Library for rules of use; OA articles are governed by the applicable Creative Commons License

solvent. Although technical limitations prevented assessing $D_{solvent}$ for AcGFP1[2], AcGFP1[3], and AcGFP1[4], analysis of AcGFP1 mobility demonstrated that CAP treatment eightfold decreased and increased $D_{solvent}$ and $\eta_{solvent}$, respectively (Table 1 and Fig 5G). By itself, this viscosity increase is highly relevant, since it will slow down any diffusion-limited process, including metabolite diffusion and macromolecular association/dissociation reactions (Van den Bogaart *et al*, 2007; Molines *et al*, 2022). Mitochondria in CAP-treated cells displayed a progressive immobilization of AcGFP1[2] and AcGFP1[3] (Fig 5D–F), contained three to five-fold cristae and displayed a more electron-dense matrix (Fig 5C). This strongly suggests that matrix macromolecular crowding is increased in CAP-treated cells (Mika *et al*, 2010; Mittal *et al*, 2015; Delarue *et al*, 2018; Junker *et al*, 2019). Electron density analysis was performed on EM images of osmium tetroxide-treated samples, which preferentially binds to unsaturated fatty acids (Belazi *et al*, 2009). However, it appears that osmium tetroxide also can react with proteins (e.g., Porter & Kallman, 1953) and that electron density increases when proteins with a relatively high affinity for this fixative are present (Bisht *et al*, 2016). In this context, it has been argued that differences in electron density of cryo-electron tomograms can be interpreted as differences in macromolecular density and that mitochondrial matrices are expected to display a higher density than the surrounding cytoplasm (Ader *et al*, 2019). Therefore, we propose that the increased electron density in CAP-treated cells (Fig 5C) represents a minor though significant increase in the concentration of soluble matrix macromolecules. This conclusion is supported by the fact that mitochondria in AcGFP1[4]-expressing cells displayed a lower fluorescent signal (Fig 2B–D), as well as a less electron-dense matrix relative to AcGFP1-expressing cells (Fig 5C). Compatible with a previous study in CAP-treated mouse embryonic fibroblasts (Sasaki *et al*, 2020), CAP-treated HeLa cells lacked a detectable increase in proteinaceous UPR^{mt}-linked markers (Figs EV2E and EV3). Although this suggests that the increase in matrix protein levels is relatively small, such an increase can substantially elevate macromolecular crowding levels due to the relatively small matrix volume.

CAP treatment does not induce mitochondrial orthodox-to-condensed transition

Classically, changes in matrix electron density are linked to alterations in mitochondrial bioenergetic state during mitochondrial "orthodox-to-condensed transition" (Hackenbrock, 1966, 1972). Orthodox mitochondria are characterized by a low OCR, $\Delta\psi$ hyperpolarization and a relatively large matrix volume, whereas condensed mitochondria display a high OCR and a relatively small matrix volume (Perkins & Ellisman, 2011). During orthodox-to-condensed transition, matrix volume decrease is accompanied by an increase in electron density without alterations in total mitochondrial volume (Hackenbrock, 1966). In CAP-treated cells, mitochondria displayed functional properties typical of orthodox mitochondria (i.e., a low OCR and $\Delta\psi$ hyperpolarization; Fig EV2A–D) but a more electron-dense (darker) matrix (typical of condensed mitochondria; Fig 5C). Although CAP did reduce the number of cristae, mitochondrial dimensions and volume were not detectably affected (Table 1). With respect to CAP-induced $\Delta\psi$ hyperpolarization, we observed that mitochondrial TMRM fluorescence was increased, whereas nucleoplasmic TMRM fluorescence was decreased. Since TMRM accumulates in the cytoplasm and mitochondrial matrix according to the plasma membrane and MIM electrical potential, respectively, this suggests that $\Delta\psi$ is more negative (Koopman *et al*, 2008a). Similarly, CAP pretreatment (48 h) induced $\Delta\psi$ hyperpolarization in HepG2 cells, as reported by fluorescence analysis of mitochondrial $DiOC_6$ accumulation (Li *et al*, 2005). However, when the rotational motion of fluorescent molecules is impeded their fluorescence quantum yield might increase (Dragan *et al*, 2014; Vyšniauskas *et al*, 2015). Therefore, it cannot be ruled out that the increased mitochondrial TMRM fluorescence signal in CAP-treated cells is due to a higher viscosity/crowding environment within the mitochondrial matrix. Taken together, our results indicate that CAP treatment might hyperpolarize $\Delta\psi$ and does not induce mitochondrial orthodox-to-condensed transition.

Predicting the degree of macromolecular crowding and volume exclusion in the mitochondrial matrix

As stated above, macromolecular crowding will reduce the translational mobility of solutes with a similar or larger size than the crowder to a greater extent than the mobility of smaller solutes. Therefore, to gain some theoretical insight into how CAP might quantitatively affect matrix crowding levels, we analyzed the predicted effect of human serum albumin (HSA) as a model crowding protein (Appendix Supplementary Results). HSA was selected because its MW (≈92-kDa) is relatively close to that of the expected NDUFV1/NDUFV2 assembly intermediates, potentially acting as (co)crowders (see Results), and similar to the MW of AcGFP1[3] (≈88-kDa), which was demonstrated to be substantially immobilized in CAP-treated cells. Using the obtained $\eta_{solvent}$ values, and assuming that HSA is the sole crowding entity, it was predicted that HSA would occupy between ~20% (absence of CAP) and ~33% (presence of CAP) of the total mitochondrial matrix volume (Appendix Supplementary Results and Fig 6A). Obviously, the magnitude of this volume exclusion effect will increase with the number/size of the crowding macromolecules and with decreasing matrix volume.

Summary and conclusion

The results presented in this study support the conclusion that the mitochondrial matrix solvent displays macromolecular crowding phenomena, particularly during conditions of CAP-induced mitochondrial dysfunction. In analogy to the cytosol (Delarue *et al*, 2018), it is therefore likely that (changes in) matrix crowding will induce molecular sieving effects that will affect matrix bioreactions dependent on the size of the involved crowding molecules and reactants. It is expected that macromolecular crowding will decrease the rate of diffusion-limited, fast association reactions whereas it will increase this rate for slow, transition-state-limited association reactions (Zhou *et al*, 2008). Therefore, crowding impacts on complex formation, surface binding, aggregation and folding/compaction of matrix proteins and, via volume exclusion, on the diffusion and (local) concentration of metabolites, ions, and other small reactants (Minton, 1990; Yu *et al*, 2016; Andrews, 2020). Crowding-induced effects on the Michaelis–Menten mechanism were predicted *in silico* (Weilandt & Hatzimanikatis, 2019) and demonstrated experimentally for the mitochondrial matrix enzymes malate hydrogenase

© 2023 The Authors

14602075, 2023, 7, Downloaded from https://www.embopress.org/doi/10.15252/embj.2021108533 by Wageningen University and Research Bibliotheek, Wiley Online Library on [11/08/2023]. See the Terms and Conditions (https://onlinelibrary.wiley.com/terms-and-conditions) on Wiley Online Library for rules of use; OA articles are governed by the applicable Creative Commons License

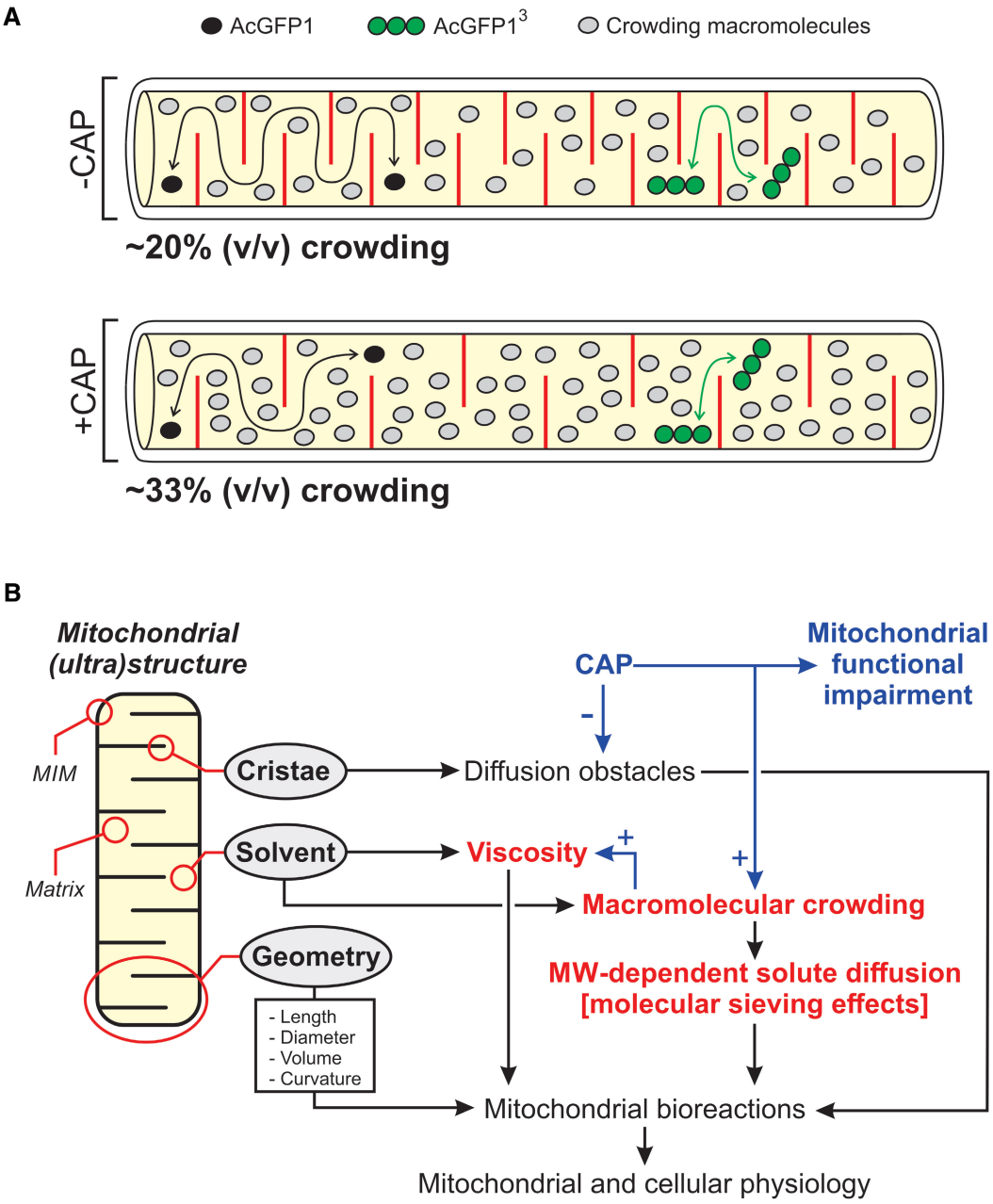

Figure 6. Key results and interplay between mitochondrial (ultra)structure, matrix solvent macromolecular crowding/viscosity and mitochondrial function.

A Graphical representation (not to scale) of the key results of this study, illustrating the hindrance effect of cristae (red lines) and crowding macromolecules (gray symbols) on the mobility of AcGFP1 (black symbols) and AcGFP1^3 (green symbols) in the mitochondrial matrix (yellow). In the absence of chloramphenicol (−CAP), low levels of macromolecular crowding reduce the mobility of AcGFP1^3 to a greater extent than the mobility of AcGFP1. In the presence of CAP (+CAP), the number of cristae is reduced but crowding is increased. This impedes the mobility of AcGFP1 and AcGFP^3, although the latter is affected to a greater extent. In this panel, the number of crowding macromolecules approximately reflects the predicted maximal degree of crowding determined using human serum albumin (HSA) as a model crowder (see Discussion).

B Integration of mitochondrial morphofunction. The mitochondrial matrix is surrounded by the mitochondrial inner membrane (MIM), which contains matrix-protruding folds (cristae). Biochemical reactions in the mitochondrial matrix are affected by hindrance of solute diffusion by cristae, the physicochemical properties of the mitochondrial matrix solvent (e.g., viscosity) and the geometry of the mitochondrial compartment (e.g., volume). We here demonstrate that the mitochondrial matrix solvent can reduce the diffusion of fluorescent proteins in an MW-dependent manner typical of macromolecular crowding. The latter appeared only minor during "normal" conditions but increased during CAP-induced mitochondrial functional impairment. We propose that crowding-induced molecular sieving effects, in combination with alterations in matrix solvent viscosity, impact on mitochondrial bioreactions and thereby on mitochondrial and cellular physiology.

© 2023 The Authors

14602075, 2023, 7, Downloaded from https://www.embopress.org/doi/10.15252/embj.2021108533 by Wageningen University and Research Bibliotheek, Wiley Online Library on [11/08/2023]. See the Terms and Conditions (https://onlinelibrary.wiley.com/terms-and-conditions) on Wiley Online Library for rules of use; OA articles are governed by the applicable Creative Commons License

(Poggi & Slade, 2015) and citrate synthase (Wilcox *et al*, 2020). We hypothesize that alterations in mitochondrial matrix crowding level, cristae number/architecture, and/or mitochondrial geometry exert control over mitochondrial bioreactions, which exemplifies the intricate link between mitochondrial (ultra)structure and function (Fig 6B). In this sense, the combined crowding and cristae-induced hindrance of matrix Ca^{2+} diffusion might be involved in heterogeneous spreading of mitochondrial Ca^{2+} signals (Gerencser & Adam-Vizi, 2005) and compartmentalization of matrix reaction networks (Kekenes-Huskey *et al*, 2015).

Materials and Methods

Generation of inducible HeLa cell lines

HeLa T-REx Flp-in cell lines stably expressing mitochondria-targeted concatemers of monomeric AcGFP1 ($AcGFP^1$, $AcGFP1^2$, $AcGFP1^3$, and $AcGFP1^4$) were generated as described in the Appendix Supplementary Methods and cultured at 37°C in a humid atmosphere (95% air, 5% CO_2). Expression of these fluorescent proteins (FPs) was induced by adding 1 μg/ml doxycycline (DOX) to the culture medium for 24 h. In certain experiments, cells were treated with 40 μg/ml chloramphenicol (CAP) for 72 h.

Mitochondrial staining and flow cytometry

Localization of the FPs and the mitochondrial marker MitoTracker Red CM-H_2XROS was visualized using confocal microscopy. Flow cytometry was applied to analyze the cellular fluorescence intensity of the AcGFP1 concatemers and forward scatter. Details are provided in the Appendix Supplementary Methods.

Fluorescence recovery after photobleaching (FRAP) analysis

Mitochondrial FRAP experiments were performed as described previously (Dieteren *et al*, 2008, 2009, 2011a, 2011b). Details are provided in the Appendix Supplementary Methods.

Western blotting

Mitochondrial fractions or whole-cell lysates were used for SDS–PAGE, in-gel fluorescence analysis, and Western blotting as described in the Appendix Supplementary Methods.

Electron microscopy (EM)

Electron microscopy was performed as described previously (Koopman *et al*, 2008a). Details are provided in the Appendix Supplementary Methods.

Functional cell analysis

Oxygen consumption rates (OCR) and extracellular acidification rates (ECAR) were quantified using a Seahorse XFe96 flux Analyzer (Agilent, Santa Clara, CA, USA). Mitochondrial membrane potential ($\Delta\psi$) was analyzed using the fluorescent cation TMRM (tetramethylrhodamine methyl ester). Mitochondrial DNA (mtDNA) copy number was quantified using real-time quantitative PCR (qPCR) analysis. Details are provided in the Appendix Supplementary Methods.

Numerical simulations

A Brownian dynamics (BD) computer model was developed to determine the solvent-dependent diffusion constant ($D_{solvent}$) of the AcGFP1 concatemers. This model was constrained by experimental data and implemented in GNU Fortran (https://gcc.gnu.org) under Ubuntu 20.04 LTS (https://releases.ubuntu.com). Details are provided in the Results section and in the Appendix Supplementary Methods.

Image analysis

Image visualization, processing, and quantification were carried out using Image Pro Plus software (Media Cybernetics, Rockville, MD, USA), Zeiss LSM 510 Meta software (Carl Zeiss AG, Oberkochen, Germany) and FIJI (https://imagej.net/Fiji).

Statistical analysis

Curve fitting and statistical analyses were performed using Origin Pro software (Originlab Corp., Northampton, MA, USA). Levenberg–Marquardt and least squares algorithms were used for nonlinear and linear regression, respectively. Average data were expressed as mean ± SEM (standard error of the mean), and significance was tested using an independent Student's *t*-test unless stated otherwise.

Data availability

Source data, materials, and computer code are available from the corresponding authors at reasonable request. All other data are contained in the main manuscript, Expanded View and Appendix. This study includes no data deposited in external repositories.

Expanded View for this article is available online.

Acknowledgements

We thank Stephen S. Taylor (Division of Cancer Sciences, University of Manchester, UK) for providing the parental HeLa T-REx Flp-in cells, Michael J. Saxton (Department of Biochemistry and Molecular Medicine, University of California, Davis, USA) for providing numerical data (Saxton, 2014), Laszlo Groh (Department of Internal Medicine, Radboudumc, The Netherlands) for assistance with OCR and ECAR measurements, Hanka Venselaar (Centre for Molecular and Biomolecular Informatics, Radboudumc, the Netherlands) for discussions on protein conformation, Riekelt H. Houtkooper (Amsterdam UMC, University of Amsterdam, Amsterdam, The Netherlands) for discussions on UPR^{mt} and Anna O. Chertkova (Section of Molecular Cytology and van Leeuwenhoek Centre for Advanced Microscopy, University of Amsterdam, The Netherlands) for cell culture. We thank the Radboudumc Microscopy Technology Center for equipment maintenance, training, and assistance with the FRAP and EM recordings. This work was supported by an equipment grant from NWO (Netherlands Organization for Scientific Research, No: 911-02-008). CEJD was supported by an NWO-VENI grant (#863.13.019). JB was supported by an EJP-RD grant ("CureMILS") through ZonMW (Netherlands Organisation for Health Research and Development; #463003001). WJHK was supported by a

© 2023 The Authors

14602075, 2023, 7, Downloaded from https://www.embopress.org/doi/10.15252/embj.2021108533 by Wageningen University and Research Bibliotheek, Wiley Online Library on [11/08/2023]. See the Terms and Conditions (https://onlinelibrary.wiley.com/terms-and-conditions) on Wiley Online Library for rules of use; OA articles are governed by the applicable Creative Commons License

junior researcher grant (EPB; Radboudmc, Nijmegen, The Netherlands), the Next Level Animal Sciences (NLAS) initiative ("Data and Models") of the Wageningen University (Wageningen, The Netherlands) and by Principal Investigator (PI) support funding (Radboudumc).

Author contributions

Elianne P Bulthuis: Formal analysis; supervision; validation; investigation; visualization; writing – original draft; writing – review and editing. **Cindy E J Dieteren:** Formal analysis; supervision; funding acquisition; validation; investigation; visualization; writing – original draft; writing – review and editing. **Jesper Bergmans:** Data curation; investigation; writing – review and editing. **Job Berkhout:** Formal analysis; investigation. **Jori A Wagenaars:** Formal analysis; investigation; visualization. **Els M A van de Westerlo:** Formal analysis; supervision; investigation; visualization. **Emina Podhumljak:** Investigation. **Mark A Hink:** Resources; formal analysis; supervision; investigation; writing – original draft. **Laura F B Hesp:** Investigation. **Hannah S Rosa:** Formal analysis; investigation. **Afshan N Malik:** Formal analysis; supervision; investigation; writing – original draft. **Mariska Kea-te Lindert:** Formal analysis; investigation; writing – original draft. **Peter H G M Willems:** Funding acquisition; writing – original draft. **Han J G E Gardeniers:** Writing – original draft; writing – review and editing. **Wouter K den Otter:** Conceptualization; resources; software; validation; visualization; methodology; writing – review and editing. **Merel J W Adjobo-Hermans:** Conceptualization; supervision; validation; investigation; visualization; writing – original draft; writing – review and editing. **Werner J H Koopman:** Conceptualization; data curation; formal analysis; supervision; funding acquisition; validation; visualization; methodology; writing – original draft; project administration; writing – review and editing.

Disclosure and competing interests statement

WJHK is an *ad hoc* scientific advisor of Khondrion B.V. (Nijmegen, The Netherlands). This SME had no involvement in the data collection, analysis and interpretation, writing of the manuscript, and in the decision to submit the manuscript for publication.

References

Ader NR, Hoffmann PC, Ganeva I, Borgeaud AC, Wang C, Youle RJ, Kukulski W (2019) Molecular and topological reorganizations in mitochondrial architecture interplay during Bax-mediated steps of apoptosis. *Elife* 8: e40712

Akabayov B, Akabayov SR, Lee SJ, Wagner G, Richardson CC (2013) Impact of macromolecular crowding on DNA replication. *Nat Commun* 4: 1615

Andrews SS (2020) Effects of surfaces and macromolecular crowding on bimolecular reaction rates. *Phys Biol* 17: 045001

Appelhans T, Richter CP, Wilkens V, Hess ST, Piehler J, Busch KB (2011) Nanoscale organisation of mitochondrial microcompartments revealed by combining tracking and localization microscopy. *Nano Lett* 12: 610 – 616

Belazi D, Sole-Domenech S, Johansson B, Schalling M, Sjovall P (2009) Chemical analysis of osmium tetroxide staining in adipose tissue using imaging ToF-SIMS. *Histochem Cell Biol* 132: 105 – 115

Bisht K, Sharma K, Lacoste B, Tremblay ME (2016) Dark microglia: why are they dark? *Commun Integr Biol* 9: e1230575

Boersma AJ, Zuhorn IS, Poolman B (2015) A sensor for quantification of macromolecular crowding in living cells. *Nat Methods* 12: 227 – 229

Böhm J, Thavaraja R, Giehler S, Nalaskowski MM (2017) A set of enhanced green fluorescent protein concatemers for quantitative determination of nuclear localization signal strength. *Anal Biochem* 533: 48 – 55

Bulthuis EP, Adjobo-Hermans M, Willems PHGM, Koopman WJH (2019) Mitochondrial morphofunction in mammalian cells. *Antioxid Redox Signal* 30: 2066 – 2109

Bulthuis EP, Einer C, Distelmaier F, Groh L, van Emst-de Vries SE, van de Westerlo E, van de Wal M, Wagenaars J, Rodenburg RJ, Smeitink JAM *et al* (2022) The decylTPP mitochondria-targeting moiety lowers electron transport chain supercomplex levels in primary human skin fibroblasts. *Free Radic Biol Med* 188: 434 – 446

Calvo SE, Mootha VK (2010) The mitochondrial proteome and human disease. *Annu Rev Genomics Hum Genet* 11: 25 – 44

Chambers JE, Kubánková M, Huber RG, López-Duarte I, Avezov E, Bond PJ, Marciniak SJ, Kuimova MK (2018) An optical technique for mapping microviscosity dynamics in cellular organelles. *ACS Nano* 12: 4398 – 4407

Chazotte B, Hackenbrock CR (1988) The multicollisional, obstructed, long-range diffusional nature of mitochondrial electron transport. *J Biol Chem* 263: 14359 – 14367

Chen E, Esquerra RM, Meléndez PA, Chandrasekaran SS, Kliger DS (2018) Microviscosity in *E coli* cells from time-resolved linear dichroism measurements. *J Phys Chem B* 122: 11381 – 11389

Cogliati S, Enriquez JA, Scorrano L (2016) Mitochondrial cristae: where beauty meets functionality. *Trends Biochem Sci* 41: 261 – 273

Cravens SL, Schonhoft JD, Rowland MM, Rodriguez AA, Anderson BG, Stivers JT (2015) Molecular crowding enhances facilitated diffusion of two human DNA glycosylases. *Nucleic Acids Res* 43: 4087 – 4097

Delarue M, Brittingham GP, Pfeffer S, Surovtsev IV, Pinglay S, Kennedy KJ, Schaffer M, Gutierrez JI, Sang D, Poterewicz G *et al* (2018) mTORC1 controls phase separation and the biophysical properties of the cytoplasm by tuning crowding. *Cell* 174: 338 – 349

Dey P, Bhattacherjee A (2019) Disparity in anomalous diffusion of proteins searching for their target DNA sites in a crowded medium is controlled by the size, shape and mobility of macromolecular crowders. *Soft Matter* 15: 1960 – 1969

Dieteren CEJ, Willems PHGM, Vogel RO, Swarts HG, Fransen J, Roepman R, Crienen G, Smeitink JAM, Nijtmans LGJ, Koopman WJH (2008) Subunits of mitochondrial complex I exist as part of matrix- and membrane-associated subcomplexes in living cells. *J Biol Chem* 283: 34753 – 34761

Dieteren CEJ, Koopman WJH, Nijtmans LGJ (2009) Tracing human mitochondrial complex I assembly by use of GFP-tagged subunits. *Methods Enzymol* 456: 133 – 151

Dieteren CEJ, Gielen SCAM, Nijtmans LGJ, Smeitink JAM, Swarts HG, Brock R, Willems PHGM, Koopman WJH (2011a) Solute diffusion is hindered in the mitochondrial matrix. *Proc Natl Acad Sci USA* 108: 8657 – 8662

Dieteren CEJ, Willems PHGM, Swarts HG, Fransen J, Smeitink JAM, Koopman WJH, Nijtmans LGJ (2011b) Defective mitochondrial translation differentially affects the live cell dynamics of complex I subunits. *Biochim Biophys Acta* 1807: 1624 – 1633

Divakaruni AS, Jastroch M (2022) A practical guide for the analysis, standardization and interpretation of oxygen consumption measurements. *Nat Metab* 4: 978 – 994

Dragan A, Graham AE, Geddes CD (2014) Fluorescence-based broad dynamic range viscosity probes. *J Fluoresc* 24: 397 – 402

Dross N, Spriet C, Zwerger M, Müller G, Waldeck W, Langowski J (2009) Mapping eGFP oligomer mobility in living cell nuclei. *PLoS ONE* 4: e5041

© 2023 The Authors

14602075, 2023, 7, Downloaded from https://www.embopress.org/doi/10.15252/embj.2021108533 by Wageningen University and Research Bibliotheek, Wiley Online Library on [11/08/2023]. See the Terms and Conditions (https://onlinelibrary.wiley.com/terms-and-conditions) on Wiley Online Library for rules of use; OA articles are governed by the applicable Creative Commons License

Einstein A (1905) Über die von der molekularkinetischen Theorie der Wärme geforderte Bewegung von in ruhenden Flüssigkeiten suspendierten Teilchen. *AdP* 322: 549 – 560

Fernández-Vizarra E, Ugalde C (2022) Cooperative assembly of the mitochondrial respiratory chain. *Trends Biochem Sci* 47: 999 – 1008

Fernie AR, Zhang Y, Sweetlove LJ (2018) Passing the baton: substrate channelling in respiratory metabolism. *Research* 2018: 1539325

Filippin L, Abad MC, Gastaldello S, Magelhães PJ, Sandonà D, Pozzan T (2005) Improved strategies for the delivery of GFP-based Ca^{2+} sensors into the mitochondrial matrix. *Cell Calcium* 37: 129 – 136

Fuentes-Lemus E, Reyes JS, Gamon LF, López-Alarcón C, Davies MJ (2021) Effect of macromolecular crowding on protein oxidation: consequences on the rate, extent and oxidation pathways. *Redox Biol* 48: 102202

Gerencser AA, Adam-Vizi V (2005) Mitochondrial Ca^{2+} dynamics reveals limited intramitochondrial Ca^{2+} diffusion. *Biophys J* 88: 698 – 714

Guerrero-Castillo S, Baertling F, Kownatzki D, Wessels HJ, Arnold S, Brandt U, Nijtmans LGJ (2017) The assembly pathway of mitochondrial respiratory chain complex I. *Cell Metab* 25: 128 – 139

Hackenbrock CR (1966) Ultrastructural bases for metabolically linked mechanical activity in mitochondria. I. Reversible ultrastructural changes with change in metabolic steady state in isolated liver mitochondria. *J Cell Biol* 30: 269 – 297

Hackenbrock CR (1972) Energy-linked ultrastructural transformations in isolated liver mitochondria and mitoplasts. *J Cell Biol* 53: 450 – 456

Haggie PM, Verkman AS (2002) Diffusion of tricarboxylic acid cycle enzymes in the mitochondrial matrix in vivo. *J Biol Chem* 277: 40782 – 40788

Hansen MMK, Mijer LHH, Spruijt E, Maas RJM, Ventosa Roquelles M, Groen J, Heus HA, Huck WTS (2016) Macromolecular crowding develops heterogeneous environments of gene expression in picoliter droplets. *Nat Nanotechnol* 11: 191 – 197

He L, Niemeyer B (2003) A novel correlation for protein diffusion coefficients based on molecular weight and radius of gyration. *Biotechnol Prog* 19: 544 – 548

Hochmair J, Exner C, Franck M, Dominguez-Baquero A, Diez L, Brognaro H, Kraushar ML, Mielke T, Radbruch H, Kaniyappan S *et al* (2022) Molecular crowding and RNA synergize to promote phase separation, microtubule interaction, and seeding of tau condensates. *EMBO J* 17: e108882

Hock DH, Robinson DRL, Stroud DA (2020) Blackout in the powerhouse: clinical phenotypes associated with defects in the assembly of OXPHOS complexes and the mitoribosome. *Biochem J* 477: 4085 – 4132

Houtkooper RH, Mouchiroud L, Ryu D, Moullan N, Katsyuba E, Knott G, Williams RW, Auwerx J (2013) Mitonuclear protein imbalance as a conserved longevity mechanism. *Nature* 497: 451 – 459

Hu C, Shu L, Huang X, Yu J, Li L, Gong L, Yang M, Wu Z, Gao Z, Zhao Y *et al* (2020) OPA1 and MICOS regulate mitochondrial crista dynamics and formation. *Cell Death Dis* 11: 940

Jímenez-Sánchez A, Lei EK, Kelley SO (2018) A multifunctional chemical probe for the measurement of local micropolarity and microviscosity in mitochondria. *Angew Chem Int Ed Engl* 57: 8891 – 8895

Joyner RP, Tang JH, Helenius J, Dultz E, Brune C, Holt LJ, Huet S, Müller DJ, Weis K (2015) A glucose-starvation response regulates the diffusion of macromolecules. *Elife* 5: e09376

Junker NO, Vaghefikia F, Albarghash A, Höfig H, Kempe D, Walter J, Otten J, Pohl M, Katranidid A, Wiegand S *et al* (2019) Impact of molecular crowding on translational mobility and conformational properties of macromolecules. *J Phys Chem B* 123: 447 – 4486

Kekenes-Huskey PM, Eun C, McCammon JA (2015) Enzyme localization, crowding, and buffers collectively modulate diffusion-influenced signal transduction: insights from continuum diffusion modelling. *J Chem Phys* 143: 094103

Kislev N, Spolsky CM, Eisenstadt JM (1973) Effect of chloramphenicol on the ultrastructure of mitochondria in sensitive and resistant strains of HeLa. *J Cell Biol* 57: 571 – 579

Koopman WJH, Hink MA, Verkaart S, Visch HJ, Smeitink JAM, Willems PHGM (2007) Partial complex I inhibition decreases mitochondrial motility and increases matrix protein diffusion as revealed by fluorescence correlation spectroscopy. *Biochim Biophys Acta* 1767: 940 – 947

Koopman WJH, Distelmaier F, Esseling JJ, Smeitink JAM, Willems PHGM (2008a) Computer-assisted live cell analysis of mitochondrial membrane potential, morphology and calcium handling. *Methods* 46: 304 – 311

Koopman WJH, Distelmaier F, Hink MA, Verkaart S, Wijers M, Fransen J, Smeitink JAM, Willems PHGM (2008b) Inherited complex I deficiency is associated with faster protein diffusion in the matrix of moving mitochondria. *Am J Physiol Cell Physiol* 294: C124 – C1132

Koopman WJH, Nijtmans LGJ, Dieteren CEJ, Roestenberg P, Valsecchi F, Smeitink JAM, Willems PHGM (2010) Mammalian mitochondrial complex I: biogenesis, regulation, and reactive oxygen species generation. *Antioxid Redox Signal* 12: 1431 – 1470

Kubankova M, Summers PA, Ljpez-Duarte I, Kiryushko D, Kuimova KM (2019) Microscopic viscosity of neuronal plasma membranes measured using fluorescent molecular rotors: effects of oxidative stress and neuroprotection. *ACS Appl Mater Interfaces* 11: 36307 – 36315

Kuznetzova IM, Turoverov KK, Uversky VN (2014) What macromolecular crowding can do to a protein. *Int J Mol Sci* 15: 23090 – 23140

Lenk R, Penman S (1971) Morphological studies of cells grown in the absence of mitochondrial-specific protein synthesis. *J Cell Biol* 49: 541 – 546

Li CH, Tzeng SL, Cheng YW, Kang JJ (2005) Chloramphenicol-induced mitochondrial stress increases p21 expression and prevents cell apoptosis through a p21-dependent pathway. *J Biol Chem* 280: 26193 – 26199

Liu F, Luo Y, Xu M (2018) Viscosity measurements using a two-photon ratiometric fluorescent sensor with two rotors. *Tetrahedron Lett* 59: 4540 – 4544

Lizana L, Konkoli Z, Bauer B, Jesorka A, Orwar O (2008) Controlling chemistry by geometry in nanoscale systems. *Annu Rev Phys Chem* 60: 449 – 468

Mika JT, van den Bogaart G, Veenhoff L, Krasnikov V, Poolman B (2010) Molecular sieving properties of the cytoplasm of *Escherichia coli* and consequences of osmotic stress. *Mol Microbiol* 77: 200 – 207

Minton AP (1990) Holobiochemistry: the effect of local environment upon the equilibria and rates of biochemical reactions. *Int J Biochem* 22: 1063 – 1067

Mittal S, Chowhan RK, Singh LR (2015) Macromolecular crowding: macromolecules friend or foe. *Biochim Biophys Acta* 1850: 1822 – 1831

Molines AT, Lemière J, Gazzola M, Steinmark IE, Edrington CH, Hsu CT, Real-Calderon P, Suhling K, Goshima G, Holt LJ *et al* (2022) Physical properties of the cytoplasm modulate the rates of microtubule polymerization and depolymerization. *Dev Cell* 57: 466 – 479

Moullan N, Mouchiroud L, Wang X, Ryu D, Williams EG, Mottis A, Jovaisaite V, Frochaux MV, Quiros PM, Deplancke B *et al* (2015) Tetracyclines disturb mitochondrial function across eukaryotic models: a call for caution in biomedical research. *Cell Rep* 10: 1681 – 1691

Nenninger A, Mastroianni G, Mullineaux CW (2010) Size dependence of protein diffusion in the cytoplasm of *Escherichia coli*. *J Bacteriol* 192: 4535 – 4540

Ölveczky BP, Verkman AS (1998) Monte Carlo analysis of obstructed diffusion in three dimensions: application to molecular diffusion in organelles. *Biophys J* 74: 2722 – 2730

© 2023 The Authors

14602075, 2023, 7, Downloaded from https://www.embopress.org/doi/10.15252/embj.2021108533 by Wageningen University and Research Bibliotheek, Wiley Online Library on [11/08/2023]. See the Terms and Conditions (https://onlinelibrary.wiley.com/terms-and-conditions) on Wiley Online Library for rules of use; OA articles are governed by the applicable Creative Commons License

Pack C, Saito K, Tamura M, Kinjo M (2006) Microenvironment and effect of energy depletion in the nucleus analyzed by mobility of multiple oligomeric EGFPs. *Biophys J* 91: 3921 – 3936

Papadopoulos S, Jürgens KD, Gros G (2000) Protein diffusion in living skeletal muscle fibers: dependence on protein size, fiber type, and contraction. *Biophys J* 79: 2084 – 2094

Partikian A, Olveczky B, Swaminathan R, Li Y, Verkman AS (1998) Rapid diffusion of green fluorescent protein in the mitochondrial matrix. *J Cell Biol* 140: 821 – 829

Perkins GA, Ellisman MH (2011) Mitochondrial configurations in peripheral nerve suggest differential ATP production. *J Struct Biol* 173: 117 – 127

Perrin F (1936) Mouvement Brownien d'un ellipsoide (II). Rotation libre et dépolarisation des fluorescences. Translation et diffusion de molécules ellipsoidales. *J Phys Radium* 7: 1 – 11

Poggi CG, Slade KM (2015) Macromolecular crowding and the steady-state kinetics of malate dehydrogenase. *Biochemistry* 54: 260 – 267

Polita A, Toliautas S, Žvirblis R, Vyšniauskas A (2020) The effect of solvent polarity and macromolecular crowding on the viscosity sensitivity of a molecular rotor BODIPY-C_{10}. *Phys Chem Chem Phys* 16: 8296 – 8303

Porter KR, Kallman F (1953) The properties and effects of osmium tetroxide as a tissue fixative with special reference to its use for electron microscopy. *Exp Cell Res* 4: 127 – 141

Prazeres DMF (2008) Prediction of diffusion coefficients of plasmids. *Biotechnol Bioeng* 99: 1040 – 1044

Puchkov EO (2013) Intracellular viscosity: methods of measurement and role in metabolism. *Biochem (Mosc) Suppl A Membr Cell Biol* 7: 279

Rath S, Sharma R, Gupta R, Ast T, Chan C, Durham JH, Goodman RP, Grabarek Z, Haas ME, Hung WHW *et al* (2021) MitoCarta 3.0: an updated mitochondrial proteome now with sub-organelle localization and pathway annotations. *Nucl Acids Res* 49: D1541 – D1547

Ren M, Zhou K, Wang L, Liu K, Lin W (2018) Construction of a ratiometric two-photon fluorescent probe to monitor the changes of mitochondrial viscosity. *Sens Actuators B* 262: 452 – 459

Ren M, Xu Q, Wang S, Liu L, Kong F (2020) A biotin-guided fluorescent probe for dual-mode imaging of viscosity in cancerous cells and tumor tissues. *Chem Commun* 56: 13351 – 13354

Rivas G, Minton AP (2016) Macromolecular crowding *in vitro*, *in vivo* and in between. *Trends Biochem Sci* 41: 970 – 981

Robinson JB, Srere PA (1985) Organization of Krebs Tricarboxylic acid cycle enzymes in mitochondria. *J Biol Chem* 260: 10800 – 10805

Sasaki K, Uchiumi T, Toshima T, Yagi M, Do Y, Hirai H, Igami K, Gotoh K, Kang D (2020) Mitochondrial translation inhibition triggers ATF4 activation, leading to integrated stress response but not to mitochondrial unfolded protein response. *Biosci Rep* 40: BSR20201289

Saxton MJ (2014) Wanted: scalable tracers for diffusion measurements. *J Phys Chem B* 118: 12805 – 12817

Scalettar BA, Abney JR, Hackenbrock CR (1991) Dynamics, structure and function are coupled in the mitochondrial matrix. *Proc Natl Acad Sci USA* 88: 8057 – 8061

Schavemaker PE, Boersma AJ, Poolman B (2018) How important is protein diffusion in prokaryotes? *Front Mol Biosci* 5: 93

Schmidt CA, Fisher-Wellman KH, Neufer PD (2021) From OCR and ECAR to energy: perspectives on the design and interpretation of bioenergetics studies. *J Biol Chem* 4: 101140

Segawa M, Wolf DM, Hultgren NW, Williams DS, van der Bliek AM, Schackelford DB, Liesa M, Shirihai OS (2020) Quantification of cristae architecture reveals time-dependent characteristics of individual mitochondria. *Life Sci Alliance* 3: e201900620

Shpilka T, Haynes CM (2018) The mitochondrial UPR: mechanisms, physiological functions and implications in ageing. *Nat Rev Mol Cell Biol* 19: 109 – 120

Smeitink JAM, van den Heuvel L, DiMauro S (2001) The genetics and pathology of oxidative phosphorylation. *Nat Rev Genet* 2: 342 – 352

Sprague BL, McNally JG (2005) FRAP analysis of binding: proper and fitting. *Trends Cell Biol* 15: 84 – 91

Sprenger HG, Langer T (2019) The good and the bad of mitochondrial breakups. *Trends Cell Biol* 29: 888 – 900

Steinmark IE, James AL, Chung PH, Morton PE, Parsons M, Dreiss CA, Lorentz CD, Yahioglu G, Suhling K (2019) Targeted fluorescence lifetime probes reveal responsive organelle viscosity and membrane fluidity. *PLoS ONE* 14: e0211165

Stephan T, Roesch A, Riedel D, Jakobs S (2019) Live-cell STED nanoscopy of mitochondrial cristae. *Sci Rep* 9: 12419

Sutherland W (1905) A dynamical theory of diffusion for non-electrolytes and the molecular mass of albumin. *Philos Mag* 9: 781 – 785

Tyn MT, Gusek TD (1990) Prediction of diffusion coefficients of proteins. *Biotechnol Bioeng* 35: 327 – 338

Vámosi G, Mücke N, Müller G, Krieger JW, Curth U, Langowski J, Tóth K (2014) EGFP oligomers as natural fluorescence and hydrodynamic standards. *Sci Rep* 6: 33022

Van den Bogaart G, Hermans N, Krasnikov V, Poolman B (2007) Protein mobility and diffusive barriers in *Escherichia coli*: consequences of osmotic stress. *Mol Microbiol* 64: 858 – 871

Van Tartwijk FW, Kaminski CF (2022) Protein condensation, cellular organization and spatiotemporal regulation of cytoplasmic properties. *Adv Biol* 6: e2101328

Verkman AS (2002) Solute and macromolecular diffusion in cellular aqueous compartments. *Trends Biochem Sci* 27: 27 – 33

Vögtle FN, Burkhart JM, Gonczarowska-Jorge H, Kücükköse C, Taskin AA, Kopczynski D, Ahrends R, Mossmann D, Sickmann A, Zahedi RP *et al* (2017) Landscape of submitochondrial protein distribution. *Nat Commun* 8: 290

Von Smoluchowski M (1906) Zur kinetischen theorie der Brownschen Molekularbewegung und der suspensionen. *Ann Phys* 326: 756 – 780

Vorontsova I, Vallmitjana A, Torrado B, Schilling TF, Hall JE, Gratton E, Malacrida L (2022) In vivo macromolecular crowding is differentially modulated by aquaporin 0 in zebrafish lens: insights from a nanoenvironment sensor and spectral imaging. *Sci Adv* 8: eabj4833

Vyšniauskas A, Qurashi M, Gallop N, Balaz M, Anderson HL, Kuimova MK (2015) Unravelling the effects of temperature on viscosity-sensitive fluorescence molecular rotors. *Chem Sci* 6: 5773 – 5778

Wang C, Taki M, Sato Y, Tamura Y, Yaginuma H, Okada Y, Yamaguchi S (2019) A photostable fluorescent marker for the superresolution live imaging of the dynamic structure of the mitochondrial cristae. *Proc Natl Acad Sci USA* 116: 15817 – 15822

Weilandt DR, Hatzimanikatis V (2019) Particle-based simulation reveals macromolecular crowding effects on the Michaelis-Menten mechanism. *Biophys J* 117: 355 – 368

Weiss M (2014) Crowding, diffusion, and biochemical reactions. Chapter 11 in: new models of the cell nucleus: crowding, entropic forces, phase separation, and fractals. *Int Rev Cell Mol Biol* 307: 383 – 417

Weissert V, Rieger B, Morris S, Arroum T, Psathaki OE, Zobel T, Perkins G, Busch KB (2021) Inhibition of the mitochondrial ATPase function by IF1 changes the spatiotemporal organisation of ATP synthase. *Biochim Biophys Acta Bioenerg* 1862: 148322

© 2023 The Authors

14602075, 2023, 7, Downloaded from https://www.embopress.org/doi/10.15252/embj.2021108533 by Wageningen University and Research Bibliotheek, Wiley Online Library on [11/08/2023]. See the Terms and Conditions (https://onlinelibrary.wiley.com/terms-and-conditions) on Wiley Online Library for rules of use; OA articles are governed by the applicable Creative Commons License

Wilcox XE, Ariola A, Jackson JR, Slade KM (2020) Overlap concentration and the effect of macromolecular crowding on citrate synthase activity. *Biochemistry* 59: 1737 – 1746

Wilkens V, Kohl W, Busch K (2013) Restricted diffusion of OXPHOS complexes in dynamic mitochondrial delays their exchange between cristae and engenders a transitory mosaic distribution. *J Cell Sci* 126: 103 – 116

Willems PHGM, Rossignol R, Dieteren CEJ, Murphy MP, Koopman WJH (2015) Redox homeostasis and mitochondrial dynamics. *Cell Metab* 22: 207 – 218

Wolf DM, Segawa M, Kondadi AK, Anand R, Bailey ST, Reichert AS, van der Bliek AM, Schackelford DB, Liesa M, Shirihai O (2019) Individual cristae within the same mitochondrion display different membrane potentials and are functionally independent. *EMBO J* 38: e101056

Xiao H, Li P, Tang B (2021) Small molecular fluorescent probes for imaging of viscosity in living biosystems. *Chemistry* 27: 6880 – 6898

Yang Z, He Y, Lee JH, Park N, Suh M, Chae WS, Cao J, Peng X, Jung H, Kang C *et al* (2013) A self-calibrating bipartite viscosity sensor for mitochondria. *J Am Chem Soc* 135: 9181 – 9185

Yin J, Huang L, Wu L, Li J, James TD, Lin W (2021) Small molecule based fluorescent chemosensors for imaging the microenvironment within specific cellular regions. *Chem Soc Rev* 50: 12098 – 12150

Young ME, Carroad PA, Bell RL (1980) Estimation of diffusion coefficients of proteins. *Biotechnol Bioeng* 22: 947 – 955

Yu I, Mori T, Ando T, Harada R, Jung J, Sugita Y, Feig M (2016) Biomolecular interactions modulate macromolecular structure and dynamics in atomistic model of a bacterial cytoplasm. *Elife* 5: e19274

Zhang C, Shao PG, van Kan JA, van der Maarel JRC (2009) Macromolecular crowding induced elongation and compaction of single DNA molecules confined in a nanochannel. *Proc Natl Acad Sci USA* 106: 16651 – 16656

Zhou HX, Rivas G, Minton AP (2008) Macromolecular crowding and confinement: biochemical, biophysical and potential physiological consequences. *Annu Rev Biophys* 37: 375 – 397

License: This is an open access article under the terms of the Creative Commons Attribution-NonCommercial-NoDerivs License, which permits use and distribution in any medium, provided the original work is properly cited, the use is non-commercial and no modifications or adaptations are made.

14602075, 2023, 7, Downloaded from https://www.embopress.org/doi/10.15252/embj.2021108533 by Wageningen University and Research Bibliotheek, Wiley Online Library on [11/08/2023]. See the Terms and Conditions (https://onlinelibrary.wiley.com/terms-and-conditions) on Wiley Online Library for rules of use; OA articles are governed by the applicable Creative Commons License

Expanded View Figures

Figure EV1. Compact and extended structural conformations of AcGFP1 concatemers.

A Dimensions (numerals) of AcGFP1 in Angstrom (Å) based upon GFP crystal structure. R and L indicate the radius and length of the protein, respectively. Geometric data are summarized in Table 1.
B Same as panel (A) but now for $AcGFP1^2$ displaying a minimal structural conformation ("compact").
C Same as panel (A) but now for $AcGFP1^2$ displaying a structural conformation of maximal size ("extended").
D Same as panel (A) but now for $AcGFP1^3$ displaying a compact structure.
E Same as panel (A) but now for $AcGFP1^3$ displaying an extended structure.
F Same as panel (A) but now for $AcGFP1^4$ displaying a compact structure.
G Same as panel (A) but now for $AcGFP1^4$ displaying an extended structure.

© 2023 The Authors

14602075, 2023, 7, Downloaded from https://www.embopress.org/doi/10.15252/embj.2021108533 by Wageningen University and Research Bibliotheek, Wiley Online Library on [11/08/2023]. See the Terms and Conditions (https://onlinelibrary.wiley.com/terms-and-conditions) on Wiley Online Library for rules of use; OA articles are governed by the applicable Creative Commons License

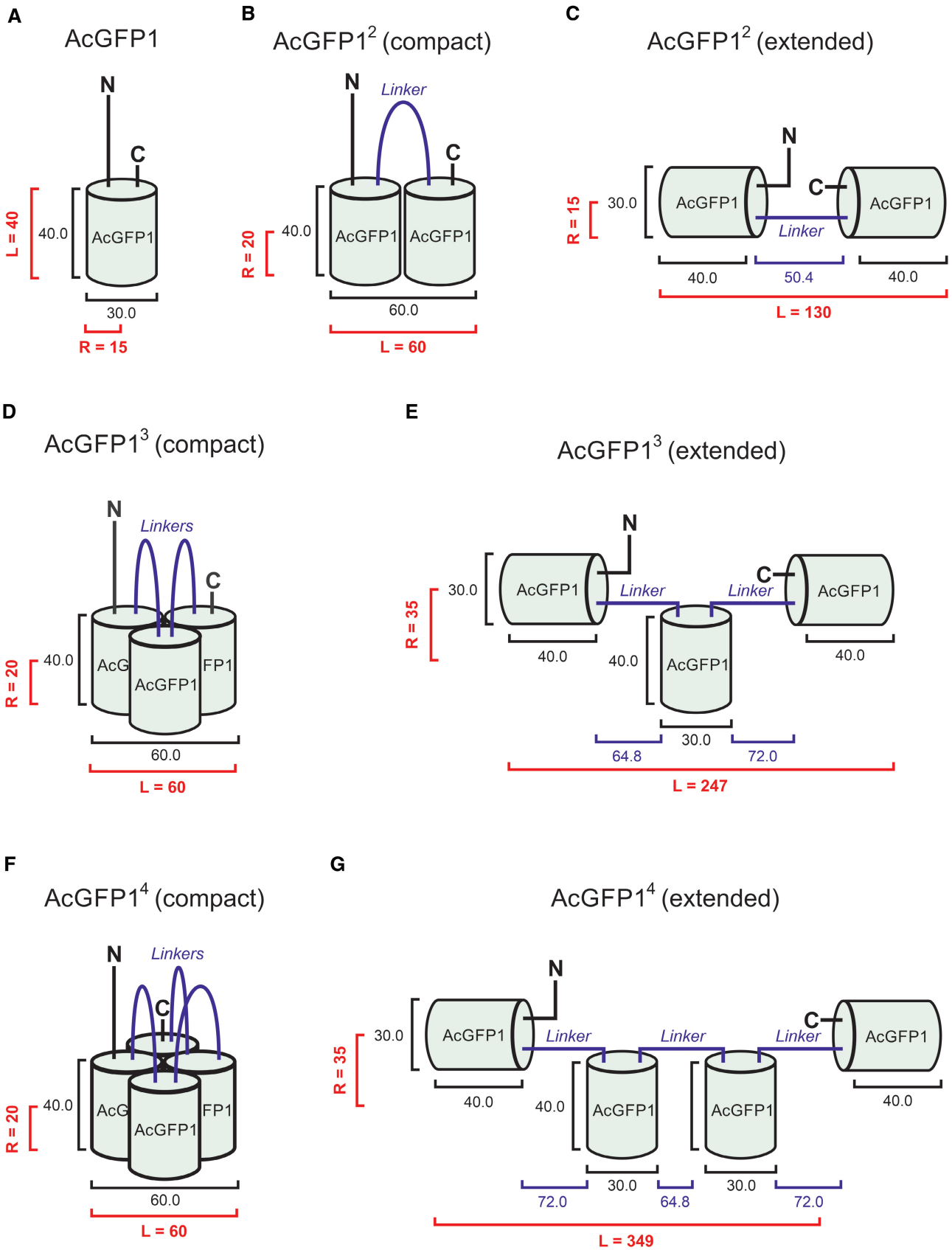

Figure EV1.

© 2023 The Authors

14602075, 2023, 7, Downloaded from https://www.embopress.org/doi/10.15252/embj.2021108533 by Wageningen University and Research Bibliotheek, Wiley Online Library on [11/08/2023]. See the Terms and Conditions (https://onlinelibrary.wiley.com/terms-and-conditions) on Wiley Online Library for rules of use; OA articles are governed by the applicable Creative Commons License

Figure EV2. Functional consequences of chloramphenicol (CAP) treatment in HeLa parental cells.

A Average oxygen consumption rate (OCR) in untreated cells, and cells treated with DOX, CAP, or DOX + CAP (for legend see panel B). Oligomycin (OLI), mitochondrial uncoupler (FCCP), and antimycin A + rotenone (AA/ROT) were added at the indicated time points.

B Same as panel (A) but now for the average extracellular acidification rate (ECAR).

C Statistical analysis of the data in panel (A and B) with respect to the basal OCR, maximal OCR and basal ECAR.

D Effect of CAP on the TMRM fluorescence signal in mitochondria and nucleus. Left panel: Typical example of fluorescence microscopy image of TMRM-stained cells. Fluorescence signals were manually determined in two regions of interest (yellow) defined in a mitochondria-dense ("m") and nucleoplasmic part ("n") of the cell and corrected for background using a close by ROI outside of the cell ("b"). Data panels: numerical values for the mitochondrial fluorescence signal (mito), nuclear fluorescence signal (nucleus) and fluorescence ratio value (mito/nucleus).

E Effect of DOX, CAP or DOX + CAP on the cellular protein levels of LONP1 (specific bands marked by red boxes), mtHSP70, mtHSP60, CLPP and CHOP. β-actin was used as cellular loading control. Arrowheads indicate molecular weight in kDa. Individual panels were contrast-optimized for visualization purposes. Original blots are presented in Appendix Fig S5B.

F Effect of CAP on mitochondrial DNA (mtDNA) levels expressed as number of mtDNA copies per cell and per nanogram (ng) of total DNA.

G Effect of CAP on the cellular levels of key mitochondrial fission and fusion proteins (specific bands are marked by red boxes): DRP1 (Dynamin-related protein 1, OPA1 (Optic atrophy protein 1), MFN2 (Mitofusin 2). β-actin and VDAC1 were used as cellular and mitochondrial loading controls, respectively. Arrowheads indicate molecular weight in kDa. Individual panels were contrast-optimized for visualization purposes. Original blots are presented in Appendix Fig S5A.

Data information: OCR and ECAR data (panels A–C) was obtained in a single ($N = 1$) experiment and the following number (n) of technical replicates: Untreated ($n = 5$), +DOX ($n = 5$), +CAP ($n = 4$), +DOX+CAP ($n = 6$). TMRM data (Panel D) was obtained in $N = 2$ independent experiments for $n = 991$ cells (−CAP) and $n = 668$ cells (+CAP). MtDNA data (panel F) was obtained in $N = 2$ independent experiments in $n = 7$ assays (−CAP) and $n = 6$ assays (+CAP). Each symbol represents an individual well (panel C), cell (panel D) or assay (panel F). In panels (A and B), individual data points reflect mean ± SEM. In panel (C), bars and errors reflect mean ± SEM. In panels (D and F), error bars mark the 95% (upper) and 5% (lower) percentile, the boundary boxes mark the 75% (upper) and 25% (lower) percentile, the square marks the mean value of the data, and the horizontal line within the box indicates the median value of the data. Significant differences, obtained using an independent Student's t-test, are indicated by $*P < 0.05$, $**P < 0.01$, $***P < 0.001$ between the marked conditions (a–c) in panel (C) and between the −CAP and +CAP condition (panel D and F). Not significant is marked by n.s. The exact P-values for panel (C) (basal OCR) were: Untreated (a) vs. +DOX (b): $P = 0.0126$; Untreated (a) vs. +CAP (c): $P = 1.554{\cdot}10^{-6}$; Untreated (a) vs. +DOX+CAP: $P = 4.082{\cdot}10^{-8}$; +DOX (b) vs. +CAP (c): $P = 2.671{\cdot}10^{-7}$; +DOX (b) vs. +DOX + CAP: $P = 3.806{\cdot}10^{-9}$. The exact P-values for panel (C) (maximal OCR) were: Untreated (a) vs. +DOX (b): $P = 6.509{\cdot}10^{-4}$; Untreated (a) vs. +CAP (c): $P = 2.019{\cdot}10^{-7}$; Untreated (a) vs. +DOX+CAP: $P = 4.900{\cdot}10^{-9}$; +DOX (b) vs. +CAP (c): $P = 4.558{\cdot}10^{-8}$; +DOX (b) vs. +DOX + CAP: $P = 5.713{\cdot}10^{-10}$. The exact P-values for panel (C) (basal ECAR) were: Untreated (a) vs. +DOX (b): $P = 0.0023$; Untreated (a) vs. +CAP (c): $P = 4.571{\cdot}10^{-8}$; Untreated (a) vs. +DOX+CAP: $P = 7.784{\cdot}10^{-10}$; +DOX (b) vs. +CAP (c): $P = 2.412{\cdot}10^{-8}$; +DOX (b) vs. +DOX+CAP: $P = 7.039{\cdot}10^{-10}$. The exact P-value for panel (C) (mito) was: $P = 7.145{\cdot}10^{-6}$. The exact P-value for panel (C) (nucleus) was: $P = 0.0237$. The exact P-value for panel (C) (mito/nucleus) was: $P = 5.702{\cdot}10^{-5}$. The exact P-value for panel (F) (per cell) was: $P = 0.556$. The exact P-value for panel (F) (per ng total DNA) was: $P = 0.139$.

© 2023 The Authors

14602075, 2023, 7, Downloaded from https://www.embopress.org/doi/10.15252/embj.2021108533 by Wageningen University and Research Bibliotheek, Wiley Online Library on [11/08/2023]. See the Terms and Conditions (https://onlinelibrary.wiley.com/terms-and-conditions) on Wiley Online Library for rules of use; OA articles are governed by the applicable Creative Commons License

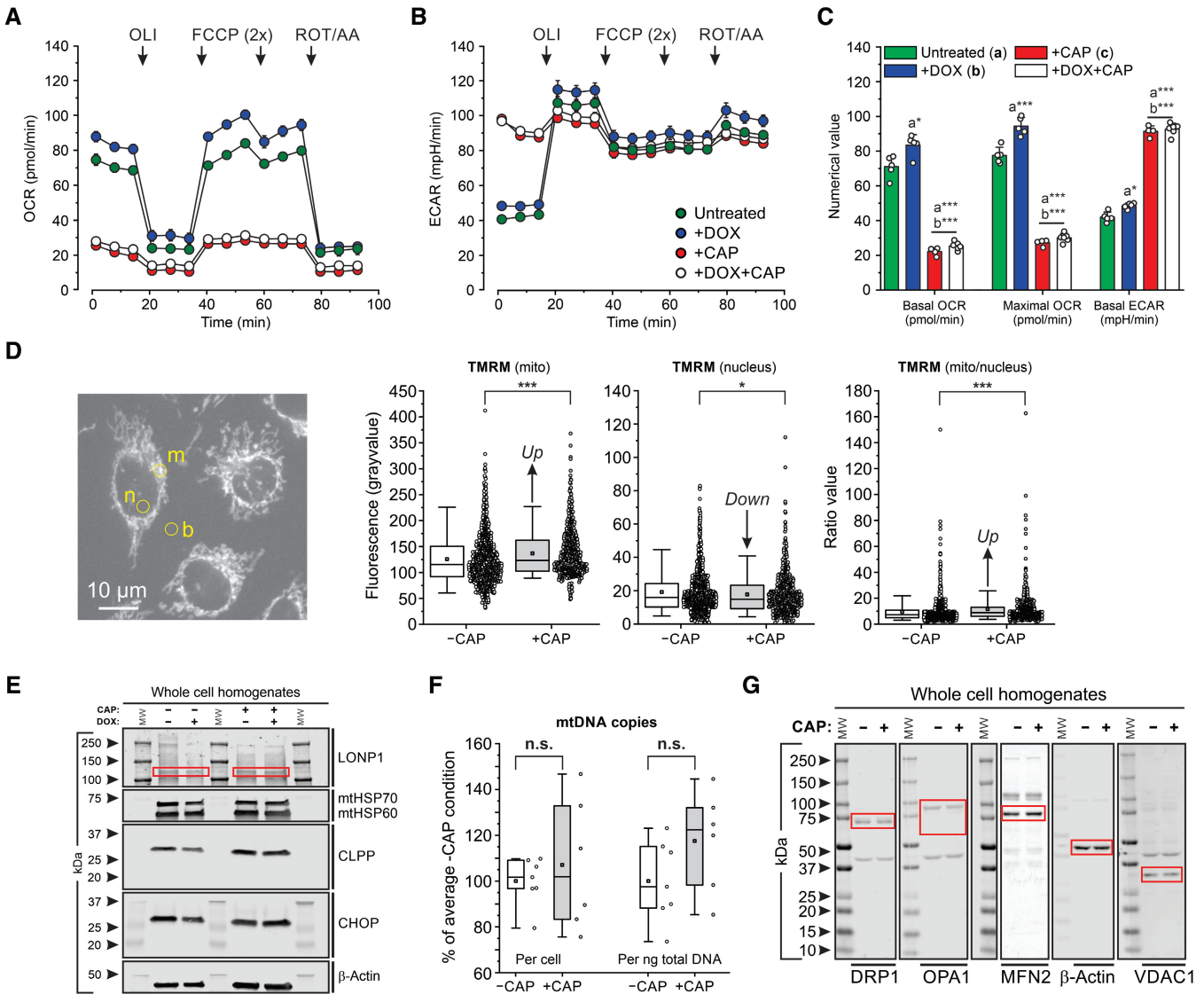

Figure EV2.

Figure EV3. Chloramphenicol (CAP) and doxycycline (DOX) do not increase protein markers typically associated with induction of the mitochondrial unfolded protein response (UPR^{mt}) in parental and FP-expressing cells.

A Western blot analysis (SDS–PAGE) of whole-cell homogenates was used to assess the levels of the following proteins: LONP1, mtHSP70, mtHSP60, CLPP, and CHOP. β-actin was used as a cellular loading control. MW indicates molecular weight in kDa. Effect of the expression inducer DOX (1 µg/ml, 24 h) and CAP (40 µg/ml, 72 h), alone and in combination (i.e., 48-h CAP treatment followed by 24 h CAP + DOX treatment), on protein levels in FP-expressing HeLa cell lines (AcGFP1, $AcGFP1^2$, $AcGFP1^3$, and $AcGFP1^4$). Individual panels were contrast-optimized for visualization purposes. Original blots are presented in Appendix Fig S4.

B Quantitative analysis of protein levels in panel A and in HeLa parental cells (the open symbols reflect data for the parental cells in Appendix Fig S5B). All signals were normalized on β-actin and expressed as % of the condition without DOX and CAP ("−DOX−CAP"). Effects previously associated with UPR^{mt} induction are marked: "Up" indicates proteins that are expected to be upregulated upon UPR^{mt} induction, "Down "indicates proteins that are expected to be downregulated upon UPR^{mt} induction.

Data information: The effects of DOX, CAP, and DOX + CAP were compared with the "−DOX−CAP" (untreated) condition (i.e., with the dotted line marked "&") by testing whether the mean value for each protein (i.e., within each gray box in panel B) differed from 100% (using a one-sample Student's *t*-test). Comparisons with the DOX only condition (+DOX; marked "a") and CAP-only condition (+CAP; marked "b") were performed using an independent two-population *t*-test (i.e., between each gray box for each protein). Not significant is marked by n.s.

© 2023 The Authors

14602075, 2023, 7, Downloaded from https://www.embopress.org/doi/10.15252/embj.2021108533 by Wageningen University and Research Bibliotheek, Wiley Online Library on [11/08/2023]. See the Terms and Conditions (https://onlinelibrary.wiley.com/terms-and-conditions) on Wiley Online Library for rules of use; OA articles are governed by the applicable Creative Commons License

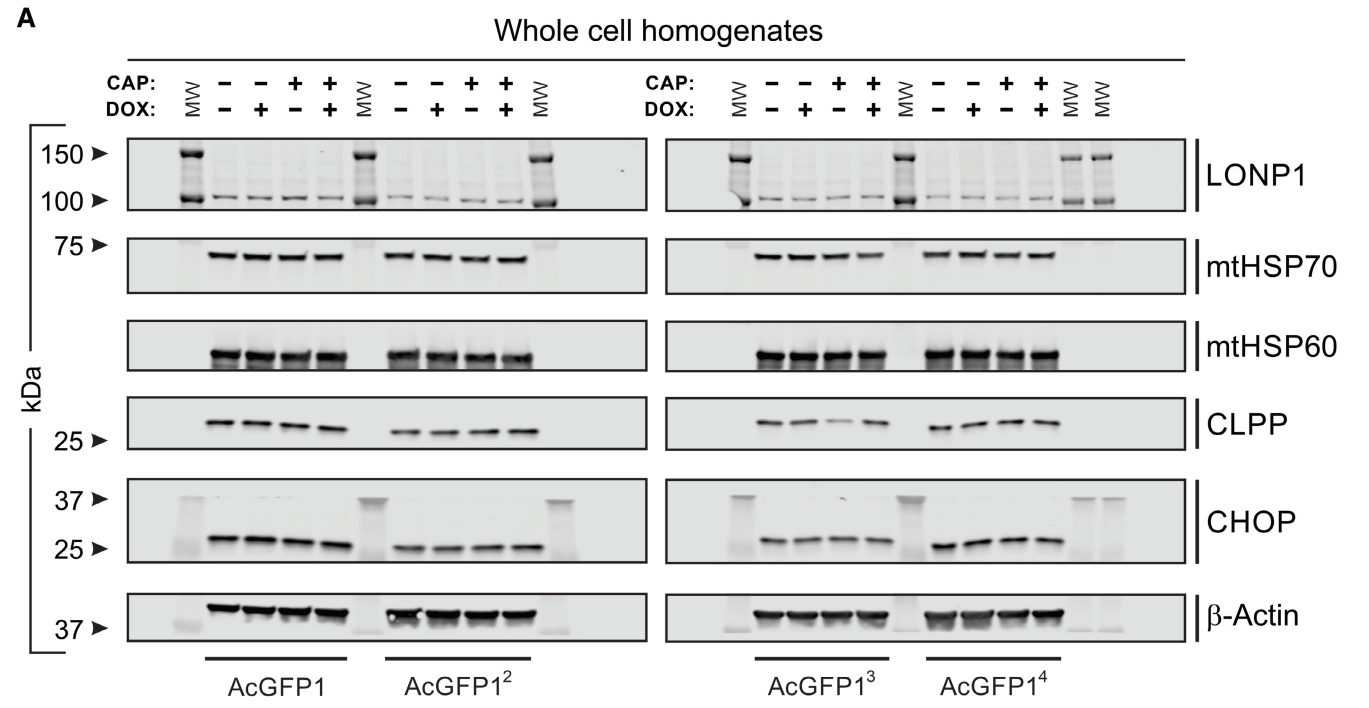

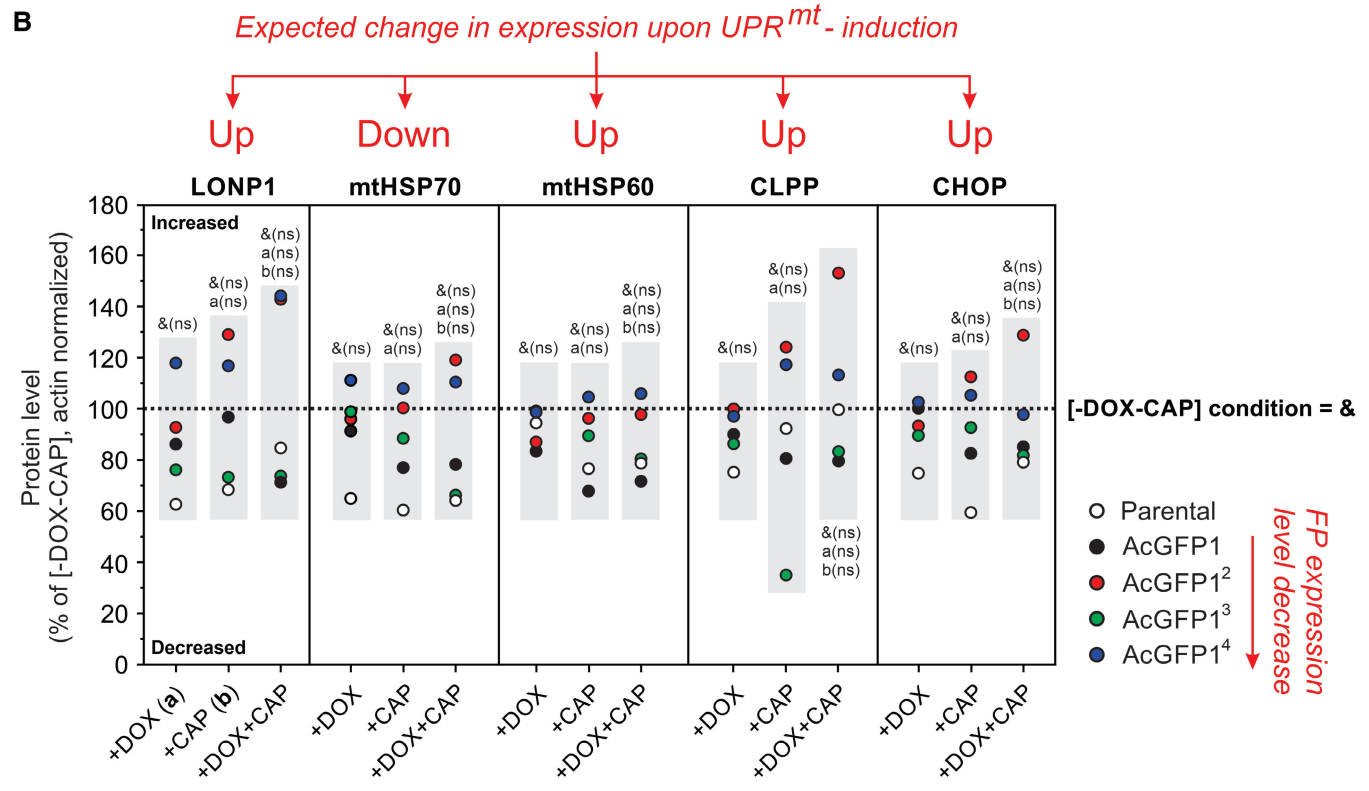

Figure EV3.

© 2023 The Authors

14602075, 2023, 7, Downloaded from https://www.embopress.org/doi/10.15252/embj.2021108533 by Wageningen University and Research Bibliotheek, Wiley Online Library on [11/08/2023]. See the Terms and Conditions (https://onlinelibrary.wiley.com/terms-and-conditions) on Wiley Online Library for rules of use; OA articles are governed by the applicable Creative Commons License

APPENDIX - TABLE OF CONTENTS

1. Appendix Supplementary Methods [PAGE 2-9]

- Generation of HeLa cell lines – **PAGE 2**
- Mitochondrial colocalization analysis – **PAGE 2-3**
- Flowcytometry – **PAGE 3**
- Fluorescence recovery after photobleaching experiments – **PAGE 3-4**
- SDS-PAGE, in-gel fluorescence analysis and Western blotting of mitochondrial fractions – **PAGE 4**
- SDS-PAGE and Western blotting of whole-cell lysates – **PAGE 4**
- Oxygen consumption (OCR) and extracellular acidification rate (ECAR) measurements – **PAGE 4-5**
- TMRM measurements – **PAGE 5**
- Quantification of mitochondrial DNA content – **PAGE 5**
- Electron microscopy – **PAGE 5-6**
- Simulation modelling of mitochondrial FRAP experiments – **PAGE 6-7**
- Calculation of solvent viscosity (ηsolvent) from $D_{solvent}$ using the He-Niemeyer equation – **PAGE 7-8**
- Calculation of solvent viscosity (ηsolvent) from $D_{solvent}$ using the Young equation – **PAGE 8**
- Calculation of solvent viscosity (ηsolvent) from $D_{solvent}$ using the Tyn-Gusek equation – **PAGE 8**
- Calculation of solvent viscosity (ηsolvent) from $D_{solvent}$ using the Stokes-Einstein equation – **PAGE 8-9**

2. Appendix Supplementary Results [PAGE 9-10]

- Chloramphenicol but not doxycycline induces a glycolytic switch– **PAGE 9**
- Chloramphenicol increases mitochondrial TMRM fluorescence – **PAGE 9**
- Chloramphenicol and doxycycline do not increase the protein levels of mitochondrial unfolded protein response markers – **PAGE 9-10**
- Chloramphenicol does not alter mitochondrial DNA copy number and the level of key mitochondrial fission and fusion proteins – **PAGE 10**
- Predicted level of macromolecules and volume exclusion in the absence and presence of CAP – **PAGE 10**

3. Appendix Supplementary Figures [PAGE 11-15]

- Appendix Figure S1: Original in-gel fluorescence scans and Western blots. – **PAGE 11**
- Appendix Figure S2: Analysis of mitochondrial fluorescence recovery after photobleaching (FRAP) experiments and quantification of mitochondrial radius (R_{mito}) and length (L_{mito}). – **PAGE 12**
- Appendix Figure S3: Synthetic FRAP data generated by the BD model. – **PAGE 13**
- Appendix Figure S4: Original blots for analysis of UPR^{mt} proteins in FP-expressing cells. – **PAGE 14**
- Appendix Figure S5: Original blots for analysis of fission/fusion and UPR^{mt} proteins in HeLa parental cells. – **PAGE 15**

4. Appendix Supplementary Tables [PAGE 16-24]

- Appendix Table S1: Sequences and MW of the AcGFP1 concatemers – **PAGE 16**
- Appendix Table S2: Experimental $D_{solvent}$ values in aqueous solution and in the cell – **PAGE 17-22**
- Appendix Table S3: Interpretation of the data sets in Appendix Table S2 – **PAGE 23**

5. Appendix Supplementary References [PAGE 24-27]

14602075, 2023, 7, Downloaded from https://www.embopress.org/doi/10.15252/embj.2021108533 by Wageningen University and Research Bibliotheek, Wiley Online Library on [11/08/2023]. See the Terms and Conditions (https://onlinelibrary.wiley.com/terms-and-conditions) on Wiley Online Library for rules of use; OA articles are governed by the applicable Creative Commons License

1. Appendix Supplementary Materials and methods

Generation of HeLa cell lines - AcGFP1 is an inert monomeric fluorescent protein derived from *Aequorea coerulescens*, the intense illumination of which is not phototoxic (**Bulina *et al.*, 2006; Bell *et al.*, 2007; Dieteren *et al.*, 2008; Dieteren *et al.*, 2011**). HeLa cell lines stably expressing AcGFP1 or AcGFP^2 were generated using the same vector constructs as described previously for HEK293 cells (**Dieteren *et al.*, 2008**). To this end, cDNA of the cox8 leader sequence (first 210 base pairs of sequence NM_00004074) was generated by Gateway-adapted PCR procedures according to the manufacturer's instructions (**Invitrogen Thermo Fisher, Carlsbad, CA, USA**). A cox8-entry clone was generated from the resulting PCR product by recombination with pDONR201 (**Invitrogen**) using Gateway Clonase II Enzyme Mix (**Invitrogen**). An AcGFP1 destination vector was generated by subcloning the BamHI/NotI restriction fragment of pAcGFP1-N1 (**Clontech, Westburg, Leusden, The Netherlands**) in-frame behind Gateway Reading Frame Cassette B (**Invitrogen**) in pcDNA5/FRT/TO (**Invitrogen**). To obtain an inducible vector containing mitochondrial matrix-targeted AcGFP1, the entry vector was recombined with the AcGFP1 destination vector by using Gateway LR Clonase II Enzyme Mix (**Invitrogen**). In the same manner, a tandem mitochondrial AcGFP1 expression vector (AcGFP1^2) was created by first generating an entry vector containing the cox8 leader sequence linked to the N-terminus of AcGFP1 (without the stop codon) and then recombining this entry clone with the AcGFP1-destination vector. To create a cox8-cox8-AcGFP1 entry clone, the cox8- sequence of the cox8-AcGFP1 entry clone was replaced by a cox8-cox8 sequence amplified from a "Pericam" vector (**Palmer *et al.*, 2004**) using the primers: Fwd_5'aaatttaaaGGGCCCCAAATAATGATTTTATTTTGA3' and Rev_5'ataataataACCGGTTTGAGATCTCCCTCCGGCGGCAA3' using the ApaI and AgeI restriction sites for ligation. Accuracy of the vector was confirmed by sequencing. To create a triple AcGFP1 expression vector (AcGFP1^3), an AcGFP1^3 destination vector was generated by consecutive cloning steps. First, an AcGFP1 fragment was generated by PCR using the primers Fwd_5'tatataACCGGTATCGATaaaattGCTAGCcatggtgagcaagggcgccgag3' and Rev_5'tatataaccggtA TGCATaacaatt gGATATCcttgtacagctcatccatgcc3' on pAcGFP-N1 (**Clontech**) as a template, and ligated into the AgeI site of the AcGFP1 destination vector, delivering an AcGFP1^2 destination vector. Subsequently, the cox8-cox8-AcGFP1 entry clone was recombined with this AcGFP1^2 destination vector using Gateway LR Clonase II Enzyme mix (**Invitrogen**), generating a cox8-cox8-AcGFP1^3 expression vector. Unfortunately, this expression vector displayed suboptimal mitochondrial expression (data not shown). As an alternative strategy, an AcGFP1 fragment was generated by PCR with primers Fwd_5'ttt tttGATATCcCGCCGCACCCAGCTTTCTTGT3' and Rev_5'ttttttATGCATgTCGATACCG GTGGATCATCAAC3' with cox8-cox8-AcGFP1^3 expression vector as template, and ligated into the EcoRV and NsiI sites of the AcGFP1^2 destination vector. This AcGFP1^3 destination vector was recombined with the cox8-entry vector and the cox8-cox8-AcGFP1 entry vector using Gateway LR Clonase II Enzyme mix (**Invitrogen**), generating the AcGFP1^3 and AcGFP1^4 expression vectors used further in this study, respectively. HeLa T-REx Flp-in cells were stably transfected using Superfect Transfection Reagent (**Qiagen, Venlo, The Netherlands**) according to the manufacturer's protocol and cultured for selection in the presence of 200 µg/ml hygromycin (#10687010; **Invitrogen**) in Dulbecco's modified Eagle's medium (DMEM; #31966; **Gibco Thermo-Fisher, MD, Gaithersburg, USA**) supplemented with 10% (v/v) fetal bovine serum (#10270; **Gibco**), 1% (v/v) penicillin/streptomycin (#15140; **Gibco**) and 4 µg/ml blasticin (# R21001; **Gibco**). The DMEM also contained 25 mM D-glucose, 3.97 mM L-Alanyl-L-Glutamine (GlutaMAX) and 1 mM pyruvate. Parental cells were cultured in the presence of 50 µg/ml zeocin (#R25001; **Invitrogen**) instead of hygromycin. All cell lines were tested for mycoplasma contamination and found negative.

Mitochondrial colocalization analysis - HeLa cells were cultured on glass-bottomed WillCo® dishes (**WillCo Wells B.V., Amsterdam, The Netherlands**) and induced with doxycycline (1 µg/ml; 24 h). Next, the cells were incubated with 1 µM MitoTracker Red CM-H2XROS (#M7513; **Invitrogen)** for 30 min in the dark (37º, 95% air, 5% CO_2). Then, the cells were washed with a colourless HEPES-Tris (HT) solution

14602075, 2023, 7, Downloaded from https://www.embopress.org/doi/10.15252/embj.2021108533 by Wageningen University and Research Bibliotheek, Wiley Online Library on [11/08/2023]. See the Terms and Conditions (https://onlinelibrary.wiley.com/terms-and-conditions) on Wiley Online Library for rules of use; OA articles are governed by the applicable Creative Commons License

(132 mM NaCl, 4.2 mM KCl, 1 mM $CaCl_2$, 1 mM $MgCl_2$, 5.5 mM D-glucose and 10 mM HEPES, pH 7.4) and fluorescence microscopy images were acquired using a ZEISS LSM510 Meta confocal microscope (**Carl Zeiss B.V., Sliedrecht, The Netherlands**) using a Plan-Apochromat 63x/1.40 Oil DIC objective (**Carl Zeiss**), a zoom factor of 2 and an optical slice thickness of < 1 µm. AcGFP1 and MitoTracker Red fluorescence signals were collected following excitation at 488 nm (Argon laser; set at 2% transmission) and 543 nm (Helium/Neon laser; 43% transmission), respectively. AcGFP1 fluorescence was detected using a 488nm dichroic mirror and a 500-530 nm band pass filter. MitoTracker Red fluorescence was detected using a 543 nm dichroic mirror and a 560 nm long pass filter.

Flowcytometry - HeLa T-REx Flp-in cells were cultured in 24-well plates (#662160; **Cellstar, Greiner Bio-One International GmbH, Alphen aan de Rijn, The Netherlands**). Using half of the wells, expression of AcGFP1 concatemers was induced with doxycycline (1 µg/ml; 24 h). Prior to flowcytometry measurements cells were trypsinized, washed with PBS and resuspended in colourless DMEM (#A14430-01; **Gibco**). Cells were analyzed using a FACSCalibur flow cytometer (**BD Biosciences, Alschwil, Switserland**) and data was exported to Excel using FloJo software.

Fluorescence recovery after photobleaching experiments - For FRAP analysis (*e.g.* **Lorén *et al.*, 2015**), cells were seeded in glass-bottomed WillCo® dishes (**WillCo Wells B.V., Amsterdam, The Netherlands)** and grown to ~70% confluence. As a reference, the cox8-AcGFP1-expressing cell line ("AcGFP1") was included on each day of experiments. Measurements were performed using a ZEISS LSM510 Meta confocal microscope (**Carl Zeiss**) at 20 ºC (293K) to minimize mitochondrial movement (**Koopman *et al.*, 2006; Dieteren *et al.*, 2008; Dieteren *et al.*, 2011**). Images were acquired at 10 Hz using a Plan-Apochromat 63x oil immersion objective (NA=1.4; **Carl Zeiss**). Pre- and post-bleach imaging was performed using 488 nm excitation light (Argon laser; set at 3% transmission), a 488 nm dichroic mirror and a 505 nm longpass filter. First the pre-bleach fluorescence level was recorded, after which AcGFP1 photobleaching was performed (Argon laser; set at 100% transmission for 100 ms) in a FRAP region of 10x10 pixels (measuring 1.4x1.4 µm). Routinely, a zoom factor of 4 was used and pinhole settings were chosen to achieve an optical thickness of < 2 µm. Only single mitochondria that were fully located within the focal plane were used for analysis (confirmed by an axial scan through the filament). Only mitochondria in which FRAP was paralleled by fluorescence loss in photobleaching (FLIP) in a part distal to the FRAP region were considered to possess a continuous mitochondrial matrix and included in the analysis (**Appendix Fig. S2A-B-C**). In our experiments the size of the FRAP region is relatively large when compared to the size of the mitochondrion. Therefore, the experimental FRAP curves (F(t)) were corrected as described previously (**Goodwin & Kenworthy, 2005; Dieteren *et al.*, 2011**) using:

$$F(t) = 100 \times \frac{(F(t)_{\text{FRAPregion}} - F(t)_{\text{background}})}{(F(t)_{\text{totalmito}} - F(t)_{\text{background}})} \times \frac{(F_{\text{i,totalmito}} - F_{\text{background}})}{(F_{\text{i,FRAPregion}} - F_{\text{background}})} \qquad \textbf{[Equation-I]}$$

Here the fluorescence intensity in the bleached mitochondrial region ($F(t)_{FRAPregion}$) and for the total mitochondrion ($F(t)_{totalmito}$), is background-corrected ($F(t)_{background}$) at each time point. Next, the corrected fluorescence signal in the bleached region is divided by the corrected intensity of the total mitochondrion to correct for the loss of mitochondrial fluorescence during the bleach. The corrected data are normalized to the background-corrected pre-bleach intensity ($F_{i,FRAP\ region}$ and $F_{i,total\ mito}$) and multiplied by 100 to yield a percentage of pre-bleach fluorescence (**Appendix Fig. S2**). Applying **[Equation-I]** also corrects for photobleaching induced by normal image acquisition. Mean fluorescence recovery curves were calculated by averaging multiple FRAP recordings from single mitochondria. This averaging improved the signal-to-noise ratio, which facilitated convergence of the Levenberg-Marquardt algorithm (**Levenberg, 1944**; **Marquardt, 1963**) used for fitting of the average FRAP curves with a mono-exponential equation (**Dieteren *et al.*, 2011**):

14602075, 2023, 7, Downloaded from https://www.embopress.org/doi/10.15252/embj.2021108533 by Wageningen University and Research Bibliotheek, Wiley Online Library on [11/08/2023]. See the Terms and Conditions (https://onlinelibrary.wiley.com/terms-and-conditions) on Wiley Online Library for rules of use; OA articles are governed by the applicable Creative Commons License

$$F(t) = y_0 + A_{mono}\left(1 - e^{-\frac{t}{T_{mono}}}\right) \quad \textbf{[Equation-II]}$$

With T_{mono} representing the FRAP time constant. The mobile fraction (F_m) was calculated from the average FRAP curves using:

$$F_m = \frac{F_\infty - F_0}{F_i - F_0} \quad \textbf{[Equation-III]}$$

With $F_\infty = y_0 + A_{mono}$ being the fluorescence intensity at $t = t_\infty$. F_0 equals the starting fluorescence level directly after the bleach pulse (as % of the pre-bleach value) and the pre-bleach fluorescence signal (F_i) is set at 100% (due to application of **[Equation I]**).

SDS-PAGE, in-gel fluorescence analysis and Western blotting of mitochondrial fractions - Cells were harvested by trypsinization, washed with cold PBS, centrifuged (5 min, 1000 g, 4˚C) and resuspended in 250 µL MSE buffer (225 mM mannitol, 75 mM D-sucrose and 1 mM Na-EDTA, pH 7.4) supplemented with 1x protease inhibitor cocktail (#05892791001; **Roche Diagnostics Merck**). Cells were exposed to three cycles of cold (liquid nitrogen) and heat shock (37˚C) and homogenized with a micro pestle. Cell debris was pelleted by centrifugation (15 min, 600 g, 4˚C). The supernatant was centrifuged at high speed in order to pellet mitochondria (15 min, 10,000 g, 4˚C). The mitochondrial pellet was dissolved in 40 µL PBS containing 2% (w/v) β-lauryl maltoside and incubated on ice for 10 minutes. Protein concentrations were determined using Protein Assay Dye Reagent Concentrate (#500-0006; **Bio-Rad Laboratories, Hercules, CA, USA**). Spectrophotometric absorbance was measured at 595 nm in a Benchmark Plus plate reader (**Bio-Rad**). Mitochondrial fractions were run on a 4-15% SDS-PAGE gel. First, the gel (40 µg protein per lane) was used for "in-gel" fluorescence analysis of AcGFP1 using a ChemiDoc MP imaging system (**Bio-Rad**). Next, the same gel was used for Western blotting and immunodetection using a rabbit polyclonal antibody against EGFP (kindly provided by F.J. van Kuppeveld, Dept. of Medical Microbiology, Radboudumc, The Netherlands) and a mouse monoclonal antibody against VDAC1 (#MABN504, 1:1000; **Merck**). Anti-rabbit IRDye800 and anti-mouse IRDye680 (**Li-cor Biosciences, Lincoln, NE, USA**) antibodies were used as secondary antibodies. Blots were scanned using an Odyssey CLx scanner (**Li-cor**).

SDS-PAGE and Western blotting of whole-cell lysates - Cells were harvested as described in the previous section. Cell pellets were resuspended in RIPA buffer (50 mM Tris-HCl (pH 7.4), 50 mM NaCl, 1% (v/v) Triton X-100, 5 mM Na_2EDTA, 10 mM $Na_4P_2O_7 \cdot 10H_2O$, 50 mM NaF, 1x Protease Inhibitor Cocktail (#05892791001; Roche), 1 x PhosStop (#04906845001; Roche) and 100 µg/mL DNase I (#79254; Qiagen)) and incubated on ice for 30 min and vortexed every 5 min. Debris was pelleted by centrifugation (10 min, 13.000 rpm, 4°C) and the supernatant was saved to serve as whole cell lysate. Protein concentrations were determined as described in the previous section. Whole-cell lysates (20-25 µg per lane) were run on a 4-15% SDS-PAGE gel and used for Western blotting and immunodetection using the following antibodies: Rabbit-anti-mtHSP60 (#NBP2-67517; **Novus Biologicals, Centennial, CO, USA**), Mouse-anti-mtHSP70/GRP75/HSPA9B/Mortalin (#NBP1-47801; **Novus**), Mouse-anti-LONP1 (#66043-1-Ig; **Proteintech Europe, Manchester, United Kingdom**), Mouse-anti-CLPP (#WH0008192M1; **Merck/Sigma-Aldrich Chemie N.V., Zwijndrecht, The Netherlands**), Rabbit-anti-CHOP/GADD153 (#NBP2-66856; **Novus**), Mouse-anti-OPA1 (#H00004976-M01; **Abnova, Taipei, Taiwan**), Mouse-anti-DRP1 (DLP1; #611112; **BD Transduction Lab**), Rabbit-anti-MFN2 (#m6444; **Sigma-Aldrich**), Mouse-anti-Porin (Porin/VDAC1; #MABN504; 35-kDa; **Merck Millipore**) and Mouse-anti-beta-actin (#A5441; **Sigma-Aldrich**). Blots were scanned using an Odyssey CLx scanner (**Li-cor**).

Oxygen consumption rate (OCR) and extracellular acidification rate (ECAR) measurements - On the day of measurement, a Cell Culture Microplate (#101085-004; **Agilent, Santa Clara, CA, USA**) was coated with Cell-Tak® (#734-1081; **BD Biosciences, San Jose, CA, USA**; 22.4 µg/ml in 0.1 M $NaHCO_3$) at 37˚C (non CO_2-corrected atmosphere) for at least 1 h. Next, cells were seeded at a density of 30,000

14602075, 2023, 7, Downloaded from https://www.embopress.org/doi/10.15252/embj.2021108533 by Wageningen University and Research Bibliotheek, Wiley Online Library on [11/08/2023]. See the Terms and Conditions (https://onlinelibrary.wiley.com/terms-and-conditions) on Wiley Online Library for rules of use; OA articles are governed by the applicable Creative Commons License

cells/well (6 replicates for each condition) in non pH-buffered Seahorse medium (DMEM containing 2 mM glutamine, 11 mM D-(+)glucose and 1 mM pyruvate; pH set to 7.4 with NaOH). Next, the plates were placed in an incubator without CO_2 correction for 1 h at 37°C. Using a Seahorse® XFe96 Analyzer (**Agilent**), the oxygen consumption rate (OCR) and extracellular acidification rate (ECAR) were measured for each well. Basal OCR/ECAR was quantified using three cycles (each consisting of 3 min of mixing followed by 3 min of recording). A similar approach was used to subsequently quantify the effects of 1 µM oligomycin (OLI; #75351; **Sigma**), two additions (2 µM and 1 µM) of carbonyl cyanide-p-trifluoromethoxyphenylhydrazone (FCCP; #C2920; **Sigma**) and the combined addition of 1.25 µM rotenone (ROT; #R887; **Sigma**) and 2.5 µM antimycin A (AA; #A8674; **Sigma**). Individual wells with zero OCR values and the corresponding ECAR data points were excluded from the analysis.

TMRM measurements **-** Cells were seeded at a density of 10,000/dish (FluoroDishes®; #FD35-100; **World Precision Instruments Ltd., Friedberg Germany**). Following 24 h of culturing, the DMEM medium was replaced by DMEM containing 40 µg/ml chloramphenicol (CAP; #C0378; **Sigma**). Prior to microscopy analysis, cells were incubated (in the dark; humidified atmosphere; 95% air; 5% CO_2, 25 min, 37°C) with 15 nM tetramethylrhodamine methyl ester (TMRM; #T668; **Life Technologies Thermo Fisher Scientific, Waltham, MA, USA**) diluted from a DMSO-dissolved stock solution. Directly following this incubation, the cells were placed on the stage of a fully motorized inverted microscope (**Carl Zeiss**; described in detail elsewhere: **Nooteboom *et al.*, 2012**). Fluorescence images were acquired within 15 min after incubation in the continuous presence of 15 nM extracellular TMRM using an 40x/1.3 NA Plan NeoFluar objective (**Carl Zeiss**), 540 nm excitation light delivered by a monochromator (**TILL Photonics, Gräfelfing, Germany**), a 560 nm dichroic mirror (#XF2017; **Omega, Brattleboro, VT, USA**), a 656 long pass emission filter (XF3085; **Omega**) and a CoolSNAP HD camera (**Roper Scientific, Evry Cedex, France**). For each cell, mitochondrial TMRM fluorescence was manually determined in two regions of interest (ROIs) defined in a mitochondria-dense and nucleoplasmic part of the cell and corrected for background using an ROI outside of the cell (**Fig. EV2D**).

Quantification of mitochondrial DNA content **-** Total DNA was isolated using the QIAamp DNA Mini Kit (**Qiagen, Manchester, UK**), according to the manufacturer's guidelines. DNA was eluted (100 µl elution buffer), and concentration was determined by NanoDrop (Labtech International, UK). To avoid dilution bias (**Malik *et al.*, 2011**), 30 µl of template DNA at a concentration of 10 ng/ µl was fragmented by sonication for 10 min at 38 kHz in a bath sonicator (**Pulsatron 55; Kerry Ultrasonics, London, UK**). Real-time qPCR was used to quantify absolute copy number of mtDNA per cell using primer sequences targeting human mtDNA (hMito) and the human nuclear gene beta-2-microglobulin (hB2M) (see: **Thubron *et al.*, 2019** for primer sequences). Each 10 µl reaction consisted of 8 µl Master Mix (5 µl 2x Quantifast SYBR Green Master Mix (**Qiagen**), 500 nM forward and reverse primer, made up to volume with RNAase-free water) and 2 µl total DNA. Samples were loaded onto a 96-well plate in triplicate alongside a standard curve consisting of a serial dilution of 10^8–10^2 copies of primer-specific PCR amplicons. All reactions were performed using the LightCycler 96 Real Time PCR System (**Roche Diagnostics Merck**) and adhering to the MIQE (minimum information for publication of quantitative real-time PCR experiments) guidelines (**Bustin *et al.*, 2009**). Absolute mtDNA copy number was calculated using the standard curve and is presented as a ratio of mitochondrial (hMito) to nuclear (hB2M) targets, representing cellular mtDNA content as described previously (MtN; **Malik *et al.*, 2011; Ajaz *et al.*, 2015**).

Electron microscopy - This approach was adapted from our earlier study (**Koopman *et al.*, 2008a**). Cells were seeded on Corning 35 mm dishes (430166), induced with doxycycline and optionally treated with CAP as described for the TMRM measurements (see above). Cells were fixed for 1 h in 2% glutaraldehyde in 0.1 M sodium cacodylate buffer (CaCo) and post-fixed for 30 min in 1% osmium tetroxide and 1% potassium ferrocyanide in 0.1 M CaCo. After being washed in buffer, cells were dehydrated in an ascending series of aqueous ethanol and were subsequently transferred via a mixture of ethanol and Epon to pure Epon as embedding medium. Sections of 80 nm were cut parallel to the bottom of the dishes, contrasted with 2%

14602075, 2023, 7, Downloaded from https://www.embopress.org/doi/10.15252/embj.2021108533 by Wageningen University and Research Bibliotheek, Wiley Online Library on [11/08/2023]. See the Terms and Conditions (https://onlinelibrary.wiley.com/terms-and-conditions) on Wiley Online Library for rules of use; OA articles are governed by the applicable Creative Commons License

uranyl acetate, counterstained with lead citrate and examined in a JEOL JEM 1400 electron microscope (**JEOL Europe B.V., Nieuw-Vennep, The Netherlands**) operating at 80 kV. Mitochondrial length was determined with Fiji software (https://imagej.net/Fiji) using the Analyse/Measure option and drawing a line transecting the mitochondrion. The number of cristae was manually counted. Next, for each mitochondrion the number of cristae per µm was calculated by dividing the number of cristae by mitochondrial length.

Simulation modelling of mitochondrial FRAP experiments - Our FRAP analysis demonstrates that all AcGFP1 concatemers are highly mobile within the mitochondrial matrix in the absence of chloramphenicol (*i.e.* $F_\infty > 91\%$; **Table 1**). To allow interpretation of T_{mono} in terms of a mitochondrial matrix solvent-dependent solute diffusion constant ($D_{solvent}$) and calculation of mitochondrial matrix solvent viscosity ($\eta_{solvent}$; see below), we developed a particle-based Brownian Dynamics (BD) simulation model (*e.g.* **Erban, 2014; Huber & McCammon, 2019**). Fluorescence correlation spectroscopy (FCS) experiments demonstrated that EYFP in the mitochondrial matrix is not affecting its own diffusion up to a concentration of 10 µM (**Willems *et al.*, 2009**). Therefore, in the BD model we routinely used an FP concentration (C_P) of 10 µM and assumed that FPs move independently. Given the fact that AcGFP1 is an inert monomeric protein (**Bulina *et al.*, 2006; Bell *et al.*, 2007**), with no known binding partners, it was further assumed that AcGFP1 does not bind to the MIM (*i.e.* individual FP molecules display reflections at the MIM). In BD simulations, the three dimensional (3D) position $\mathbf{r}_i$ of the i^{th} particle as a function of time t is integrated over a time step Δt according to:

$$\mathbf{r}_i(t+\Delta t) = \mathbf{r}_i(t) + \sqrt{2D_{solvent}\Delta t}\,\boldsymbol{\theta}_i(t) \qquad \textbf{[Equation-IV]}$$

where the three components to the random vector $\boldsymbol{\theta}_i(t)$ have zero mean, unit standard deviation and are devoid of correlations (Markovian). The diffusion coefficient was varied between 0.5 and 50 $\mu m^2/s$ and the time step was set at $\Delta t = 10^{-5}\ \mu m^2/D_{solvent}$ across all simulations. The mitochondrion was modelled as a cylinder with a radius R_{mito} and a length L_{mito}. (**Appendix Fig. S3A**). These parameters were experimentally determined (**Table 1**) by intensity profile analyses as described previously (see: **Willems *et al.*, 2009** and **Appendix Fig. S2F**). In order to account for diffusion hindrance by mitochondrial cristae (**Ölveczky et al., 1998; Partikian et al., 1998; Dieteren *et al.*, 2011**), we performed EM analysis of mitochondrial ultrastructure (**Fig. 5A** and **Table 1**). Based upon this analysis and information in the literature (**Appelhans *et al.*, 2011; Wilkens *et al.*, 2012; Wolf *et al.*, 2019; Segawa *et al.*, 2020; Hu *et al.*, 2020; Weissert *et al.*, 2021**) it was assumed in the model that: (**1**) mitochondria contained regularly arranged cristae of negligible thickness perpendicular to the longitudinal axis of the mitochondrion, (**2**) the orientations of the cristae alternated, with consecutive cristae blocking - $R_{mito} \leq z \leq -R_{mito} + h$ and $R_{mito} - h \leq z \leq R_{mito}$,, respectively, with h being the length of each crista (**Appendix Fig. S3A**). The presence of cristae increased the effective length of the "channel" that connected the two ends of the mitochondrion thereby increasing FP diffusion length (**Dieteren *et al.*, 2011**). In addition, the presence of cristae reduced the diffusive flow between consecutive mitochondrial sub-compartments. All flat and cylindrical walls were implemented using the appropriate bounce-back rules and it was verified that these rules conserved a uniform density near all surfaces. Simulations were initiated by randomly distributing FP-representing particles throughout the mitochondrial matrix volume. During the bleaching phase of the simulation (lasting 0.1 s; identical to experiments), all particles within the FRAP region (S_{FRAP} = 1.4 µm; identical to experiments) at one end of the cylinder were bleached. In the subsequent recovery simulation, the number of unbleached particles in this region was monitored to compute the FRAP signal. The generated FRAP curves were averaged over ten independent simulations (*e.g.* **Appendix Fig. S3B-C**). These average curves were fitted with the same mono-exponential equation (**[Equation-II]**) as the experimental data to extract T_{mono}. This also allowed calculation of F_m and F_∞ (as explained above). Analysis of the simulated FRAP data demonstrated that each curve ultimately converged to an F_∞ value of 1.0 (*i.e.* 100% fluorescence recovery; equalling F_m and F_∞ values of 1). To compute $D_{solvent}$ from the experimental T_{mono} values, LOG10($D_{solvent}$) was plotted as a function of LOG(T_{mono}) for the simulated FRAP curves and fitted with a straight line (**Fig. 3D** and **Appendix Fig. S3D**):

14602075, 2023, 7, Downloaded from https://www.embopress.org/doi/10.15252/embj.2021108533 by Wageningen University and Research Bibliotheek, Wiley Online Library on [11/08/2023]. See the Terms and Conditions (https://onlinelibrary.wiley.com/terms-and-conditions) on Wiley Online Library for rules of use; OA articles are governed by the applicable Creative Commons License

$$\mathrm{LOG10}(\mathrm{D_{solvent}}) = \mathrm{A} + \mathrm{B} \cdot \mathrm{LOG10}(T_{mono}) \qquad \textbf{[Equation-V]}$$

This yields values for A (intercept) and B (slope), which allows calculation of $D_{solvent}$ by inserting the experimental T_{mono} value.

Calculation of solvent viscosity ($\eta_{solvent}$) from $D_{solvent}$ using the He-Niemeyer equation - This equation is a modified Stokes-Einstein relationship that quantitatively links $D_{solvent}$ and $\eta_{solvent}$ for freely diffusing spherical and cylindrical molecules (**He & Niemeyer, 2003**). We have previously applied this equation in our FRAP analysis of matrix-diffusing AcGFP1 and AcGFP1[2] in HEK293 cells (**Dieteren *et al.*, 2011**):

$$\mathrm{D_{solvent}} = \frac{6.85 \cdot 10^{-8} \mathrm{T}}{\eta_{solvent} \cdot \sqrt{\mathrm{MW}^{\frac{1}{3}} \cdot \mathrm{R_G}}} \qquad \textbf{[Equation-VI]}$$

With T = temperature (in K; 293 K = 20 °C), $\eta_{solvent}$ = solvent viscosity (in cP; 1 cP = 10^{-3} Pa·s), MW = solute molecular weight (in g/mol), $D_{solvent}$ = solvent-dependent diffusion constant (in cm^2/s; 1.0 cm^2/s = $1.0x10^8$ $\mu m^2/s$), and R_G = radius of gyration (in Angstrom; Å; 1 Å = $1.0x10^{-10}$ m). Here we used **[Equation-VI]** to calculate $\eta_{solvent}$ from $D_{solvent}$ by rewriting as follows:

$$\eta_{solvent} = \frac{6.85 \cdot 10^{-8} \mathrm{T}}{\mathrm{D_{solvent}} \sqrt{\mathrm{MW}^{\frac{1}{3}} \cdot \mathrm{R_G}}} \qquad \textbf{[Equation-VII]}$$

For calculating $\eta_{solvent}$, the values of T (=293K), MW (determined using the protein sequence; **Appendix Table S1**) and $D_{solvent}$ (from the BD model) are known. This means that R_G needs to be determined for each AcGFP1 concatemer. Assuming that AcGFP1 displays a (minimal) spherical conformation, its R_G value can be calculated from the hydrodynamic radius (R_H) according to (**Dashevskaya *et al.*, 2008**):

$$\mathrm{R_G} = \sqrt{\frac{3}{5}} \cdot \mathrm{R_H} = 0.775 \cdot \mathrm{R_H} \qquad \textbf{[Equation-VIII]}$$

For AcGFP1, R_H = 20Å (**Terry *et al.*, 1995; Arrio-Dupont *et al.*, 2000; Lavalette *et al.*, 2006**) so R_G = 15.5Å, compatible with molecular modelling results for GFP (**Dashevskaya *et al.*, 2008**). Inspection of the GFP crystal structure (**Yang *et al.*, 1996**) predicts an AcGFP1 radius (R) and length (L) of 15Å and 40Å, respectively (**Figure EV1A**). Because AcGFP1[2], AcGFP1[3] and AcGFP1[4] may assume a non-spherical shape in the mitochondrial matrix solvent, **[Equation-VIII]** cannot be applied to determine their R_G value. In principle, AcGFP1[2], AcGFP1[3] and AcGFP1[4] can assume two extreme configurations: "compact" and "extended" (**Figure EV1B-G**). In their extended configuration, we assumed the AcGFP1 concatemer structure to be cylindrical. For a rigid cylinder, the R_G about its centroidal x-axis or y-axis is given by:

$$\mathrm{R_G} = \frac{\sqrt{9 \cdot \mathrm{R}^2 + 3 \cdot \mathrm{L}^2}}{6} \qquad \textbf{[Equation-IX]}$$

In which R is the radius and L is the length of the cylinder. In case of AcGFP1[2], its two AcGFP1 molecules are connected by a 14 AA linker (**Appendix Table S1**). For the compact AcGFP1[2] configuration R = 20Å, L = 60Å and R_G = 20.0 Å (**Table 1** and **Figure EV1B**). When maximally stretched out, this linker has a length of 50.4Å (**Minier & Sigel, 2004**). This means that for the extended AcGFP1[2] configuration R = 15Å, L = 130Å and R_G = 38Å (**Figure EV1C**). Similar calculations were carried out for AcGFP1[3] and AcGFP1[4] (**Table 1**) yielding R_G values of 20Å (AcGFP1[3]-compact), 73Å (AcGFP1[3]-extended), 20Å (AcGFP1[4]-

14602075, 2023, 7, Downloaded from https://www.embopress.org/doi/10.15252/embj.2021108533 by Wageningen University and Research Bibliotheek, Wiley Online Library on [11/08/2023]. See the Terms and Conditions (https://onlinelibrary.wiley.com/terms-and-conditions) on Wiley Online Library for rules of use; OA articles are governed by the applicable Creative Commons License

compact) and 102Å (AcGFP1[4]-extended). Inserting T, $D_{solvent}$, MW and R_G in **[Equation-VII]** was used to calculate $\eta_{solvent}$ for each AcGFP1 concatemer (**Table 1**).

Calculation of solvent viscosity ($\eta_{solvent}$) from $D_{solvent}$ using the Young equation - The Young equation (**Young, 1980**) predicts $\eta_{solvent}$ from $D_{solvent}$ based upon the MW of the solute:

$$D_{solvent} = 8.34 \times 10^{-8} \left(\frac{T}{\eta_{solvent} \cdot MW^{\frac{1}{3}}} \right) \qquad \textbf{[Equation-X]}$$

equalling:

$$\eta_{solvent} = 8.34 \times 10^{-8} \left(\frac{T}{D_{solvent} \cdot MW^{\frac{1}{3}}} \right) \qquad \textbf{[Equation-XI]}$$

With: T = temperature (in K), $\eta_{solvent}$ = solvent viscosity (in cP), MW = solute molecular weight (in g/mol), $D_{solvent}$ = solvent-dependent diffusion constant (in cm^2/s).

Calculation of solvent viscosity ($\eta_{solvent}$) from $D_{solvent}$ using the Tyn-Gusek equation - This approach allows prediction of $\eta_{solvent}$ from $D_{solvent}$ and R_G (**Tyn & Gusek, 1990**):

$$D_{solvent} = 5.78 \times 10^{-8} \left(\frac{T}{\eta_{solvent} \cdot R_G} \right) \qquad \textbf{[Equation-XII]}$$

equalling:

$$\eta_{solvent} = 5.78 \times 10^{-8} \left(\frac{T}{D_{solvent} \cdot R_G} \right) \qquad \textbf{[Equation-XIII]}$$

With T = temperature (in K), $\eta_{solvent}$ = solvent viscosity (in cP), $D_{solvent}$ = solvent-dependent diffusion constant (in cm^2/s), R_G = solute radius of gyration (in Å).

Calculation of solvent viscosity ($\eta_{solvent}$) from $D_{solvent}$ using the Stokes-Einstein equation - The Stokes-Einstein equation describes the diffusion of spherical particles through a liquid (**Einstein, 1905; Sutherland, 1905; von Smoluchowski, 1906**):

$$D_{solvent} = \frac{\kappa_B \cdot T}{6 \cdot \pi \cdot \eta_{solvent} \cdot R_H} \qquad \textbf{[Equation-XIV]}$$

equalling:

$$\eta_{solvent} = \frac{\kappa_B \cdot T}{6 \cdot \pi \cdot D_{solvent} \cdot R_H} \qquad \textbf{[Equation-XV]}$$

With T = temperature (in K), $\eta_{solvent}$ = solvent viscosity (in Pa·s; 1 Pa·s = 10^3 cP), $D_{solvent}$ = solvent-dependent diffusion constant (in m^2/s; 1.0 m^2/s = 1.0×10^{12} $\mu m^2/s$), κ_B = Boltzmann's constant (1.38065×10^{-23} J/K), R_H = solute hydrodynamic radius (in m). For AcGFP1, R_H = 20Å was taken from the literature (**Terry *et al.*, 1995; Arrio-Dupont *et al.*, 2000; Lavalette *et al.*, 2006**). The other AcGFP1 concatemers in their compact and extended configurations (**Figure EV1B-G**) were modelled as prolate ellipsoids (**Perrin, 1936**). In this case their R_H is given by:

14602075, 2023, 7, Downloaded from https://www.embopress.org/doi/10.15252/embj.2021108533 by Wageningen University and Research Bibliotheek, Wiley Online Library on [11/08/2023]. See the Terms and Conditions (https://onlinelibrary.wiley.com/terms-and-conditions) on Wiley Online Library for rules of use; OA articles are governed by the applicable Creative Commons License

$$R_H = \frac{\sqrt{(a^2-b^2)}}{\ln\left(\frac{a+\sqrt{(a^2-b^2)}}{b}\right)}$$ **[Equation-XVI]**

With a = major semi-axis of the ellipse = L/2; b = minor semi-axis of the ellipse = R; L = length of major axis of the ellipsoid (in Å); R = length of minor axis of the ellipsoid (in Å).

2. Appendix Supplementary Results

Chloramphenicol but not doxycycline induces a glycolytic switch - To allow interpretation of the observed CAP effects on FP diffusion in a functional context, we first studied the oxygen consumption rate (OCR) and extracellular acidification rate (ECAR) in HeLa parental cells (**Divakaruni *et al.*, 2022**). The incubation protocols were identical to those used for FP-induced cells ("+DOX" condition: 1 µg/ml; 24 h) and CAP-treatment of FP-induced cells (*i.e.* "+DOX+CAP": 40 µg/ml CAP for 48 h, followed by 40 µg/ml CAP + 1 µg/ml DOX for 24 h). As a control, we also determined the effect of CAP itself ("+CAP": 40 µg/ml for 72 h). After recording basal OCR/ECAR values, various chemicals were added (**Figure EV2A-B**) to inhibit the F_oF_1-ATPAse (oligomycin; OLI), induce mitochondrial uncoupling (FCCP) and inhibit OXPHOS complex I (rotenone; ROT) and complex III (antimycin A; AA). Basal and maximal OCR were slightly increased in the +DOX condition and greatly reduced in the +CAP and +DOX+CAP condition (**Figure EV2C**). Basal ECAR was slightly increased in the +DOX condition and greatly increased in the +CAP and +DOX+CAP condition (**Figure EV2C**). Basal/maximal OCR and basal ECAR values did not significantly differ between the +CAP and +DOX+CAP condition (**Figure EV2C**). Taken together, these results demonstrate that DOX treatment does not inhibit mitochondrial oxygen consumption. In contrast, CAP reduces mitochondrial respiration and increases ECAR, suggesting induction of a glycolytic switch, which was not affected by DOX.

Chloramphenicol increases mitochondrial TMRM fluorescence - Given the central role of the electron transport chain (ETC) in sustaining the mitochondrial membrane potential ($\Delta\psi$), it was next determined whether CAP affected the accumulation of the fluorescent cation TMRM, which can be used as a semi-quantitative readout of $\Delta\psi$ (**Koopman *et al.*, 2008b**). It was found that CAP treatment of HeLa parental cells increased and decreased the mitochondrial and nuclear TMRM fluorescence, respectively (**Figure EV2D**). This suggest that CAP treatment induces $\Delta\psi$ hyperpolarization.

Chloramphenicol and doxycycline do not increase the protein levels of mitochondrial unfolded protein response markers - Evidence in the literature suggests that CAP and DOX can induce the mitochondrial unfolded protein response (UPR^{mt}), which is classically linked to the accumulation of misfolded proteins in the mitochondrial matrix (**Houtkooper *et al.*, 2013; Moullan *et al.*, 2015; Shpilka and Haynes, 2018**). In this way, the observed effects on FP mobility might be due to a CAP- and/or DOX-induced accumulation of unfolded proteins in the mitochondria matrix. UPR^{mt} activation is characterized by upregulation of nuclear genes that encode mitochondrial stress proteins (**Zhao *et al.*, 2002**). The latter include mitochondrial heat shock protein 60 (mtHSP60) and the mitochondrial ATP-dependent Clp protease proteolytic subunit (CLPP). MtHSP60 promotor activity is controlled by the DNA damage-inducible transcript 3 protein (CHOP/CHOP-10/DDIT3) transcription factor. However, CHOP is also involved in the endoplasmic reticulum unfolded protein response (UPR^{ER}) and therefore not UPR^{mt} specific (**Zhao *et al.*, 2002**). In addition, UPR^{mt} activation was previously linked to increased protein levels of the mitochondrial Lon Peptidase 1 (LONP1; **Xu *et al.*, 2016**) and reduced function of mitochondrial heat shock protein 70 (mtHSP70/mortalin; **Burbulla *et al.*, 2014**). Analysis of HeLa parental cells (**Figure EV2E**) and FP-expressing cells (**Figure EV3A**) revealed no changes in the above protein levels upon treatment with DOX, CAP or DOX+CAP. For statistical analysis we reasoned that if DOX and/or CAP would affect the

14602075, 2023, 7, Downloaded from https://www.embopress.org/doi/10.15252/embj.2021108533 by Wageningen University and Research Bibliotheek, Wiley Online Library on [11/08/2023]. See the Terms and Conditions (https://onlinelibrary.wiley.com/terms-and-conditions) on Wiley Online Library for rules of use; OA articles are governed by the applicable Creative Commons License

level of the UPR^{mt}-linked proteins, the effect on the expression pattern of these proteins should be similar in all five HeLa cell lines (*i.e.* parental and four FP-expressing). This analysis revealed no UPR^{mt}-characteristic changes in the expression pattern of LONP1, mtHSP70, mtHSP70, CLPP and CHOP (**Figure EV3B**). These results suggest that UPR^{mt} activation is not responsible for the CAP-induced increase in $D_{solvent}$.

Chloramphenicol does not alter mitochondrial DNA copy number and the level of key mitochondrial fission and fusion proteins - Within cells, mtDNA is associated in nucleoprotein complexes ("nucleoids") and evidence in *E. coli* demonstrated that nucleoids undergo changes in shape and compaction upon CAP treatment (**Van Helvoort *et al.*, 1996**). Mitochondrial cristae structure also appears to compartmentalize nucleoids thereby preventing their free matrix diffusion (**Nicholls & Gustafsson, 2018**). Substantial nucleoid aggregation was observed upon loss of specific isoforms of the key MIM fusion protein Optic atrophy protein 1 (OPA1), which controls cristae structure and might be involved in mtDNA to MIM attachment (**Elachouri *et al.*, 2011**). Moreover, CAP prevented stress-induced OPA1 processing during dysfunction of the mitochondrial AAA protease AFG3L2 (**Richter *et al.*, 2019**). In this way, alterations in mtDNA and/or OPA1 level/processing might affect solute diffusion in CAP-treated cells. Here we observed that CAP treatment did not affect mtDNA copy number in HeLa parental cells (**Figure EV2F**). Similarly, the level of OPA1 and two other key MOM fission/fusion proteins (DRP1, MFN2) was not affected by CAP (**Figure EV2G**). This demonstrates that the observed CAP-induced increase in $D_{solvent}$ is not linked to alterations in the levels of mtDNA, OPA1, DRP1 or MFN2.

Predicted level of macromolecules and volume exclusion in the absence and presence of CAP - To obtain an semiquantitative estimate of the degree of macromolecular crowding within the mitochondrial matrix solvent of HeLa cells, we used human serum albumin (HSA) as a theoretical crowding agent. The MW of hydrated HSA equals 91.675 kDa (*i.e.* 91.675 $x10^3$ g/mol). Structurally, hydrated HSA is a prolate ellipsoid with semi-diameters: a = 8.2 nm and b = 2.1 nm. Computing the volume of this ellipsoid ($V_{ellipsoid,prolate} = (4/3)\cdot\pi\cdot b^2\cdot a$) yields a HSA molecular volume of 151 nm^3 (*i.e.* $1.51\cdot10^{-22}$ l). The total volume of the mitochondrial matrix (V_{mito}) equals ≈ $8.0\cdot10^{-16}$ l (**Table 1**). This means that ≈ $5.28\cdot10^6$ HSA molecules will fit in the mitochondrial matrix.

- In the absence of CAP, the matrix solvent viscosity ($\eta_{solvent}$) was maximally 4.57 cP (**Fig. 4C**). At 20° C this viscosity value was reached at HSA concentrations of ≈ 198 kg/m^3 in distilled water (**Monkos, 2004**). This concentration equals $198/91.675\cdot10^3 = 2.16\cdot10^{-3}$ mol and $2.16\cdot10^{-3}$ x $6.0221\cdot10^{23}$ (N_A) = $1.30\cdot10^{21}$ molecules/l. With a V_{mito} of $8.0\cdot10^{-16}$ l this equals a total number of $1.30\cdot10^{21}$ x $8.0\cdot10^{-16}$ = $1.04\cdot10^6$ molecules. These molecules occupy a volume fraction of $1.04\cdot10^6$ / $5.28\cdot10^6$ = 19.7% of the total mitochondrial matrix volume.

In CAP-treated cells $\eta_{solvent}$ increased to a maximal value of 37.5 cP (**Fig. 5G**), being equivalent to a HSA concentration of ≈ 328 kg/m^3 (**Monkos, 2004**). These concentrations are equivalent to $1.72\cdot10^6$ molecules in the mitochondrial matrix, which suggests that in the presence of CAP 32.7% of the total mitochondrial matrix volume is occupied by proteins. The HSA-occupied volume is not accessible by other molecules, a phenomenon described as the "excluded volume" effect (**Minton, 1981**). In this sense, the predicted HSA volume fractions in the absence and presence of CAP agree with those reported in *E. Coli* being between 5% and 40% of the cell volume (**Akabayov *et al.*, 2013**).

14602075, 2023, 7, Downloaded from https://www.embopress.org/doi/10.15252/embj.2021108533 by Wageningen University and Research Bibliotheek, Wiley Online Library on [11/08/2023]. See the Terms and Conditions (https://onlinelibrary.wiley.com/terms-and-conditions) on Wiley Online Library for rules of use; OA articles are governed by the applicable Creative Commons License

3. Appendix Supplementary Figures

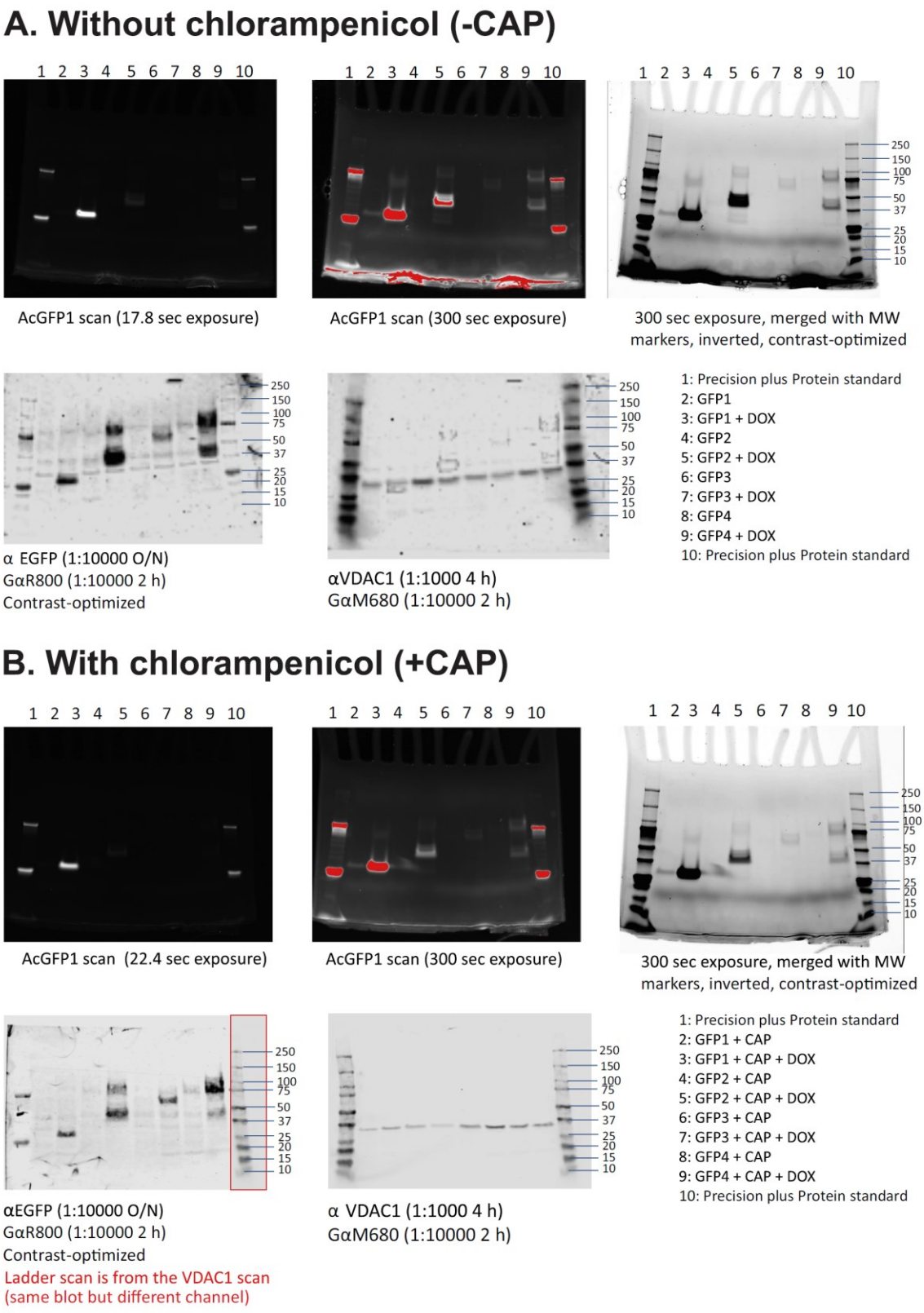

Appendix Figure S1: Original in-gel fluorescence scans and Western blots. The data in panel A was used to create **Fig. 2B**. The data in panel B is virtually identical to panel A, but was obtained for cells cultured in the presence of chloramphenicol (CAP).

14602075, 2023, 7, Downloaded from https://www.embopress.org/doi/10.15252/embj.2021108533 by Wageningen University and Research Bibliotheek, Wiley Online Library on [11/08/2023]. See the Terms and Conditions (https://onlinelibrary.wiley.com/terms-and-conditions) on Wiley Online Library for rules of use; OA articles are governed by the applicable Creative Commons License

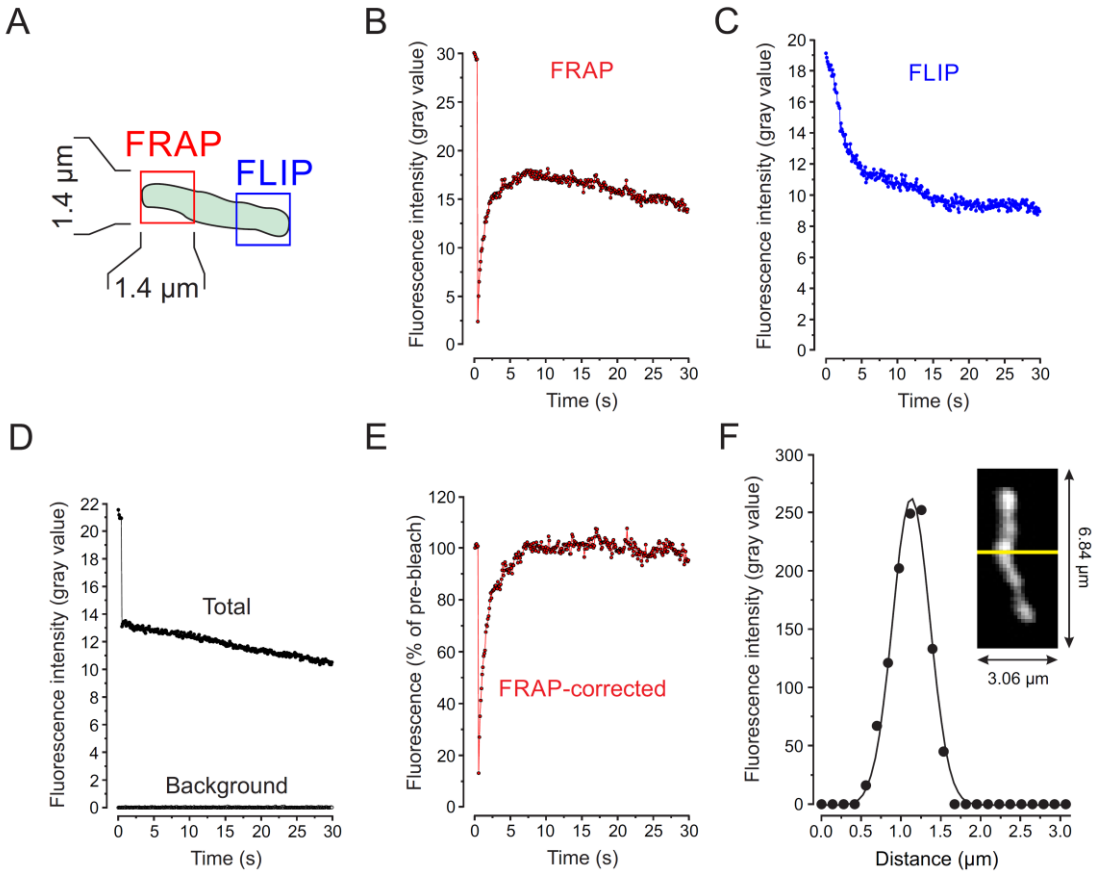

Appendix Figure S2: Analysis of mitochondrial fluorescence recovery after photobleaching (FRAP) experiments and quantification of mitochondrial radius (R_{mito}) and length (L_{mito}). In this typical example, a FRAP recording from a mitochondrion in an mitochondria-targeted AcGFP1-expressing HeLa cell is presented. (**A**) Geometry of the FRAP experiment. Two regions of interest (ROIs) were placed on both ends of the mitochondrion. AcGFP1 photobleaching was performed using a 1.4x1.4 µm FRAP region. Only single mitochondria that were fully located within the focal plane were used for analysis (confirmed by an axial scan). Only mitochondria in which FRAP was paralleled by fluorescence loss in photobleaching (FLIP) in a part distal to the FRAP region were considered to possess a continuous mitochondrial matrix and included in the analysis. (**B**) Time course of the fluorescence signal in the FRAP region. First, a pre-bleach fluorescence level was recorded, after which AcGFP1 was photobleached (fast signal drop) and fluorescence recovery (slower increase) was measured. (**C**) Time course of the fluorescence signal in the FLIP region. (**D**) Fluorescence signal in a ROI placed just outside the mitochondrion ("Background") and a rotated rectangular ROI around the complete mitochondrion ("Total"). (**E**) Time course of the corrected FRAP curve. In our experiments the size of the FRAP region is relatively large in comparison to the total size of the mitochondrion. Therefore, the experimental FRAP curve in panel B was corrected using the information in panel C and D using **[Equation-I]**. This also corrects for photobleaching during image acquisition (visible in panel D; total signal). (**F**) Determination of mitochondrial diameter (D_{mito}) from confocal microscopy fluorescence images (**Willems *et al.*, 2009**). Mitochondrial diameter D_{mito} (equalling $2 \cdot R_{mito}$) was assessed by quantifying the intensity of a 1 pixel wide profile perpendicular to the long axis of the mitochondrial filament (yellow line; image was linearly contrast stretched for visualization purposes). The width (w) of this profile at its half-maximal height is determined by fitting a Gaussian curve: $y=y_0+\{A/[w\cdot\sqrt{(\pi/2)}]\}\cdot EXP\{-2\cdot[(x-x_c)^2/w^2]\}$. For the given example this yielded $\underline{w}$=0.469 µm (*i.e.* R_{mito}=0.248 µm) and R^2=0.988. A similar strategy was used to determine mitochondrial length (L_{mito}) by analysing the intensity profile along the length axis of the mitochondrion.

14602075, 2023, 7, Downloaded from https://www.embopress.org/doi/10.15252/embj.2021108533 by Wageningen University and Research Bibliotheek, Wiley Online Library on [11/08/2023]. See the Terms and Conditions (https://onlinelibrary.wiley.com/terms-and-conditions) on Wiley Online Library for rules of use; OA articles are governed by the applicable Creative Commons License

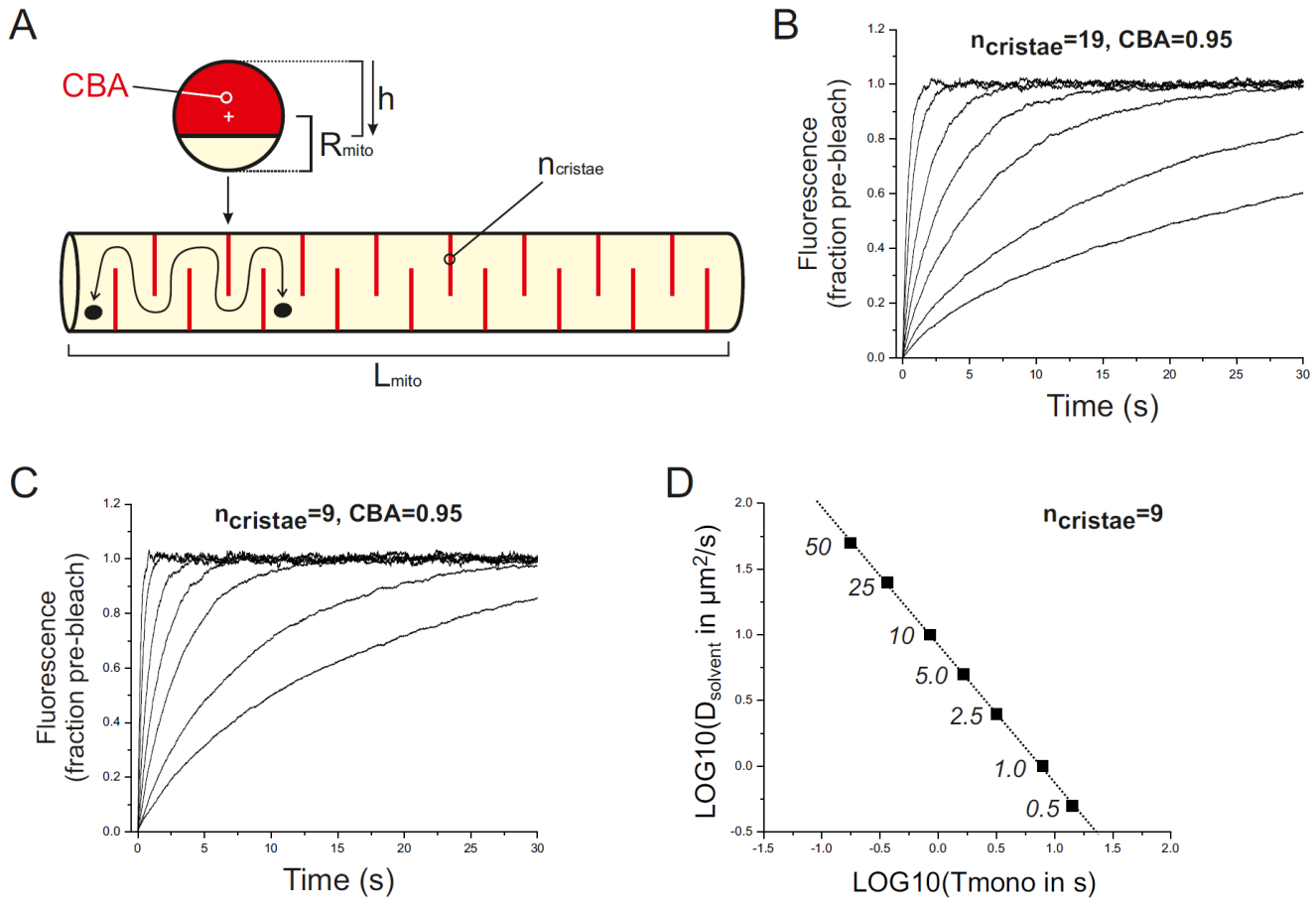

Appendix Figure S3: Synthetic FRAP data generated by the BD model. (**A**) Geometry of the BD model. See **Appendix** and **Results** for details. (**B**) Simulated FRAP curves for different values of the solvent-dependent diffusion constant ($D_{solvent}$; see panel D for exact values in $\mu m^2/s$). The number of cristae/mito ($n_{cristae}$) equalled 19. The cristae-blocked area (CBA) equalled 0.95. (**C**) Same as panel B but now for $n_{cristae}$ = 9 and CBA=0.95. (**D**) Linear relationship **[Equation-VI]** between the FRAP recovery time constant (T_{mono}) and the $D_{solvent}$ value (logarithmic scale) for the data in panel C (R=-0.999, p<0.0001; A(intercept)=0.923±0.00569(SE); B(slope)= -1.05±0.00841 (SE)).

14602075, 2023, 7, Downloaded from https://www.embopress.org/doi/10.15252/embj.2021108533 by Wageningen University and Research Bibliotheek, Wiley Online Library on [11/08/2023]. See the Terms and Conditions (https://onlinelibrary.wiley.com/terms-and-conditions) on Wiley Online Library for rules of use; OA articles are governed by the applicable Creative Commons License

A

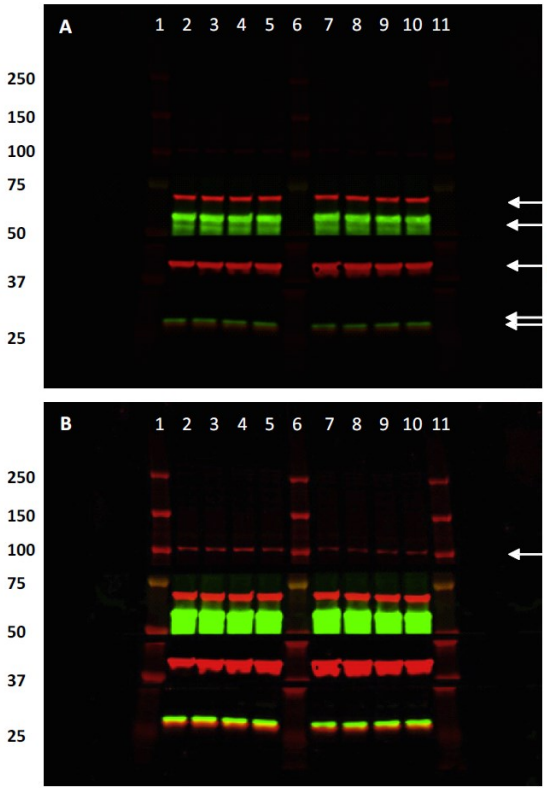

Legend:

1. Precision Plus Protein standards Dual color
2. HeLa T-Rex Flp-In cox8-AcGFP1-CAP/-DOX
3. HeLa T-Rex Flp-In cox8-AcGFP1-CAP/+DOX
4. HeLa T-Rex Flp-In cox8-AcGFP1 +CAP/-DOX
5. HeLa T-Rex Flp-In cox8-AcGFP1 +CAP/+DOX
6. Precision Plus Protein standards Dual color
7. HeLa T-Rex Flp-In cox8-AcGFP2-CAP/-DOX
8. HeLa T-Rex Flp-In cox8-AcGFP2-CAP/+DOX
9. HeLa T-Rex Flp-In cox8-AcGFP2 +CAP/-DOX
10. HeLa T-Rex Flp-In cox8-AcGFP2 +CAP/+DOX
11. Precision Plus Protein standards Dual color

- CAP treatment: 72h (40 µg/ml)
- DOX induction: 24h (1 µg/ml)
- Loaded: 20 µg total protein/lane
- 4-15% SDS-PAGE

- LONP1: 106 kDa
- mtHSP70: 70 kDa
- mtHSP60: 60 kDa
- β-actin: 42 kDa
- CLPP: 30 kDa
- CHOP: 29 kDa

- A = Auto scan
- B = Enhanced

B

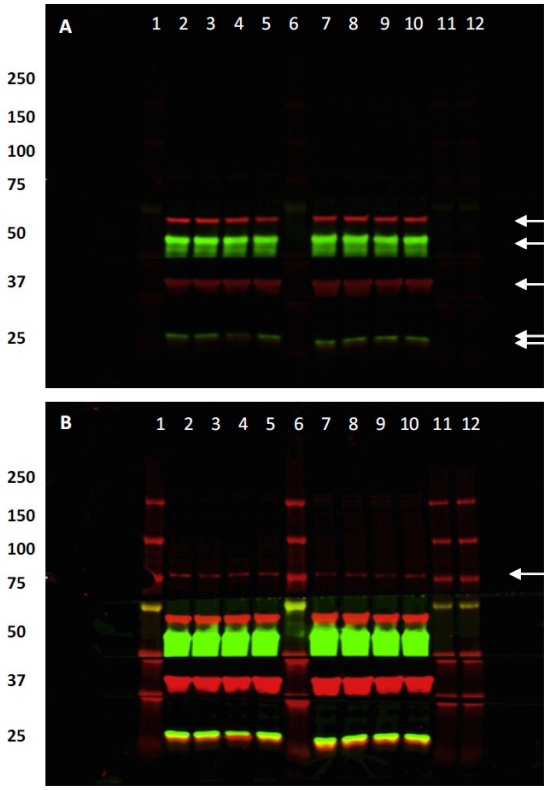

Legend:

1. Precision Plus Protein standards Dual color
2. HeLa T-Rex Flp-In cox8-AcGFP3-CAP/-DOX
3. HeLa T-Rex Flp-In cox8-AcGFP3-CAP/+DOX
4. HeLa T-Rex Flp-In cox8-AcGFP3 +CAP/-DOX
5. HeLa T-Rex Flp-In cox8-AcGFP3 +CAP/+DOX
6. Precision Plus Protein standards Dual color
7. HeLa T-Rex Flp-In cox8-AcGFP4-CAP/-DOX
8. HeLa T-Rex Flp-In cox8-AcGFP4-CAP/+DOX
9. HeLa T-Rex Flp-In cox8-AcGFP4 +CAP/-DOX
10. HeLa T-Rex Flp-In cox8-AcGFP4 +CAP/+DOX
11. Precision Plus Protein standards Dual color
12. Precision Plus Protein standards Dual color

- CAP treatment: 72h (40 µg/ml)
- DOX induction: 24h (1 µg/ml)
- Loaded: 20 µg total protein/lane
- 4-15% SDS-PAGE

- LONP1: 106 kDa
- mtHSP70: 70 kDa
- mtHSP60: 60 kDa
- β-actin: 42 kDa
- CLPP: 30 kDa
- CHOP: 29 kDa

- A = Auto scan
- B = Enhanced

Appendix Figure S4: Original blots for analysis of UPR^{mt} proteins in FP-expressing cells.

14602075, 2023, 7, Downloaded from https://www.embopress.org/doi/10.15252/embj.2021108533 by Wageningen University and Research Bibliotheek, Wiley Online Library on [11/08/2023]. See the Terms and Conditions (https://onlinelibrary.wiley.com/terms-and-conditions) on Wiley Online Library for rules of use; OA articles are governed by the applicable Creative Commons License

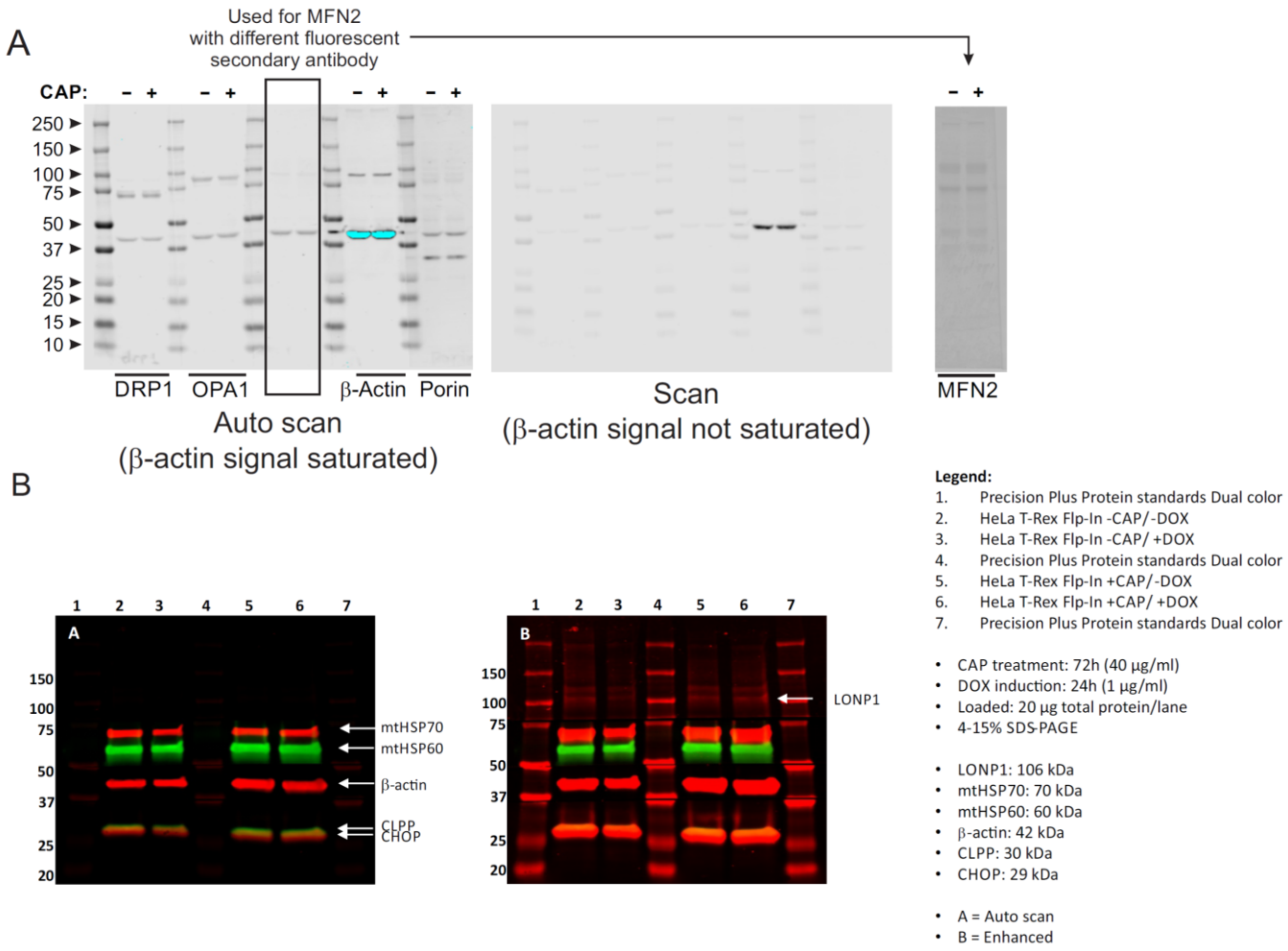

Appendix Figure S5: Original blots for analysis of fission/fusion (panel A) and UPR^{mt} proteins (panel B) in HeLa parental cells.

14602075, 2023, 7, Downloaded from https://www.embopress.org/doi/10.15252/embj.2021108533 by Wageningen University and Research Bibliotheek, Wiley Online Library on [11/08/2023]. See the Terms and Conditions (https://onlinelibrary.wiley.com/terms-and-conditions) on Wiley Online Library for rules of use; OA articles are governed by the applicable Creative Commons License

4. Appendix Supplementary Tables

Appendix Supplementary Table S1: Protein sequences, MW and dimensions of the AcGFP1 concatemers

Sequence	MW and dimensions
Cox8-AcGFP1 MSVLTPLLLRGLTGSARRLPVPRAKIHSLPPHPAFLYKVVDDPPVMVSKGAELFTGIVPILI ELNGDVNGHKFSVSGEGEGDATYGKLTLKFICTTGKLPVPWPTLVTTLSYGVQCFSRYPD HMKQHDFFKSAMPEGYIQERTIFFEDDGNYKSRAEVKFEGDTLVNRIELTGTDFKEDGNI LGNKMEYNYNAHNVYIMTDKAKNGIKVNFKIRHNIEDGSVQLADHYQQNTPIGDGPVLL PDNHYLSTQSALSKDPNEKRDHMIYFGFVTAAAITHGMDELYK	MTS = 2.703 kDa Linker = 2.241 kDa AcGFP1 = 26.874 kDa **Total protein (+MTS) = 31.818 kDa** **Total protein (-MTS) = 29.115 kDa**
Cox8-AcGFP1[2] MSVLTPLLLRGLTGSARRLPVPRAKIHSLPPHPAFLYKVVDDPPVMVSKGAELFTGIVPILI ELNGDVNGHKFSVSGEGEGDATYGKLTLKFICTTGKLPVPWPTLVTTLSYGVQCFSRYPD HMKQHDFFKSAMPEGYIQERTIFFEDDGNYKSRAEVKFEGDTLVNRIELTGTDFKEDGNI LGNKMEYNYNAHNVYIMTDKAKNGIKVNFKIRHNIEDGSVQLADHYQQNTPIGDGPVLL PDNHYLSTQSALSKDPNEKRDHMIYFGFVTAAAITHGMDELYKHPAFLYKVVDDPPVM VSKGAELFTGIVPILIELNGDVNGHKFSVSGEGEGDATYGKLTLKFICTTGKLPVPWPTLV TTLSYGVQCFSRYPDHMKQHDFFKSAMPEGYIQERTIFFEDDGNYKSRAEVKFEGDTLV NRIELTGTDFKEDGNILGNKMEYNYNAHNVYIMTDKAKNGIKVNFKIRHNIEDGSVQLA DHYQQNTPIGDGPVLLPDNHYLSTQSALSKDPNEKRDHMIYFGFVTAAAITHGMDELYK	MTS = 2.703 kDa Linker = 2.241 kDa AcGFP1 = 26.874 kDa Linker = 14AA = 50.4 Å = 1.597 kDa AcGFP1 = 26.874 kDa **Total protein (+MTS) = 60.289 kDa** **Total protein (-MTS) = 57.586 kDa**
Cox8-AcGFP1[3] MSVLTPLLLRGLTGSARRLPVPRAKIHSLPPHPAFLYKVVDDPPVSIKLLAMVSKGAELFT GIVPILIELNGDVNGHKFSVSGEGEGDATYGKLTLKFICTTGKLPVPWPTLVTTLSYGVQC FSRYPDHMKQHDFFKSAMPEGYIQERTIFFEDDGNYKSRAEVKFEGDTLVNRIELTGTDF KEDGNILGNKMEYNYNAHNVYIMTDKAKNGIKVNFKIRHNIEDGSVQLADHYQQNTPIG DGPVLLPDNHYLSTQSALSKDPNEKRDHMIYFGFVTAAAITHGMDELYKDIPPHPAFLYK VVDDPPVMVSKGAELFTGIVPILIELNGDVNGHKFSVSGEGEGDATYGKLTLKFICTTGK LPVPWPTLVTTLSYGVQCFSRYPDHMKQHDFFKSAMPEGYIQERTIFFEDDGNYKSRAEV KFEGDTLVNRIELTGTDFKEDGNILGNKMEYNYNAHNVYIMTDKAKNGIKVNFKIRHNIE DGSVQLADHYQQNTPIGDGPVLLPDNHYLSTQSALSKDPNEKRDHMIYFGFVTAAAITH GMDELYKHPAFLYKVVDDPPVSTCIPVMVSKGAELFTGIVPILIELNGDVNGHKFSVSGE GEGDATYGKLTLKFICTTGKLPVPWPTLVTTLSYGVQCFSRYPDHMKQHDFFKSAMPEG YIQERTIFFEDDGNYKSRAEVKFEGDTLVNRIELTGTDFKEDGNILGNKMEYNYNAHNVY IMTDKAKNGIKVNFKIRHNIEDGSVQLADHYQQNTPIGDGPVLLPDNHYLSTQSALSKDP NEKRDHMIYFGFVTAAAITHGMDELYK	MTS = 2.703 kDa Linker = 2.867 kDa AcGFP1 = 26.874 kDa Linker = 18AA = 64.8 Å = 2.019 kDa AcGFP1 = 26.874 kDa Linker = 20AA = 72.0 Å = 2.197 kDa AcGFP1 = 26.874 kDa **Total protein (+MTS) = 90.408 kDa** **Total protein (-MTS) = 87.705 kDa**
Cox8[2]-AcGFP1[4] MSVLTPLLLRGLTGSARRLPVPRAKIHSLGDPMSVLTPLLLRGLTGSARRLPVPRAKIHSL PPEGDLKPVMVSKGAELFTGIVPILIELNGDVNGHKFSVSGEGEGDATYGKLTLKFICTTG KLPVPWPTLVTTLSYGVQCFSRYPDHMKQHDFFKSAMPEGYIQERTIFFEDDGNYKSRAE VKFEGDTLVNRIELTGTDFKEDGNILGNKMEYNYNAHNVYIMTDKAKNGIKVNFKIRHN IEDGSVQLADHYQQNTPIGDGPVLLPDNHYLSTQSALSKDPNEKRDHMIYFGFVTAAAIT HGMDELYKHPAFLYKVVDDPPVSIKLLAMVSKGAELFTGIVPILIELNGDVNGHKFSVSG EGEGDATYGKLTLKFICTTGKLPVPWPTLVTTLSYGVQCFSRYPDHMKQHDFFKSAMPE GYIQERTIFFEDDGNYKSRAEVKFEGDTLVNRIELTGTDFKEDGNILGNKMEYNYNAHNV YIMTDKAKNGIKVNFKIRHNIEDGSVQLADHYQQNTPIGDGPVLLPDNHYLSTQSALSKD PNEKRDHMIYFGFVTAAAITHGMDELYKDIPPHPAFLYKVVDDPPVMVSKGAELFTGIVP ILIELNGDVNGHKFSVSGEGEGDATYGKLTLKFICTTGKLPVPWPTLVTTLSYGVQCFSRY PDHMKQHDFFKSAMPEGYIQERTIFFEDDGNYKSRAEVKFEGDTLVNRIELTGTDFKEDG NILGNKMEYNYNAHNVYIMTDKAKNGIKVNFKIRHNIEDGSVQLADHYQQNTPIGDGPV LLPDNHYLSTQSALSKDPNEKRDHMIYFGFVTAAAITHGMDELYKHPAFLYKVVDDPPV STCIPVMVSKGAELFTGIVPILIELNGDVNGHKFSVSGEGEGDATYGKLTLKFICTTGKLP VPWPTLVTTLSYGVQCFSRYPDHMKQHDFFKSAMPEGYIQERTIFFEDDGNYKSRAEVK FEGDTLVNRIELTGTDFKEDGNILGNKMEYNYNAHNVYIMTDKAKNGIKVNFKIRHNIED GSVQLADHYQQNTPIGDGPVLLPDNHYLSTQSALSKDPNEKRDHMIYFGFVTAAAITHG MDELYK	MTS = 2.703 kDa Linker = 0.738 kDa MTS = 2.703 kDa Linker = 1.401 kDa AcGFP1 = 26.874 kDa Linker = 20AA = 72.0 Å = 2.223 kDa AcGFP1 = 26.874 kDa Linker = 18AA = 64.8 Å = 2.019 kDa AcGFP1 = 26.874 kDa Linker = 20AA = 72.0 Å = 2.198 kDa AcGFP1 = 26.874 kDa **Total protein (+MTS-linker-MTS) = 121.481 kDa** **Total protein (-MTS-linker-MTS) = 115.337 kDa**

Remarks: Mitochondrial Target Sequence (MTS), the 25-residue Cox8 sequence (**Rizzutto et al., J. Biol. Chem., 1989**). Linker sequences . Linker sequences. AcGFP1 sequence (monomeric *Aequorea coerulescens* Green Fluorescent Protein). The linkers highlighted in black were not considered for geometry calculations of the proteins. Molecular weight was calculated directly from the protein sequence using the pI/Mw tool (web.expasy.org/compute_pi).One (1) Dalton (Da) equals 1 g/mol.

14602075, 2023, 7, Downloaded from https://www.embopress.org/doi/10.15252/embj.2021108533 by Wageningen University and Research Bibliotheek, Wiley Online Library on [11/08/2023]. See the Terms and Conditions (https://onlinelibrary.wiley.com/terms-and-conditions) on Wiley Online Library for rules of use; OA articles are governed by the applicable Creative Commons License

Appendix Supplementary Table S2: Experimental $D_{solvent}$ values in aqueous solution and in the cell

Protein/molecule	MW (kDa)	LOG10 (MW)	$D_{solvent}$ (µm²/s)	LOG10 ($D_{solvent}$)	Reference
GLOBULAR OR SPHERICAL CONFORMATION IN AQUEOUS SOLUTION Fitting results of LOG(MW) *vs.* LOG($D_{solvent}$): **Y=A+B·X:** R=-0.986; P<0.0001; A=2.45±0.0154(SE); B=-0.360±0.00525(SE)					
Insulin	12	1.079	147.0	2.167	**Gribbon *et al.*, 1998**
Cytochrome-*c*	13	1.126	114.0	2.057	**Young *et al.*, 1980**
Ribonuclease	13	1.102	131.0	2.117	**Tyn & Gusek, 1990**
Alpha-lactalbumin	13	1.124	106.0	2.025	**Tyn & Gusek, 1990**
Ribonuclease	14	1.137	117.0	2.068	**Tyn & Gusek, 1990**
Lysozyme	14	1.144	112.0	2.049	**Tyn & Gusek, 1990**
Myoglobin	16	1.204	113.0	2.053	**Tyn & Gusek, 1990**
Ribonuclease	17	1.230	102.0	2.009	**Tyn & Gusek, 1990**
Myokinase	21	1.322	160.0	2.204	**Arrio-Dupont et al., 2000**
Alpha-chymotrypsin (monomer)	21	1.328	102.0	2.009	**Young *et al.*, 1980**
Alpha-chymotrypsinogen	38	1.580	79.0	1.898	**He & Niemeyer, 2003**
Gamma-chymotrypsin	23	1.366	95.0	1.978	**Tyn & Gusek, 1990**
Chymotrypsin A	18	1.243	102.0	2.009	**Tyn & Gusek, 1990**
SBTI	22	1.334	88.0	1.944	**Gribbon *et al.*, 1998**
Ribosome 4S	23	1.365	75.8	1.880	**Tyn & Gusek, 1990**
Beta-casein	24	1.382	60.5	1.782	**Tyn & Gusek, 1990**
Riboflavin-binding protein	33	1.512	74.0	1.869	**Tyn & Gusek, 1990**
Pepsin	33	1.515	87.0	1.940	**Tyn & Gusek, 1990**
Beta-lactoglobulin	35	1.549	78.0	1.892	**Tyn & Gusek, 1990**
Ovalbumin	44	1.643	77.6	1.890	**Tyn & Gusek, 1990**
Phosphoglucomutase	60	1.778	63.8	1.805	**Arrio-Dupont *et al.*, 2000**
Phosphoglycerate kinase	47	1.670	63.8	1.805	**Tyn & Gusek, 1990**
Hemoglobin	63	1.799	69.0	1.839	**Tyn & Gusek, 1990**
Hemoglobin - earthworm	3700	3.568	12.0	1.079	**Papadopoulos *et al.*, 2000**
Bovine serum albumin	65	1.816	61.5	1.789	**Tyn & Gusek, 1990**
Beta-enolase	90	1.954	56.0	1.748	**Arrio-Dupont *et al.*, 2000**
Alpha-amylase	97	1.986	57.2	1.757	**Young *et al.*, 1980**
Citrate synthase	98	1.991	58.0	1.763	**Durchslag & Zipper, 1997**
Hexokinase	99	1.996	60.0	1.778	**Tyn & Gusek, 1990**
Glyceraldehyde-3-phosphate dehydrogenase	141	2.149	50.0	1.699	**Tyn & Gusek, 1990**

14603075, 2023, 7, Downloaded from https://www.embopress.org/doi/10.15252/embj.2021108533 by Wageningen University and Research Bibliotheek, Wiley Online Library on [11/08/2023]. See the Terms and Conditions (https://onlinelibrary.wiley.com/terms-and-conditions) on Wiley Online Library for rules of use; OA articles are governed by the applicable Creative Commons License

Lysine-trna ligase	138	2.140	43.0	1.633	**Tyn & Gusek, 1990**
Lactate dehydrogenase	138	2.141	51.0	1.708	**Tyn & Gusek, 1990**
Phosphofructokinase	142	2.152	53.0	1.724	**Tyn & Gusek, 1990**
Phosphofructokinase	160	2.204	42.0	1.623	**Tyn & Gusek, 1990**
IgG	160	2.204	40.5	1.607	**Arrio-Dupont *et al.*, 2000**
Phosphofructokinase	320	2.505	32.2	1.508	**Tyn & Gusek, 1990**
Beta-lactoglobulin A	147	2.167	42.0	1.623	**Tyn & Gusek, 1990**
Gamma-globulin	153	2.185	40.0	1.602	**Tyn & Gusek, 1990**
Gamma-globulin	162	2.210	37.0	1.568	**Tyn & Gusek, 1990**
Glycogen-phosphorylase	163	2.212	42.0	1.623	**Tyn & Gusek, 1990**
Glycogen-phosphorylase	185	2.267	41.2	1.615	**Tyn & Gusek, 1990**
Malate synthase	170	2.230	45.0	1.653	**Tyn & Gusek, 1990**
Malate synthase	187	2.272	45.0	1.653	**Tyn & Gusek, 1990**
Methionyl-tRNA synthetase	173	2.238	35.0	1.544	**Tyn & Gusek, 1990**
Pyruvate kinase	191	2.281	42.0	1.623	**Tyn & Gusek, 1990**
Catalase	225	2.352	41.0	1.613	**Tyn & Gusek, 1990**
Catalase	232	2.365	41.0	1.613	**Tyn & Gusek, 1990**
Catalase	248	2.394	43.0	1.633	**Papadopoulos *et al.*, 2000**
Catalase	250	2.398	45.0	1.653	**Tyn & Gusek, 1990**
Porphobilinogen synthase	270	2.431	42.0	1.623	**Tyn & Gusek, 1990**
Porphobilinogen synthase	240	2.380	42.0	1.623	**Tyn & Gusek, 1990**
Glutamate dehydrogenase	270	2.431	35.0	1.544	**Tyn & Gusek, 1990**
Glutamate dehydrogenase	312	2.494	35.0	1.544	**Tyn & Gusek, 1990**
Glutamate dehydrogenase	343	2.535	35.0	1.544	**Tyn & Gusek, 1990**
Edestin	310	2.491	39.3	1.594	**Tyn & Gusek, 1990**
Edestin	324	2.511	31.7	1.501	**Tyn & Gusek, 1990**
Adenovirus_Type_2_hexon	323	2.509	35.6	1.551	**Tyn & Gusek, 1990**
Adenovirus_Type_2_hexon	355	2.550	33.2	1.521	**Tyn & Gusek, 1990**
Phosphofructokinase	330	2.519	36.0	1.556	**Tyn & Gusek, 1990**
Phosphofructokinase	340	2.531	32.2	1.508	**Tyn & Gusek, 1990**
DNA-dependent_RNA+polymerase	360	2.556	33.0	1.519	**Tyn & Gusek, 1990**
Glycogen phosphorylase	370	2.568	33.0	1.519	**Tyn & Gusek, 1990**
Cytochrome c1	371	2.569	33.1	1.520	**Young *et al.*, 1980**
Ferritin	450	2.653	38.0	1.580	**Papadopoulos *et al.*, 2000**
Apoferritin	441	2.644	36.1	1.558	**Tyn & Gusek, 1990**
Apoferritin	460	2.663	36.1	1.558	**Tyn & Gusek, 1990**

14603075, 2023, 7, Downloaded from https://www.embopress.org/doi/10.15252/embj.2021108533 by Wageningen University and Research Bibliotheek, Wiley Online Library on [11/08/2023]. See the Terms and Conditions (https://onlinelibrary.wiley.com/terms-and-conditions) on Wiley Online Library for rules of use; OA articles are governed by the applicable Creative Commons License

Apoferritin	467	2.669	36.1	1.558	**Tyn & Gusek, 1990**
Fibronectin	510	2.708	22.7	1.356	**Durchslag & Zipper, 1997**
Beta-galactosidase	540	2.732	30.0	1.477	**Arrio-Dupont *et al.*, 2000**
Thyroglobulin	630	2.799	26.5	1.423	**Tyn & Gusek, 1990**
Thyroglobulin	650	2.813	26.5	1.423	**Tyn & Gusek, 1990**
Thyroglobulin	660	2.820	26.1	1.417	**Tyn & Gusek, 1990**
Ribosome S30	700	2.845	29.5	1.470	**Tyn & Gusek, 1990**
Alpha-crystallin	770	2.886	23.0	1.362	**Tyn & Gusek, 1990**
Alpha-crystallin	840	2.924	23.0	1.362	**Tyn & Gusek, 1990**
Alpha-crystallin	960	2.982	20.0	1.301	**Tyn & Gusek, 1990**
Alpha2-macroglobulin	820	2.914	24.1	1.382	**Tyn & Gusek, 1990**
Alpha2-macroglobulin	985	2.993	24.1	1.382	**Tyn & Gusek, 1990**
Haemocyanin	854	2.931	26.9	1.430	**Tyn & Gusek, 1990**
Ribosome S30	870	2.940	29.5	1.470	**Tyn & Gusek, 1990**
Ribosome S30	900	2.954	29.5	1.470	**Tyn & Gusek, 1990**
Beta-casein	1200	3.079	14.0	1.146	**Tyn & Gusek, 1990**
Ribosome S30	1000	3.000	29.5	1.470	**Tyn & Gusek, 1990**
Ribosome S50	1500	3.176	19.1	1.281	**Tyn & Gusek, 1990**
Ribosome S50	1550	3.190	19.1	1.281	**Tyn & Gusek, 1990**
Ribosome S50	1580	3.199	19.1	1.281	**Tyn & Gusek, 1990**
Ribosome S50	1800	3.255	19.1	1.281	**Tyn & Gusek, 1990**
Ribosome S70	3000	3.477	18.3	1.262	**Tyn & Gusek, 1990**
Fatty-acid synthase	2200	3.342	17.8	1.250	**Tyn & Gusek, 1990**
Fatty-acid synthase	2300	3.362	17.0	1.230	**Tyn & Gusek, 1990**
Pyruvate dehydrogenase	3780	3.577	12.0	1.079	**Tyn & Gusek, 1990**
Pyruvate dehydrogenase	4800	3.681	12.0	1.079	**Tyn & Gusek, 1990**
Satellite_tobacco_necrosis_virus	9000	3.954	10.7	1.029	**Tyn & Gusek, 1990**
Satellite_tobacco_necrosis_virus	1700	3.230	20.4	1.310	**Tyn & Gusek, 1990**
Turnip_yellow_mosaic_virus	1970	3.294	20.4	1.310	**Tyn & Gusek, 1990**
Turnip_yellow_mosaic_virus	3013	3.479	15.1	1.179	**Tyn & Gusek, 1990**
Turnip_yellow_mosaic_virus	3100	3.491	15.1	1.179	**Tyn & Gusek, 1990**
Alfalfa_mosaic_virus_(top)	3500	3.544	15.1	1.179	**Tyn & Gusek, 1990**
Bacteriophage_MS2_(native_protein)	3770	3.576	15.5	1.190	**Tyn & Gusek, 1990**
BacteriOphage fr	3600	3.556	16.0	1.204	**Durchslag & Zipper, 1997**
Bacteriophage_virus_R17	3620	3.559	14.0	1.146	**Tyn & Gusek, 1990**
Bacteriophage_virus_R17	3600	3.556	13.3	1.123	**Tyn & Gusek, 1990**

14603075, 2023, 7, Downloaded from https://www.embopress.org/doi/10.15252/embj.2021108533 by Wageningen University and Research Bibliotheek, Wiley Online Library on [11/08/2023]. See the Terms and Conditions (https://onlinelibrary.wiley.com/terms-and-conditions) on Wiley Online Library for rules of use; OA articles are governed by the applicable Creative Commons License

Bacteriophage_virus_R17	3700	3.568	13.3	1.123	**Tyn & Gusek, 1990**
Wild_cucumber_mosaic_virus_top_a	4190	3.622	13.3	1.123	**Tyn & Gusek, 1990**
Wild_cucumber_mosaic_virus_top_b	4000	3.602	12.9	1.111	**Tyn & Gusek, 1990**
Wild_cucumber_mosaic_virus_top_b	4300	3.633	12.9	1.111	**Tyn & Gusek, 1990**
Bromegrass_mosaic_virus	4400	3.643	12.9	1.111	**Tyn & Gusek, 1990**
Bromegrass_mosaic_virus	4400	3.643	15.5	1.190	**Tyn & Gusek, 1990**
Bromegrass_mosaic_virus	4700	3.672	15.5	1.190	**Tyn & Gusek, 1990**
Broad_bean_mottle_virus	5400	3.732	15.5	1.190	**Tyn & Gusek, 1990**
Broad_bean_mottle_virus	4750	3.677	14.4	1.158	**Tyn & Gusek, 1990**
Broad_bean_mottle_virus	4850	3.686	14.4	1.158	**Tyn & Gusek, 1990**
Broad_bean_mottle_virus	5000	3.699	14.4	1.158	**Tyn & Gusek, 1990**
Broad_bean_mottle_virus	5200	3.716	13.8	1.140	**Tyn & Gusek, 1990**
Turnip_yellow_mosaic_virus	5600	3.748	14.4	1.158	**Tyn & Gusek, 1990**
Turnip_yellow_mosaic_virus	4970	3.696	15.5	1.190	**Tyn & Gusek, 1990**
Turnip_yellow_mosaic_virus	5000	3.699	15.5	1.190	**Tyn & Gusek, 1990**
Tobacco_necrosis_virus	5530	3.743	15.5	1.190	**Tyn & Gusek, 1990**
Tobacco_necrosis_virus	6000	3.778	15.3	1.185	**Tyn & Gusek, 1990**
Southern_bean_mosaic_virus	7400	3.869	14.0	1.146	**Tyn & Gusek, 1990**
Southern_bean_mosaic_virus	6600	3.820	13.9	1.143	**Tyn & Gusek, 1990**
Southern_bean_mosaic_virus	6602	3.820	13.9	1.143	**Tyn & Gusek, 1990**
Southern bean mosaic virus	6630	3.822	13.4	1.127	**Durchslag & Zipper, 1997**
Alfalfa_mosaic_virus_(bottom)	6690	3.825	13.9	1.143	**Tyn & Gusek, 1990**
Alfalfa_mosaic_virus_(bottom)	6820	3.834	11.3	1.053	**Tyn & Gusek, 1990**
Alfalfa_mosaic_virus_(bottom)	6860	3.836	11.3	1.053	**Tyn & Gusek, 1990**
Alfalfa_mosaic_virus_(bottom)	6920	3.840	10.5	1.021	**Tyn & Gusek, 1990**
Tobacco_bushy_stunt_virus	7400	3.869	10.5	1.021	**Tyn & Gusek, 1990**
Bacteriophage_lambda_(enlarged_prehead)	10700	4.029	11.5	1.061	**Tyn & Gusek, 1990**
Bacteriophage_lambda_(processed_prehead)	17000	4.230	6.9	0.839	**Tyn & Gusek, 1990**
Bacteriophage_lambda_(empty_head)	18000	4.255	7.8	0.892	**Tyn & Gusek, 1990**
Bacteriophage_lambda_(unprocessed_head)	21000	4.322	6.4	0.806	**Tyn & Gusek, 1990**
Bacteriophage_lambda_(full_head)	22000	4.342	7.6	0.881	**Tyn & Gusek, 1990**
Lipid-containing_bacteriophage	56000	4.748	6.5	0.813	**Tyn & Gusek, 1990**
Rice dwarf virus	45000	4.653	5.5	0.740	**Durchslag & Zipper, 1997**
ELONGATED, FIBROUS STRUCTURE OR ROD-LIKE CONFORMATION IN AQUEOUS SOLUTION Fitting results of LOG(MW) *vs.* LOG($D_{solvent}$): **Y=A+B·X:** R=-0.990; P<0.0001; A=3.06±0.0542(SE); B=-0.715±0.0173(SE)					

14603075, 2023, 7, Downloaded from https://www.embopress.org/doi/10.15252/embj.2021108533 by Wageningen University and Research Bibliotheek, Wiley Online Library on [11/08/2023]. See the Terms and Conditions (https://onlinelibrary.wiley.com/terms-and-conditions) on Wiley Online Library for rules of use; OA articles are governed by the applicable Creative Commons License

Flagellin	42	1.620	54.0	1.732	**Tyn & Gusek, 1990**
Meromyosin	120	2.079	22.5	1.352	**Tyn & Gusek, 1990**
Fibrinogen	340	2.531	20.2	1.305	**Tyn & Gusek, 1990**
Myosin	493	2.693	11.6	1.064	**Tyn & Gusek, 1990**
Myosin	570	2.756	10.0	1.000	**Tyn & Gusek, 1990**
Myosin	594	2.774	8.7	0.940	**Tyn & Gusek, 1990**
RNA_of_tobacco_mosaic_virus	2150	3.332	7.0	0.843	**Tyn & Gusek, 1990**
DNA	4000	3.602	1.3	0.114	**Tyn & Gusek, 1990**
DNA	5000	3.699	1.3	0.114	**Tyn & Gusek, 1990**
DNA	6000	3.778	1.3	0.114	**Tyn & Gusek, 1990**
p1868	1232	3.091	7.0	0.845	**Prazeres, 2008**
PLN1	1386	3.142	6.0	0.778	**Prazeres, 2008**
Not available	1525	3.183	5.6	0.748	**Prazeres, 2008**
PK3A108	1535	3.186	5.4	0.728	**Prazeres, 2008**
pUC18	1773	3.249	5.4	0.732	**Prazeres, 2008**
pUC8	1793	3.254	4.9	0.690	**Prazeres, 2008**
pUC18-3A108	1847	3.266	4.8	0.681	**Prazeres, 2008**
pGem1a	2462	3.391	4.1	0.614	**Prazeres, 2008**
pBR322	2880	3.459	3.7	0.568	**Prazeres, 2008**
p30delta	3136	3.496	3.5	0.545	**Prazeres, 2008**
pACL29	3564	3.552	3.1	0.491	**Prazeres, 2008**
ColE1	4290	3.632	2.9	0.461	**Prazeres, 2008**
pDR1996	6732	3.828	2.3	0.362	**Prazeres, 2008**
pPIC9K<TRL5>	7326	3.865	1.7	0.217	**Prazeres, 2008**
pCC1FOS™45	29700	4.473	0.6	-0.222	**Prazeres, 2008**
CTD-2342K16	74448	4.872	0.5	-0.310	**Prazeres, 2008**
CTD-2609C22	121110	5.083	0.3	-0.481	**Prazeres, 2008**
CTD-2657L24	189486	5.278	0.2	-0.638	**Prazeres, 2008**
EGFP1	30	1.477	104.0	2.017	**Pack *et al.*, 2006**
EGFP1	27	1.431	87.0	1.940	**Arrio-Dupont *et al.*, 2000**
EGFP2	60	1.778	71.8	1.856	**Pack et al., 2006**
EGFP3	90	1.954	61.3	1.787	**Pack et al., 2006**
EGFP4	120	2.079	48.7	1.688	**Pack et al., 2006**
EGFP5	150	2.176	45.2	1.655	**Pack et al., 2006**
EGFP1	27	1.430	97.3	1.988	**Vámosi *et al.*, 2016**
EGFP2	54	1.735	98.8	1.995	**Vámosi *et al.*, 2016**

14603075, 2023, 7, Downloaded from https://www.embopress.org/doi/10.15252/embj.2021108533 by Wageningen University and Research Bibliotheek, Wiley Online Library on [11/08/2023]. See the Terms and Conditions (https://onlinelibrary.wiley.com/terms-and-conditions) on Wiley Online Library for rules of use; OA articles are governed by the applicable Creative Commons License

EGFP3	82	1.912	60.2	1.780	**Vámosi *et al.*, 2016**
EGFP4	109	2.038	54.8	1.739	**Vámosi *et al.*, 2016**
ELONGATED, FIBROUS STRUCTURE OR ROD-LIKE MOLECULES IN THE NUCLEUS OF HELA CELLS Fitting results of LOG(MW) *vs.* LOG($D_{solvent}$): **Y=A+B·X:** R=-0.926; P=3.42E-4; A=2.72±0.214(SE); B=-0.748±0.115(SE)					
EGFP1 - nucleus HeLa	30	1.477	32.3	1.510	**Pack *et al.*, 2006**
EGFP2 - nucleus HeLa	60	1.778	21.2	1.327	**Pack *et al.*, 2006**
EGFP3 - nucleus HeLa	90	1.954	16.5	1.218	**Pack *et al.*, 2006**
EGFP4 - nucleus HeLa	120	2.079	12.3	1.088	**Pack *et al.*, 2006**
EGFP5 - nucleus HeLa	150	2.176	11.1	1.046	**Pack *et al.*, 2006**
EGFP1 - nucleus HEK293, HeLa, TP366, T98G	27	1.431	50.6	1.704	**Dross *et al.*, 2009**
EGFP2 - nucleus HEK293, HeLa, TP366, T98G	54	1.732	31.0	1.491	**Dross *et al.*, 2009**
EGFP3 - nucleus HEK293, HeLa, TP366, T98G	81	1.908	23.8	1.377	**Dross *et al.*, 2009**
EGFP4 - nucleus HEK293, HeLa, TP366, T98G	108	2.033	20.2	1.305	**Dross *et al.*, 2009**
ELONGATED, FIBROUS STRUCTURE OR ROD-LIKE MOLECULES IN THE CYTOSOL OF HELA CELLS Fitting results of LOG(MW) *vs.* LOG($D_{solvent}$): **Y=A+B·X:** R=-0.984; P=0.00236; A=2.53±0.131(SE); B=-0.665±0.0688(SE)					
EGFP1 - cytosol HeLa	30	1.477	33.3	1.523	**Pack *et al.*, 2006**
EGFP2 - cytosol HeLa	60	1.778	23.4	1.369	**Pack *et al.*, 2006**
EGFP3 - cytosol HeLa	90	1.954	18.7	1.271	**Pack *et al.*, 2006**
EGFP4 - cytosol HeLa	120	2.079	12.8	1.108	**Pack *et al.*, 2006**
EGFP5 - cytosol HeLa	150	2.176	11.8	1.073	**Pack *et al.*, 2006**
ACGFP1 CONCATEMERS IN THE MITOCHONDRIA OF HELA CELLS Fitting results of LOG(MW) *vs.* LOG($D_{solvent}$): **Y=A+B·X:** R=-0.997; P=0.00268; A=2.81±0.0923(SE); B=-0.976±0.0506(SE)					
AcGFP1	29	1.465	23.9	1.378	**Current study**
$AcGFP1^2$	58	1.760	11.8	1.072	**Current study**
$AcGFP1^3$	88	1.943	8.6	0.934	**Current study**
$AcGFP1^4$	115	2.062	6.0	0.780	**Current study**

Remarks: Data in **red** of **Pack *et al.*, 2006** were corrected as proposed by **Dross *et al.*, 2009** using a diffusion constant for Rhodamine 6G of 430 $\mu m^2/s$ (**Jameson *et al.*, 2009**). Data for the Tobacco mosaic virus was not included since this virus is geometrically extreme (*i.e.* it resembles a cylinder with a length/diameter ratio of 16.7; **Saxton, 2014**).

14603075, 2023, 7, Downloaded from https://www.embopress.org/doi/10.15252/embj.2021108533 by Wageningen University and Research Bibliotheek, Wiley Online Library on [11/08/2023]. See the Terms and Conditions (https://onlinelibrary.wiley.com/terms-and-conditions) on Wiley Online Library for rules of use; OA articles are governed by the applicable Creative Commons License

Appendix Supplementary Table S3: Interpretation of the data sets in Appendix Supplementary Table S2

Dataset	Environment	Techniques	Interpretation	References
Globular or spherical conformation in aqueous solution				
Globular	Aqueous solution	Various	Globular structure	**Young *et al.*, 1980** **Tyn & Gusek, 1990** **Durchslag & Zipper, 1997** **Gribbon *et al.*, 1998** **Arrio-Dupont *et al.*, 2000** **Papadopoulos *et al.*, 2000** **He & Niemeyer, 2003** **Saxton, 2014**
Virus	Aqueous solution	Various	Globular structure	**Tyn & Gusek, 1990** **Durchslag & Zipper, 1997** **Saxton, 2014**
Elongated, fibrous structure or rod-like conformation in aqueous solution				
Fibrous	Aqueous solution	Various	Fibrous, elongated structure	**Tyn & Gusek, 1990** **Saxton, 2014**
Plasmids	Aqueous solution	Various	Supercoiled, elongated structure	**Prazeres, 2008**
(E)GFP concatemers	Aqueous solution	FCS	Rod-like molecules	**Pack *et al.*, 2006** **Vámosi *et al.*, 2016**
Elongated, fibrous structure or rod-like molecules in the cell				
EGFP concatemers	Nucleus of HeLa cells	FCS	Rod-like molecules	**Pack *et al.*, 2006**
EGFP concatemers	Cytoplasm of HeLa cells	FCS	Rod-like molecules	**Pack *et al.*, 2006**
EGFP concatemers	Nucleus of HeLa cells	FCS	Rod-like molecules	**Dross *et al.*, 2009**

14602075, 2023, 7, Downloaded from https://www.embopress.org/doi/10.15252/embj.2021108533 by Wageningen University and Research Bibliotheek, Wiley Online Library on [11/08/2023]. See the Terms and Conditions (https://onlinelibrary.wiley.com/terms-and-conditions) on Wiley Online Library for rules of use; OA articles are governed by the applicable Creative Commons License

5. Appendix Supplementary References

1. **Ajaz S**, Czajka A, Malik A (2015) Accurate measurement of circulating mitochondrial DNA content from human blood samples using real-time quantitative PCR. *Meth Mol Biol* 1264: 117-131
2. **Akabayov B**, Akabayov SR, Lee SJ, Wagner G, Richardson CC (2013) Impact of macromolecular crowding on DNA replication. *Nat Commun* 4: 1615
3. **Appelhans T**, Richter CP, Wilkens V, Hess ST, Piehler J, Busch KB (2011) Nanoscale organisation of mitochondrial microcompartments revealed by combining tracking and localization microscopy. *Nano Lett* 12: 610-616
4. **Arrio-Dupont M**, Cribier S, Foucault G, Devaux PF, d'Albis A, (1996) Diffusion of fluorescently labeled macromolecules in cultured muscle cells. *Biophys J* 70: 2327-2332
5. **Arrio-Dupont M**, Foucault G, Vacher M, Devaux PF, Cribier S (2000) Translational diffusion of globular proteins in the cytoplasm of cultured muscle cells. *Biophys J* 78: 901-907
6. **Bell P**, Vandenberghe LH, Wu D, Johnston J, Limberis M, Wilson JM (2007) A comparative analysis of novel fluorescent proteins as reporters for gene transfer studies. *J Histochem Cytochem* 55: 931-939
7. **Blässle A**, Soh G, Braun T, Mörsdorf D, Preiss H, Jordan BM, Müller P (2018) Quantitative diffusion measurements using the open-source software PyFRAP. *Nat Commun* 9: 1582
8. **Burbulla LF**, Fitzgerald JC, Stegen K, Westermeier J, Thost AK, Kato H, Mokranjac D, Sauerwald J, Martins LM, Woitalla D, *et al.* (2014) Mitochondrial proteolytic stress induced by loss of mortalin function is rescued by Parkin and PINK1. *Cell Death Dis* 5: e1180
9. **Bulina ME**, Chudakov DM, Britanova OV, Yanushevich YG, Staroverov DB, Chepurnykh TV, Merzlyak EM, Shkrob MA, Lukyanov S, Lukyanov KA (2006) A genetically encoded photosensitizer. *Nat Biotechnol* 24: 95-99
10. **Bustin SA**, Benes V, Garson JA, Hellemans J, Huggett J, Kubista M, Mueller R, Nolan T, Pfaffl MW, Shipley GL, Vandesompele J, Wittwer CT (2009) The MIQE guidelines: minimum information for publication of quantitative real-time PCR experiments. *Clin Chem* 55: 611-622.
11. **Dashevskaya S**, Kopito RB, Friedman R, Elbaum M, Epel BL (2008) Diffusion of anionic and neutral GFP derivatives through plasmodesmata in epidermal cells of *Nicotiana benthamiana*. *Protoplasma* 234: 13-23.
12. **Dieteren CEJ**, Willems PHGM, Vogel RO, Swarts HG, Fransen J, Roepman R, Crienen G, Smeitink JAM, Nijtmans LGJ, Koopman WJH (2008) Subunits of Mitochondrial Complex I Exist as part of matrix- and membrane-associated subcomplexes in living cells. *J Biol Chem* 283: 34753-34761
13. **Dieteren CEJ**, Gielen SCAM, Nijtmans LGJ, Smeitink JAM, Swarts HG, Brock R, Willems PHGM, Koopman WJH (2011) Solute diffusion is hindered in the mitochondrial matrix. *Proc Natl Acad Sci USA* 108: 8657-8662
14. **Divakaruni AS**, Jastroch M (2022) A practical guide for the analysis, standardization and interpretation of oxygen consumption measurements. *Nat Metab* 4:978-994
15. **Dross N**, Spriet C, Zwerger M, Müller G, Waldeck W, Langowski J (2009) Mapping eGFP oligomer mobility in living cell nuclei. *PLoS ONE* 4: e5041
16. **Durchslag H**, Zipper P (1997) Prediction of hydrodynamic parameters of biopolymers from small-angle scattering data. *J Appl Cryst* 30: 1112-1124
17. **Einstein A** (1905) Über die von der molekularkinetischen Theorie der Wärme geforderte Bewegung von in ruhenden Flüssigkeiten suspendierten Teilchen. *Annalen der Physik* 322: 549-560
18. **Elachouri G,** Vidoni S, Zanna C, Pattyn A, Boukhaddaoui H, Gaget K, Yu-Wai-Man P, Gasparre G, Sarzi E, Delettre C, *et al.* (2011) OPA1 links human mitochondrial genome maintenance to mtDNA replication and distribution. *Genome Res* 21: 12-20
19. **Erban R** (2014) From molecular dynamics to Brownian dynamics. *Proc R Soc A* 470: 20140036
20. **Goodwin JS**, Kenworthy AK (2005) Photobleaching approaches to investigate diffusional mobility and trafficking of Ras in living cells. *Methods* 37: 154-164
21. **Gribbon P**, Hardingham TE (1998) Macromolecular diffusion of biological polymers measured by confocal fluorescence recovery after photobleaching. *Biophys J* 75: 1032-1039

14602075, 2023, 7, Downloaded from https://www.embopress.org/doi/10.15252/embj.2021108533 by Wageningen University and Research Bibliotheek, Wiley Online Library on [11/08/2023]. See the Terms and Conditions (https://onlinelibrary.wiley.com/terms-and-conditions) on Wiley Online Library for rules of use; OA articles are governed by the applicable Creative Commons License

22. **He L**, Niemeyer B (2003) A novel correlation for protein diffusion coefficients based on molecular weight and radius of gyration. *Biotechnol Prog* 19: 544-548
23. **Houtkooper RH,** Mouchiroud L, Ryu D, Moullan N, Katsyuba E, Knott G, Williams RW, Auwerx J (2013) Mitonuclear protein imbalance as a conserved longevity mechanism. *Nature* 497: 451-459
24. **Huber GA, McCammon JA** (2019) Brownian dynamics simulations of biological molecules. *Trends Chem* 1: 727-738
25. **Hu C**, Shu L, Huang X, Yu J, Li L, Gong L, Yang M, Wu Z, Gao Z, Zhao Y, Chen L, Song Z (2020) OPA1 and MICOS regulate mitochondrial crista dynamics and formation. *Cell Death Dis* 11: 940
26. **Jameson DM**, Ross JA, Albanesi JP (2009) Fluorescence fluctuation microscopy: ushering a new age of enlightenment for cellular dynamics. *Biophys Rev* 1: 105-118
27. **Koopman WJH**, Visch HJ, Smeitink JAM, Willems PHGM (2006) Simultaneous, quantitative measurement and automated analysis of mitochondrial morphology, mass, potential and motility in living human skin fibroblasts, *Cytometry A* 69A: 1-12
28. **Koopman WJH**, Distelmaier F, Hink MA, Verkaart S, Wijers M, Fransen J, Smeitink JAM, Willems PHGM (2008a) Inherited complex I deficiency is associated with faster protein diffusion in the matrix of moving mitochondria. *Am J Physiol Cell Physiol* 294: C1124-C1132
29. **Koopman WJH,** Distelmaier F, Esseling JJ, Smeitink JAM, Willems PHGM (2008b) Computer-assisted live cell analysis of mitochondrial membrane potential, morphology and calcium handling. *Methods* 46: 304-311
30. **Lavalette D**, Hink MA, Tourbez M, Tétreau C, Visser AJ (2006) Proteins as microviscosimeters: Brownian motion revisited. *Eur Biophys J* 35: 517-522
31. **Levenberg K** (1944) A method for the solution of certain non-linear problems in least squares. *Quarterly Appl Math* 2: 164-168.
32. **Lorén N**, Hagman J, Jonasson JK, Deschout H, Bernin D, Cella-Zanacchi F, Diaspro A, McNally JG, Ameloot M, Smisdom N, (2015) Fluorescence recovery after photobleaching in material and life sciences: putting theory into practice. *Q Rev Biophys* 48: 323-387
33. **Malik AN**, Shahni R, Rodriguez-de-Ledesma A, Laftah A, Cunningham P (2011) Mitochondrial DNA as a non-invasive biomarker: accurate quantification using real time quantitative PCR without co-amplification of pseudogenes and dilution bias. *Bioch Biophys Res Comm* 412 :1-7
34. **Marquardt DW** (1963) An algorithm for the least-squares estimation of nonlinear parameters. *SIAM J Appl Math.* 11: 431-441.
35. **Minier F**, Sigel E (2004) Techniques: Use of concatenated subunits for the study of ligand-gated ion channels. *Trends Pharmacol Sci* 25: 499-503
36. **Monkos K** (2004) On the hydrodynamics and temperature dependence of the solution conformation of human serum albumin from viscometry approach. *Biochim Biophys Acta* 1700: 27-34
37. **Minton AP** (1981) Excluded volume as a determinant of macromolecular structure and reactivity. *Biopolymers* 20: 2093-2120
38. **Moullan N,** Mouchiroud L, Wang X, Ryu D, Williams EG, Mottis A, Jovaisaite V, Frochaux MV, Quiros PM, Deplancke B, *et al.* (2015) Tetracyclines disturb mitochondrial function across eukaryotic models: a call for caution in biomedical research. *Cell Rep* 10: 1681-1691
39. **Nooteboom M**, Forkink M, Willems PHGM, Koopman WJH (2012) Live-cell quantification of mitochondrial functional parameters. Chapter 6 in: *Neuromethods* 70: Visualization techniques, from immunohistochemistry to Magnetic Resonance Imaging (Badoer, E., ed.)
40. **Nicholls TJ,** Gustafsson CM (2018) Separating and segregating the human mitochondrial genome. *Trends Biochem Sci* 43: 869-881
41. **Ölveczky BP,** Verkman AS (1998) Monte Carlo analysis of obstructed diffusion in three dimensions: application to molecular diffusion in organelles. *Biophys J* 74: 2722-2730
42. **Pack C**, Saito K, Tamura M, Kinjo M (2006) Microenvironment and effect of energy depletion in the nucleus analyzed by mobility of multiple oligomeric EGFPs. *Biophys J* 91: 3921-3936

14602075, 2023, 7, Downloaded from https://www.embopress.org/doi/10.15252/embj.2021108533 by Wageningen University and Research Bibliotheek, Wiley Online Library on [11/08/2023]. See the Terms and Conditions (https://onlinelibrary.wiley.com/terms-and-conditions) on Wiley Online Library for rules of use; OA articles are governed by the applicable Creative Commons License

43. **Palmer AE**, Jin C, Reed JC, Tsien RY (2004) Bcl-2-mediated alterations in endoplasmic reticulum Ca^{2+} analyzed with an improved genetically encoded fluorescent sensor. *Proc Natl Acad Sci USA* 101: 17404-17409
44. **Papadopoulos S**, Jürgens KD, Gros G (2000) Protein diffusion in living skeletal muscle fibers: Dependence on protein size, fiber type, and contraction. *Biophys J* 79: 2084-2094
45. **Partikian A**, Olveczky B, Swaminathan R, Li Y, Verkman AS (1998) Rapid diffusion of green fluorescent protein in the mitochondrial matrix. *J Cell Biol* 140: 821-829
46. **Perrin, F.** (1936) Mouvement Brownien d'un ellipsoide (II). Rotation libre et dépolarisation des fluorescences. Translation et diffusion de molécules ellipsoidales. *J Phys Radium* 7: 1-11
47. **Prazeres DMF** (2008) Prediction of diffusion coefficients of plasmids. *Biotechnol Bioeng* 99:1040-1044
48. **Richter U,** Ng KY, Suomi F, Marttinen P, Turunen T, Jackson C, Suomalainen A, Vihinen H, Jokitalo E, Nyman TA, *et al.* (2019) Mitochondrial stress response triggered by defects in protein synthesis quality control. *Life Sci Alliance* 2: e201800219
49. **Rizzutto F,** Nakase H, Darras B, Francke U, Fabrizi GM, Mengel T, Walsh F, Kadenbach B, DiMauro S, Schon EA (1989) A gene specifying subunit VIII of human cytochrome-*c* oxidase is localized to chromosome 11 and is expressed in both muscle and non-muscle tissues. *J Biol Chem* 264: 10595–10600
50. **Saxton MJ** (2014) Wanted: Scalable tracers for diffusion measurements. *Phys Chem B* 118: 12805-12817
51. **Segawa M**, Wolf DM, Hultgren NW, Williams DS, van der Bliek AM, Schackelford DB, Liesa M, Shirihai OS. (2020) Quantification of cristae architecture reveals time-dependent characteristics of individual mitochondria. *Life Sci Alliance* 3: e201900620
52. **Shpilka T,** Haynes CM (2018) The mitochondrial UPR: mechanisms, physiological functions and implications in ageing. *Nat Rev Mol Cell Biol* 19: 109-120
53. **Sutherland W** (1905) A dynamical theory of diffusion for non-electrolytes and the molecular mass of albumin. *Philosophical Magazine* 9: 781–785
54. **Terry BR**, Matthews EK, Haseloff J. (1995) Molecular characterisation of recombinant green fluorescent protein by fluorescence correlation microscopy. *Biochem Biophys Res Commun* 217: 21-27
55. **Thubron EB**, Rosa HS, Hodges A, Sivaprasad S, Francis PT, Pienaar IS, Malik AN (2019) Regional mitochondrial DNA and cell-type changes in post-mortem brains of non-diabetic Alzheimer's disease are not present in diabetic Alzheimer's disease. *Sci Rep* 9: 11386
56. **Tyn MT**, Gusek TD (1990) Prediction of diffusion coefficients of proteins. *Biotechnol Bioeng* 35: 327-338
57. **Van Helvoort JMLM,** Kool J, Woldringh CL (1996) Chloramphenicol causes fusion of separated nucleoids in *Escherichia coli* K-12 cells and filaments. *J Bacteriol* 178: 4289-4293
58. **Vámosi G**, Mücke N, Müller G, Krieger JW, Curth U, Langowski J, Tóth K (2014) EGFP oligomers as natural fluorescence and hydrodynamic standards. *Sci Rep* 6: 33022
59. **Von Smoluchowski M** (1906) Zur kinetischen Theorie der Brownschen Molekularbewegung und der Suspensionen. *Annalen der Physik* 326: 756–780
60. **Weissert V**, Rieger B, Morris S, Arroum T, Psathaki OE, Zobel T, Perkins G, Busch KB (2021) Inhibition of the mitochondrial ATPase function by IF1 changes the spatiotemporal organisation of ATP synthase. *Biochim Biophys Acta Bioenerg* 1862: 148322
61. **Wilkens V**, Kohl W, Busch K (2012) Restricted diffusion of OXPHOS complexes in dynamic mitochondrial delays their exchange between cristae and engenders a transitory mosaic distribution. *J Cell Sci* 126: 103-116
62. **Willems PHGM**, Swarts HG, Hink MA, Koopman WJH (2009) Chapter 16: The use of fluorescence correlation spectroscopy to probe mitochondrial mobility and intramatrix protein diffusion. *Methods Enzymol* 456: 287-302

14602075, 2023, 7, Downloaded from https://www.embopress.org/doi/10.15252/embj.2021108533 by Wageningen University and Research Bibliotheek, Wiley Online Library on [11/08/2023]. See the Terms and Conditions (https://onlinelibrary.wiley.com/terms-and-conditions) on Wiley Online Library for rules of use; OA articles are governed by the applicable Creative Commons License

63. **Wolf DM**, Segawa M, Kondadi AK, Anand R, Bailey ST, Reichert AS, van der Bliek AM, Schackelford DB, Liesa M, Shirihai O (2019) Individual cristae within the same mitochondrion display different membrane potentials and are functionally independent. *EMBO J* 38: e101056
64. **Xu M,** Bi X, He X, Yu X, Zhao M, Zhang W (2016) Inhibition of the mitochondrial unfolded protein response by acetylcholine alleviated hypoxia/reoxygenation-induced apoptosis of endothelial cells. *Cell Cycle* 15: 1331-1343
65. **Yang F**, Moss LG, Philips Jr, GN (1996) The molecular structure of green fluorescent protein. *Nature Biotechnol* 14: 1246-1251
66. **Young ME**, Carroad PA, Bell RL (1980) Estimation of diffusion coefficients of proteins. *Biotechnol Bioeng* 22: 947-955
67. **Zhao Q,** Wang J, Levichkin IV, Stasinopoulos S, Ryan MT, Hoogenraad NJ (2002) A mitochondrial specific stress response in mammalian cells. *EMBO J* 21: 4411-4419

14602075, 2023, 7, Downloaded from https://www.embopress.org/doi/10.15252/embj.2021108533 by Wageningen University and Research Bibliotheek, Wiley Online Library on [11/08/2023]. See the Terms and Conditions (https://onlinelibrary.wiley.com/terms-and-conditions) on Wiley Online Library for rules of use; OA articles are governed by the applicable Creative Commons License